UNIVERSITAT POLITÈCNICA DE CATALUNYA
PROGRAMA DE DOCTORADO DE INGENIERÌA CIVIL

Doctoral Thesis

HIERARCHICAL SEMIACTIVE CONTROL OF BASE-ISOLATED STRUCTURES

Arash Bahar

Barcelona, April 2009

UNIVERSITAT POLITÈCNICA DE CATALUNYA
PROGRAMA DE DOCTORADO DE INGENIERÌA CIVIL

Doctoral Thesis in Civil Engineering

HIERARCHICAL SEMIACTIVE CONTROL OF BASE-ISOLATED STRUCTURES

BY
Arash Bahar

Advisors: José Rodellar Benedé
Alex Barbat

Barcelona, April 2009

To my wife Afsaneh
and my son Kiarash
for their great patience

Acknowledgements

I would like to thank my advisors Prof. Dr. José Rodellar Benedé and Prof. Dr. Alex Barbat, for their help, guidance and a never-ending fount of moral support. This thesis is the result of their inspiration, creativity and experience. Their advises and suggestions were critical and helpful completing this thesis.

I also want to extend my thanks to Dr. Francesc Pozo and Dr. Leonardo Acho, for their readiness to lend a hand. They deserve special recognition for agreeing to serve on the committee and critique this study. I have learned so much from them, from figuring out what research is, to learning how to present my work.

Finally, I would like to give thanks and all of my love to my wife, Afsaneh, for her encouragement, interest in my work, and all her aid, when I need moral support.

Contents

List of Tables

List of Figures

Motivation and objectives

Motivation

In structural engineering, one of the constant challenges is to find new better means of protecting structures from the damaging effects of destructive environmental forces. This can be achieved by applying traditional seismic design principles, which assume that earthquakes act upon the structure across its fixed base, to assure partial dissipation of the induced energy. Plastic deformation of certain members can occur and, as a result, the structure is damaged to a certain degree. This disadvantage can be avoided by using passive, active, hybrid, and semiactive control strategies.

Passive control refers to systems that utilize the response of structures to develop the control forces without requiring an external power source for their operation. Active control, on the other hand, refers to systems that require a large power source to operate the actuators that supply the control forces. Semiactive control combines the features of active and passive systems. These systems require a small power source to operate and utilize the response of the structure to develop the control forces that are regulated by algorithms using the measured excitation and/or response. Hybrid control implies the combined use of active and passive control systems or semiactive and passive ones.

Passive supplemental damping strategies are well understood and are widely accepted by the engineering community as

a means for mitigating the effects of dynamic loading on structures. Seismic isolation system is one of the most well accepted passive control methods which has been shown to not only reduce the response of the primary structure, but also reduce damage to equipment and other non-structural secondary elements. A drawback of most isolation systems becomes apparent when one considers the response of isolated structures subjected to earthquakes characterized by near-field motions. Such motions are likely to produce large isolation system deformations, which in turn, may lead to buckling or rupture of isolators. Moreover, these passive-device methods are unable to adapt to structural changes and to varying loading conditions.

In order to overcome these drawbacks one way is to utilize supplemental dampers together with the isolation system (a hybrid system). However the beneficial effects of the isolation system may be significantly reduced for both moderate and strong earthquakes due to the transfer of energy into higher modes which can result in increased interstory drift and floor acceleration responses.

Preliminary studies indicate that appropriately implemented semiactive systems perform significantly better than passive devices and have the potential to achieve the majority of the performance of fully active systems, thus allowing for the possibility of effective response reduction during a wide array of dynamic loading conditions. Therefore, one approach for improving the performance of an isolation system is to incorporate a semiactive device within the isolation system whose properties can be adjusted in real-time during an earthquake. Specifically the magnetorheological (MR) dampers appear to have significant potential to advance the acceptance of structural control as a viable means for dynamic hazard mitigation. However, because of the inherent nonlinearity of MR dampers, the first step in the design of a semi-active control strategy is the development of an accurate model of the MR device. The system-identification issue plays a key role in control problems.

As in a passive control system, the control forces in semi-active systems are developed as a result of the motion of the structure itself. They can only be modified through appropriate adjustment of mechanical properties of semi-active devices. Furthermore, the control forces act to oppose the motion of the structural system and therefore promote the global stability of the structure.

Objectives of the thesis

The nature of this research is multidisciplinary because it deals with two concepts, identification of a mechanical device (MR damper) as well as a structural control problem in a civil engineering perspective. In other words, this study will focus on the development of a new parameter identification method for MR dampers which will lead to a new inverse model for these highly non-linear semi-active devices. The resulted inverse model will be used in a control strategy. The proposed control strategy will be developed to manipulate the command voltage of a group of MR dampers installed at the base level of a base-isolated building in order to generate a control force as close as possible to the desired one. Finally, the resulted control strategy will be applied to improve the dynamic behavior of a benchmark base-isolated structure subjected to near-fault pulse-type ground motions.

Therefore the main objectives of this study can be summarized as follows:

- Develop a new extended parameter identification method for MR dampers based on the normalized Bouc-Wen model.
- Define a new inverse model for MR dampers based on the identification results.
- Design a hierarchical control strategy for a hybrid system consisting of a set of base-isolators and MR dampers for a building structure.
- Assess the efficiency of the control strategy in a numerical three-dimensional model of a base-isolated buildings used

by the structural control community as a benchmark for assessment of seismic control systems.

Layout of the thesis

- ▷ **Chapter 1** presents some general information about MR dampers. The mechanical properties of magnetorheological fluid and the way it changes is discussed. Different types of MR dampers and their mathematical models are presented, including a normalized version of the Bouc-Wen model.

- ▷ In **Chapter 2** a modified Bouc-Wen based normalized model is developed to study the behavior of a wider range of MR dampers, specially the devices which are more effective in the vibration control of real structures. This model then leads to an extended parameter identification method for MR dampers. The result of this modification is its ability to identify a larger class of MR dampers with more accuracy. In order to validate the method, a black-box model of an MR damper which comes with the benchmark program is used as a virtual device. The output force of this virtual damper is used as laboratory test data. The versatility of the proposed parameter identification method is tested using the MR damper as a semi-active device under time-varying voltage and earthquake excitation.

- ▷ **Chapter 3** deals with a new inverse model for MR dampers. This model is derived from the extended normalized Bouc-Wen model, which resulted in Chapter 2, based on two practical simplifications and considering additional operational constraints. The inverse model will serve to determine the command voltage of the MR damper to approach a desired control force.

- ▷ In **Chapter 4** a hierarchical semi-active control strategy is presented. This control strategy consists of a supervisor block which will calculate the desired level of control

force based on the sign of the base velocity. The number of dampers which can apply an effective force in the same direction of the desired control force is found and the corresponding command voltage will be calculated using the inverse model.

▷ **Chapter 5** presents the numerical application of the control strategy by considering a three-dimensional smart base-isolated benchmark building. Performance indices as long as time history plots and resulted damping force are presented.

▷ In **Chapter 6** some concluding remarks and future lines for investigations are presented.

Chapter 1

MR dampers

1.1 Introduction

A magnetorheological (MR) damper consists of a solution that, in the presence of a magnetic field, can reversibly change from a free-flowing, linear viscous fluid to a semi-solid with controllable yield strength [10]. This feature provides simple and rapid response interfaces between electronic controls and mechanical systems. Normally, MR fluids are free flowing liquids having a consistency similar to that of motor oil [43]. However, in the presence of an applied magnetic field, the iron particles (carbonyl iron) acquire a dipole moment aligned with the external field which causes particles to form linear chains parallel to the field (Figure 1.1).

This phenomenon can solidify the suspended iron particles and restrict the fluid movement. Consequently, yield strength develops within the fluid. This change is manifested by change of the damper force in which MR fluids are used. The degree of change is related to the magnitude of the applied magnetic field, and can occur only in a few milliseconds. A typical MR fluid consists of 20-40 percent by volume of relatively pure, 3-10 micron diameter iron particles, suspended in a carrier liquid such as mineral oil, synthetic oil, water or glycol [118]. In contrast to their electrical counter-part, the electrorheological (ER), MR fluids are not highly sensitive to moisture or other contaminants

that might be encountered during manufacture and usage [52]. Further, because the magnetic polarization mechanism is unaffected by temperature (The operation range has reported in [52] from -40 to 150 ℃ with a slight variation of the yield stress), the performance of MR-based devices is relatively insensitive to temperature over a broad temperature range (including the range for automotive use) [42].

MR fluid can be used in three different ways, all of which can be applied to MR damper design depending on the damper's intended use. These modes of operation are referred to as squeeze mode, valve mode (pressure driven flow mode), and shear mode. A device that uses squeeze mode has a thin film (on the order of 0.020 in.) of MR fluid that is sandwiched between paramagnetic pole surfaces as shown in Figure 1.2. An MR fluid device is said to operate in shear mode when a thin layer (0.005 to 0.015 in.) of MR fluid is sandwiched between two paramagnetic moving surfaces. Shear mode (see Figure 1.3) is useful primarily for dampers that are not required to produce large forces and for clutches and brakes. The last mode of MR damper operation, valve mode (see Figure 1.4), is the most widely used of the three modes [88]. An MR device is said to operate in valve mode when the MR fluid is used to impede the flow of MR fluid from one reservoir to another. Most devices that use controllable fluids can be classified as having either fixed poles

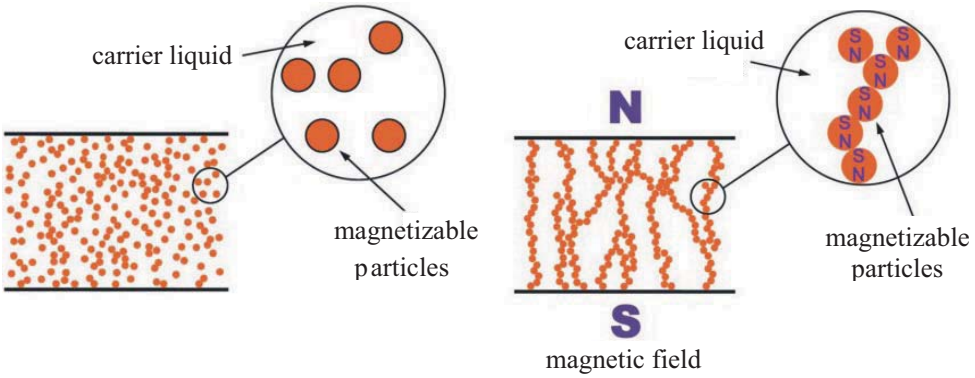

Figure 1.1: MR Fluid Behavior [56].

(working frequently in pressure driven flow mode) or relatively movable poles (working in direct-shear mode) [88].

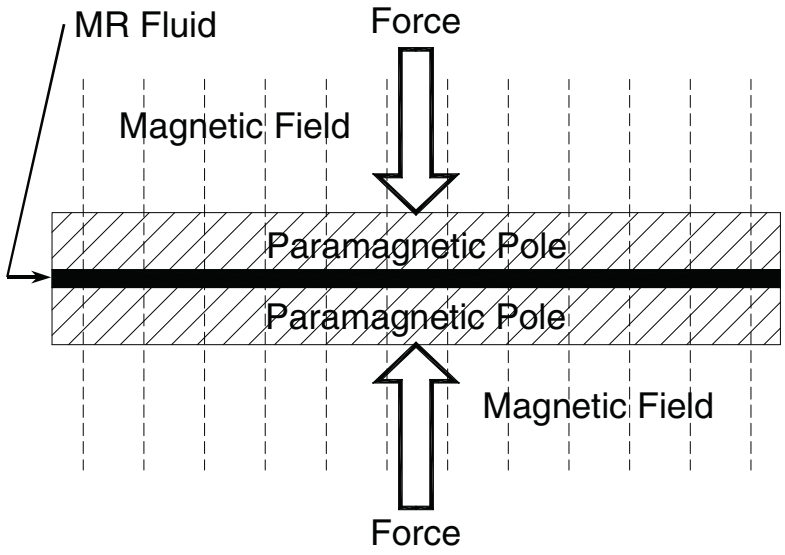

Figure 1.2: MR fluid used in squeeze mode.

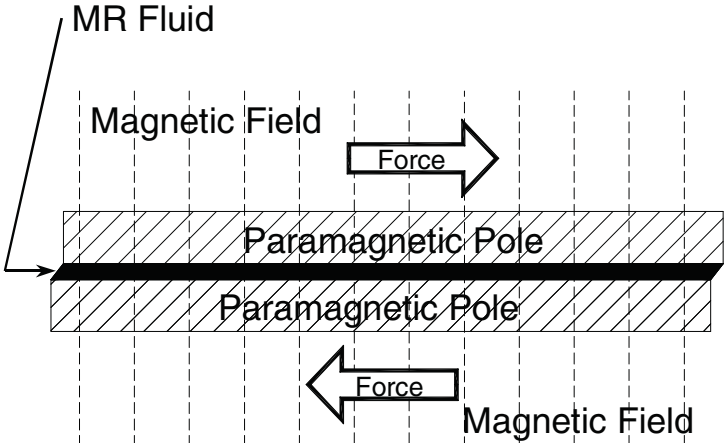

Figure 1.3: MR fluid used in shear mode.

Commercialization of MR technology begun in 1995 by use

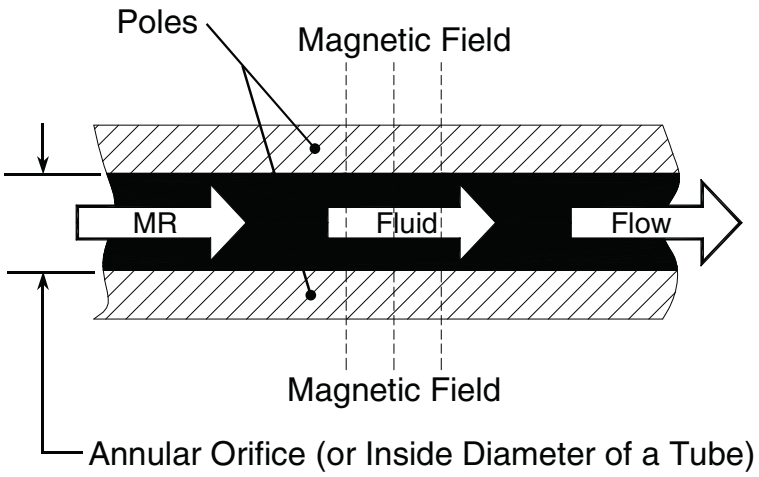

Figure 1.4: MR fluid used in valve mode.

of rotary brakes in aerobic exercise equipment. From this moment, application of magnetorheological material technology in real-world systems has grown steadily [56]. MR fluid operating in valve mode, with fixed magnetic poles, is appropriate for hydraulic controls, servo valves, shock absorbers, and dampers (include the models which called tube/linear MR dampers, see Figure 1.5). The direct-shear mode with a moving pole, in turn, would be suitable for clutches and brakes, chucking/locking devices, dampers (include the models which called shear mode or rotary MR dampers, see Figure 1.6), breakaway devices and structural composites [52]. During the past few years a number of commercially available products (or near commercialization) have been developed, e.g. [44][58]:

- MR dampers for real-time active vibrational control systems in heavy duty trucks,
- linear and rotary brakes for low-cost, accurate, positional and velocity control of pneumatic actuator systems,
- rotary brakes to provide tactile force-feedback in steer-by wire systems,
- linear dampers for real-time gait control in advanced prosthetic devices,

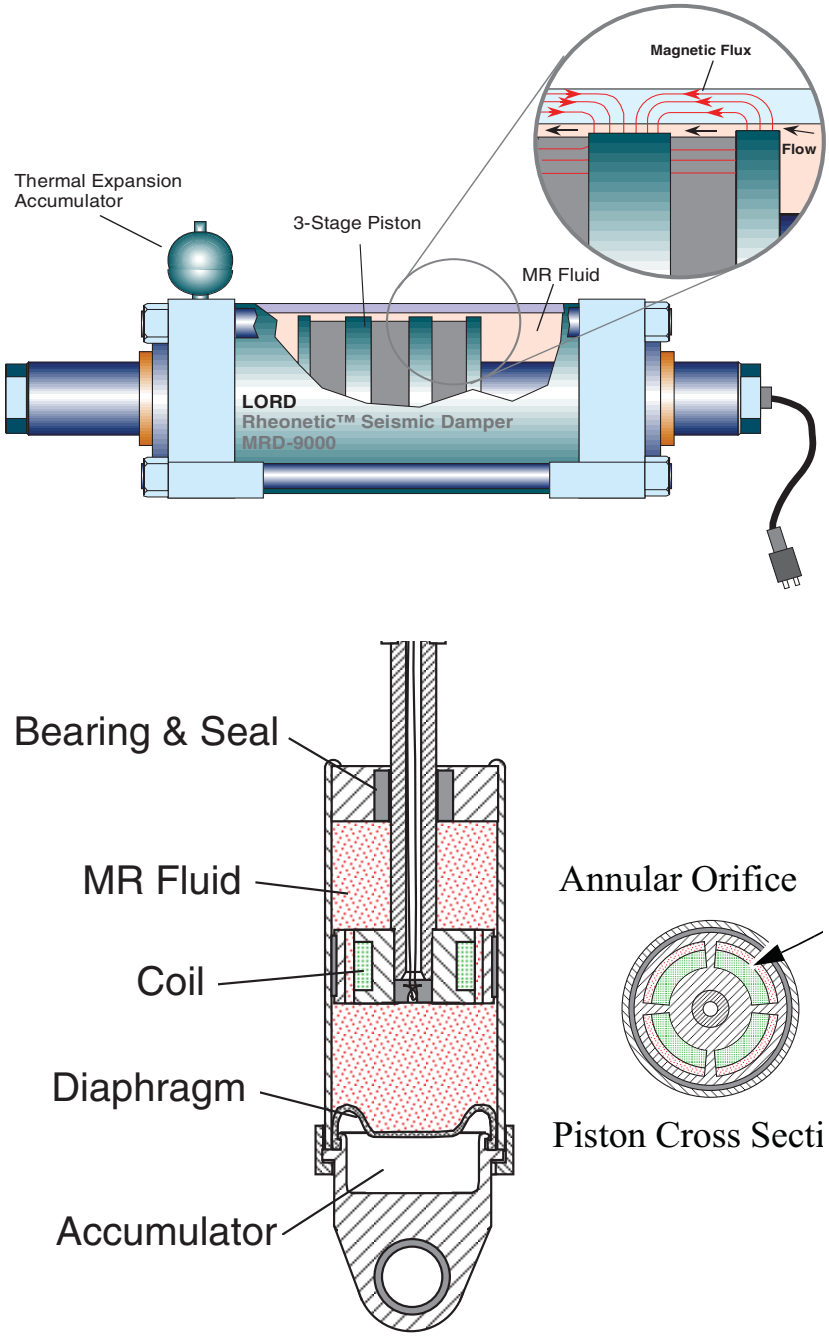

Figure 1.5: Two models of Linear MR damper [118].

- adjustable real-time controlled shock absorbers for automobiles,
- MR sponge dampers for washing machines (see section 1.2.1),
- magnetorheological fluid polishing tools,
- very large MR fluid dampers for seismic damage mitigation in civil engineering structures,
- large MR fluid dampers to control wind-induced vibrations in cable-stayed bridges.

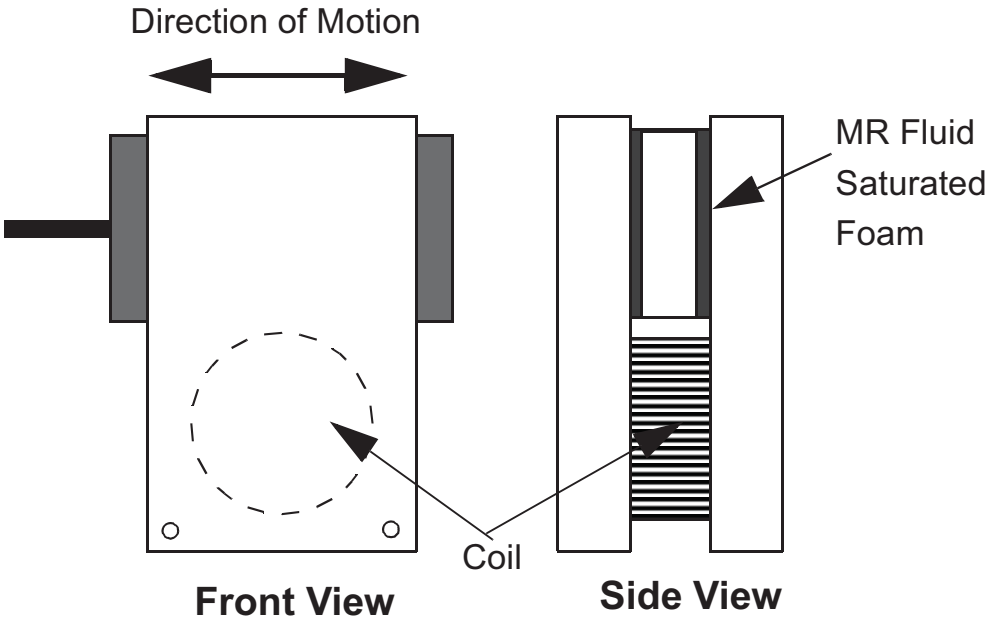

Figure 1.6: Schematic diagram of a shear mode MR damper [50].

1.2 MR dampers

MR dampers are semi-active devices that contain magnetorheological fluids. After application of a magnetic field the fluid changes from liquid to semi-solid state in few milliseconds, so

the result is an infinitely variable, controllable damper capable of generating large damping forces. MR dampers offer an attractive solution to energy absorption in mechanical systems and structures and can be considered as fail-safe devices. MR dampers have a low cost [10], and with few moving parts, are reliable. Moreover, combined with the low power requirements and inherent stability due to their inability to introduce energy to the system, are an attractive solution for control of civil structures [20,43]. All these features make MR dampers promising as actuators controlled by the voltage or current, that can be used in different engineering fields [52].

In civil engineering applications, the expected damping forces and displacements are rather large in magnitude. Therefore, MR dampers primarily operating under direct shear mode or squeeze mode might be impractical. Usually valve mode (tube/linear MR dampers) or its combination with direct shear mode are employed [118].

1.2.1 Types of linear MR dampers

There are four main types of MR dampers; mono tube, twin tube, double-ended, and sponge-type [88]. A mono tube MR damper, shown in Figure 1.7, has only one MR fluid reservoir and an accumulator mechanism to accommodate changes in volume resulting from piston rod movement. The accumulator piston provides a barrier between the MR fluid and a compressed gas (usually nitrogen) that accommodates the volume changes that occur when the piston rod enters the housing. The twin tube MR damper has two fluid reservoirs, one inside of the other, as shown in Figure 1.8. In this configuration, the damper has an inner and outer housing. The inner housing guides the piston rod assembly, in exactly the same manner as in a mono tube damper. The volume enclosed by the inner housing is the inner reservoir; the volume that is confined by the space between the inner housing and the outer housing is the outer reservoir. The inner reservoir is filled with MR fluid so that no air pockets exist.

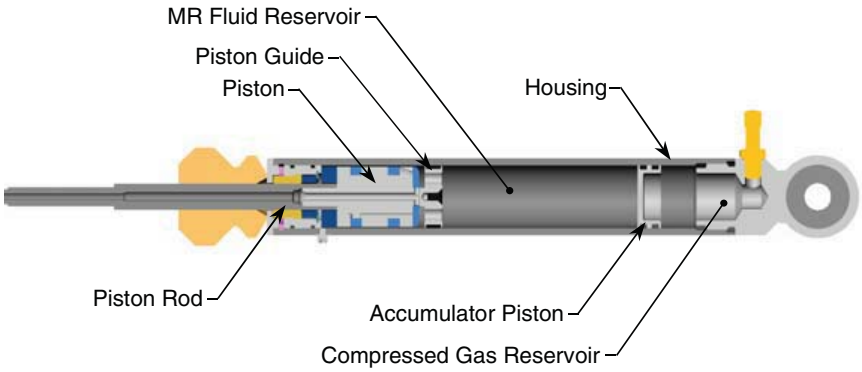

Figure 1.7: Mono tube MR damper [88].

An outer reservoir that is partially filled with MR fluid helps to accommodate changes in volume due to piston rod movement. Therefore, the outer tube in a twin tube damper serves the same purpose as the pneumatic accumulator mechanism in a mono tube damper. In practice, a valve assembly, or a 'foot valve', is attached to the bottom of the inner housing to regulate the flow of fluid between the two reservoirs. As the piston rod enters the damper, MR fluid flows from the inner reservoir into the outer reservoir through the compression valve, which is part of the foot valve assembly. The amount of fluid that flows from the inner reservoir into the outer reservoir is equal to the volume displaced by the piston rod as it enters the inner housing [88]. As the piston rod withdraws from the damper, MR fluid

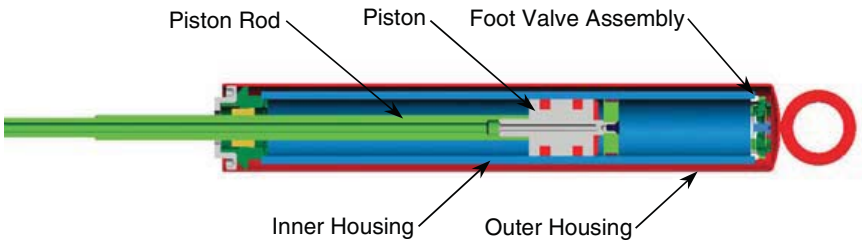

Figure 1.8: The twin tube MR damper [88].

flows from the outer reservoir into the inner reservoir through the return valve, which is also part of the foot valve assembly.

The third type of MR damper is called a double-ended damper, since a piston rod of equal diameter protrudes from both ends of the damper housing. Figure 1.9 shows a section view of a typical double-ended MR damper. Since there is no change in volume as the piston rod moves relative to the damper body, the double-ended damper does not require an accumulator mechanism [88]. Double-ended MR dampers have been used for bicycle applications [2], gun recoil applications [3], and for controlling building sway motion caused by wind gusts and earthquakes [28].

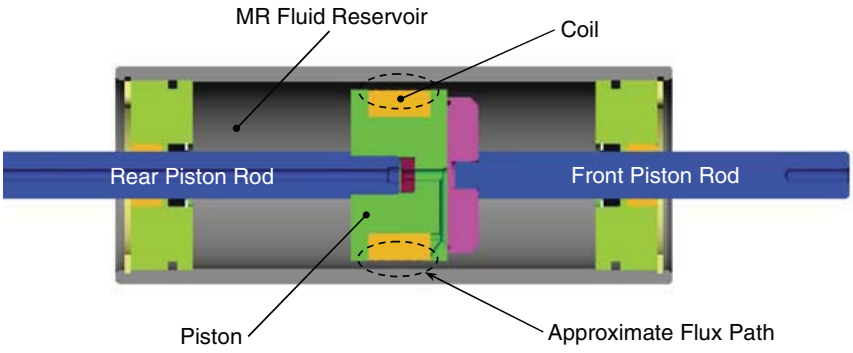

Figure 1.9: The double-ended damper [88].

The final type of MR damper is called a sponge-type damper (Fig. 1.10). An MR sponge damper contains MR fluid in an absorbent matrix such as sponge, open-celled foam, or fabric. The sponge keeps the MR fluid located in the active region of the device where the magnetic field is applied. The device is operated in a direct shear mode with a minimum volume of MR fluid.

1.3 Models of MR dampers

Memory-dependent, multi-valued relation between force and deformation, i.e., hysteresis, is observed in MR dampers. Many

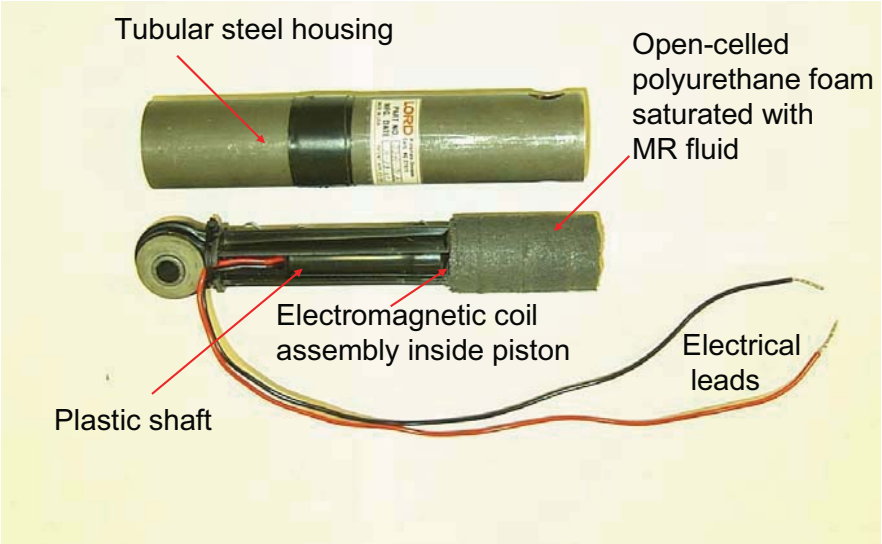

Figure 1.10: The sponge-type damper [59].

mathematical models have been developed to efficiently describe such behavior for use in time history and random vibration analysis. High-accuracy models for MR dampers can be designed using two different model families: semi-physical models [89, 101], and black-box models [34, 111]. Semi-physical models use a simplified model of the physical device, and then use some kind of measurements for identifying free parameters of the model. The black-box model, in contrary, is a strategy for investigating a complex object or device without knowledge or assumptions about its internal make-up, structure, parts or model.

Some of the most known models to describe the hysteretic behavior of MR dampers are the Bingham model and its extended versions, the Bouc-Wen model, the Dahl model, the modified LuGre model and some other non-parametric models [93]. Although a few quasi-static models have been proposed and shown to describe reasonably well the MR damper force-displacement relation, they were unable to model its nonlinear force-velocity behavior [118]. More accurate dynamic models were developed and can be divided in two categories: non-parametric and parametric models. Description of several of

these models are presented in [101, 54, 118].

1.3.1 Non-parametric models

Non-parametric models are based on device performance alone. They usually require a large amount of experimental data showing the fluid response to different loads under different operation conditions [54]. Proposed models in this category are based on Chebyshev polynomials [30, 65, 13], neural-networks [15, 62, 106, 125], neuro-fuzzy systems [96, 25, 37], for example. Neural-networks have been able to reproduce the nonlinear MR fluid behavior very closely. This, however, requires the use of input-output data sets obtained from experimental results or from a mathematical simulation of the system to be modeled. Chang and Roschke [15] proposed a multi-layer perception (MLP) network for the modeling of the MR dampers. MLP networks are one of the most commonly used neural network types, which have the particularity of using only a single nonlinear function. They have also been shown to accurately reproduce simple and complex systems. Neuro-fuzzy models are yet another example of non-parametric models proposed for emulating MR dampers' behavior. Since these devices are highly nonlinear, fuzzy logic has been proposed as an alternative to the computationally expensive models currently used. Neural-networks were then used to adjust the fuzzy logic parameters. Fuzzy logic incorporates human knowledge of the system into the controller, by use of membership functions, which are sets defining imprecise or vague concepts, such as: *large, weak, hard, moderate*, etc. The desirable output is determined based on fuzzy information of the inputs, much like the human brain makes decisions. Although several non-parametric models were shown to effectively reproduce MR damper behavior, their application is often hindered by their complexity and the extensive amount of experimental data required for training and/or model validation. Parametric models have therefore been more commonly

employed in simulations and in the development of control algorithms.

1.3.2 Parametric models

Parametric models consist of arrangements of mechanical elements such as springs and dashpots to emulate the device behavior. The parameters of these elements are determined by fitting experimental results. One of the first parametric models developed was the Bingham model (Figure 1.11, left), which consists of a Coulomb frictional element in parallel with a dashpot (viscous element) [104, 105]. The force generated by the model is:

$$f = f_y \mathrm{sgn}(\dot{x}) + c_0 \dot{x} \tag{1.1}$$

where f_y is the yield force, related to the fluid yield stress, c_0 is the damping coefficient and $\dot{x}$ is the piston velocity. Both f_y and c_0 depend on the applied voltage. Although this model accurately describes the fluid behavior beyond the yield point, it does not capture its behavior in the pre-yield region [101, 54].

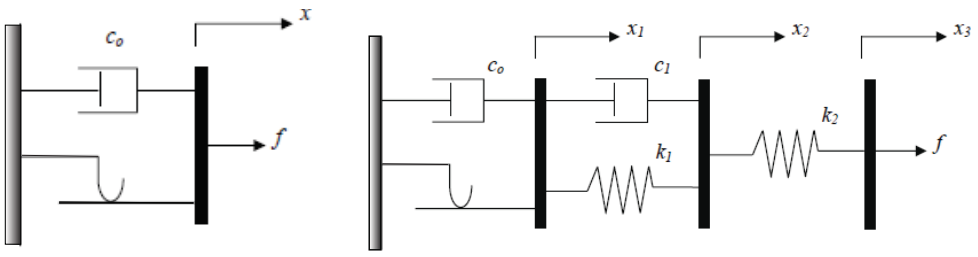

Figure 1.11: Left: Bingham model, Right: Gamota and Filisko model.

The Bingham model is based on the assumption that the MR (and electrorheological/ER) fluid damper behaves in viscoplastic way. Gamota and Filisko [33] discovered that the MR (and ER) fluid has mixed viscoelastic and viscoplastic behavior,

and thus proposed an extension of the Bingham model. It consists in adding a standard linear solid model in series with the original Bingham model (Figure 1.11, right). The force in the system can be described by:

$$f = \begin{cases} k_1(x_2 - x_1) + c_1(\dot{x}_2 - \dot{x}_1) \\ c_0\dot{x}_1 + f_y \text{sgn}(\dot{x}_1) & |f| > f_y \\ k_2(x_3 - x_1) \end{cases} \tag{1.2}$$

$$f = \begin{cases} k_1(x_2 - x_1) + c_1\dot{x}_2 \\ k_2(x_3 - x_2) & |f| \leq f_y \end{cases} \tag{1.3}$$

where k_1, k_2, and c_1 are the parameters associated with the linear solid model, c_0 is the damping coefficient for the Bingham model, and f_y is the yield force. Note that when $|f| \leq f_y$, $\dot{x}_1 = 0$. Although force-velocity behavior was found to more closely resemble experimental results, the fluid behavior when the velocity is close to zero is still not accurately reproduced. It was also observed by [101] that the governing Equations (1.2)-(1.3) are extremely stiff, making them difficult to deal with numerically. Numerical integration of them for the parameters given in [101] required a time step on the order of 10^{-6} sec. Note that a decrease in the damping, c_1, can produce the nonlinear roll-off observed in the experimental force-velocity relationship as the velocity approaches zero, but then even smaller time steps are required to simulate the system. The numerical challenges of this model constitute its main shortcoming, which was also noted in [31].

To improve these models, Spencer et al. [101] proposed a model that is numerically tractable and predicts response well. As shown in Figure 1.12 left, schematically, this model combines the Bouc-Wen model, which was originally proposed by Bouc [11, 12] and later generalized by Wen [111], and a spring-dashpot model, which are for the hysteretic behavior and the linear viscoelastic behavior of the MR damper, respectively. The model has the advantage of computational simplicity, because only one auxiliary nonlinear differential equation is needed to describe

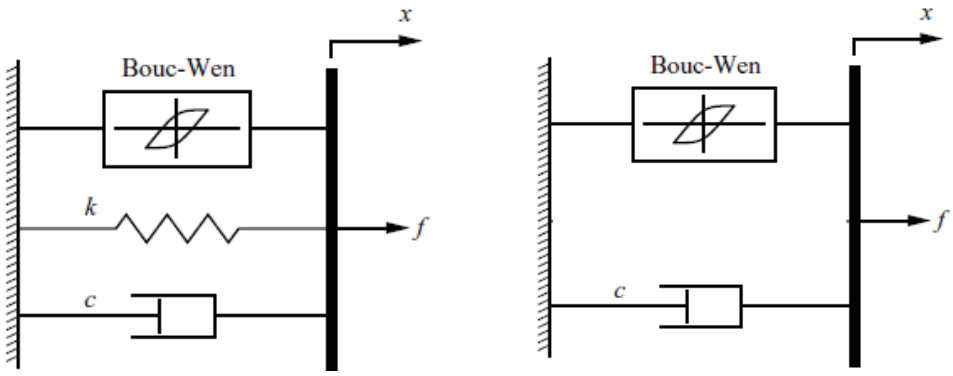

Figure 1.12: Left: Simple Bouc-Wen model, Right: Shear MR model.

the hysteretic behavior. The model has also good equivalency between complexity of model itself and the accuracy of the results. Moreover, closed-form expressions are available for the coefficients of the equivalent linear system [112]. The model is also versatile in describing various characteristics of hysteretic behavior, e.g., degrading of stiffness and strength and the pinching effect [6, 4, 85, 32], biaxial hysteresis [87], and asymmetry of the peak restoring force [110].

It has been pointed out that the Bouc-Wen class models are not in agreement with the requirements of classical plasticity theory [9], and may produce negative energy dissipation when the unloading-reloading process occurs without load reversal [14, 107]. Nevertheless, the Bouc-Wen class models have been widely used in the field of structural engineering, since they greatly facilitate deterministic and stochastic dynamic analysis of real structures with reasonable accuracy [99].

The Bouc-Wen model has been successfully used for modeling hysteretic systems. This model expresses the force generated by the damper as:

$$f = c_0\dot{x} + k_0 x + \alpha z \tag{1.4}$$

where c_0 is the damping coefficient, k_0 is the linear spring parameter, α is the Bouc-Wen parameter associated with the yield stress of the MR fluid and z is an evolutionary variable that accounts for the history dependence of the response and satisfies the following equation:

$$\dot{z} = A\dot{x} - \beta\dot{x}|z|^n - \gamma|\dot{x}|z|z|^{n-1} \tag{1.5}$$

Parameters A, β, γ, and n determine the linearity in the unloading region as well as the transition smoothness from the pre-yield to the post-yield regions. There is another version of such simple model which belong to the shear mode type MR dampers. For this type the elastic part is omitted because of its very small influence in the resulted damping force, therefore, the characteristic of damper is modeled by hysteresis and viscous terms (Figure 1.12, right):

$$f = c_0\dot{x} + \alpha z \tag{1.6}$$

To improve the accuracy of the force-velocity behavior of the MR dampers, a modified Bouc-Wen model, also referred to as phenomenological model, was proposed by Spencer et al. [101]. This model consists in the addition of a dashpot in series with the original Bouc-Wen model and a spring in parallel with the entire system (Figure 1.13). The force produced by the damper can be described by:

$$f = \alpha z + c_0(\dot{x} - \dot{y}) + k_0(x - y) = c_1\dot{y} + k_1(x - x_0) \tag{1.7}$$

where x is the damper displacement, y is an internal displacement of the damper, α is the Bouc-Wen parameter describing the MR fluid yield stress, c_0 represents the viscous damping at large velocities, k_0 the stiffness at large velocities, k_1 is introduced to model the damper force due to the accumulator, and c_1 to reproduce the roll-off occurring in the experimental data when velocities are close to zero. x_0 is the initial displacement of spring k_1. Evolutionary variable z and variable y satisfy the

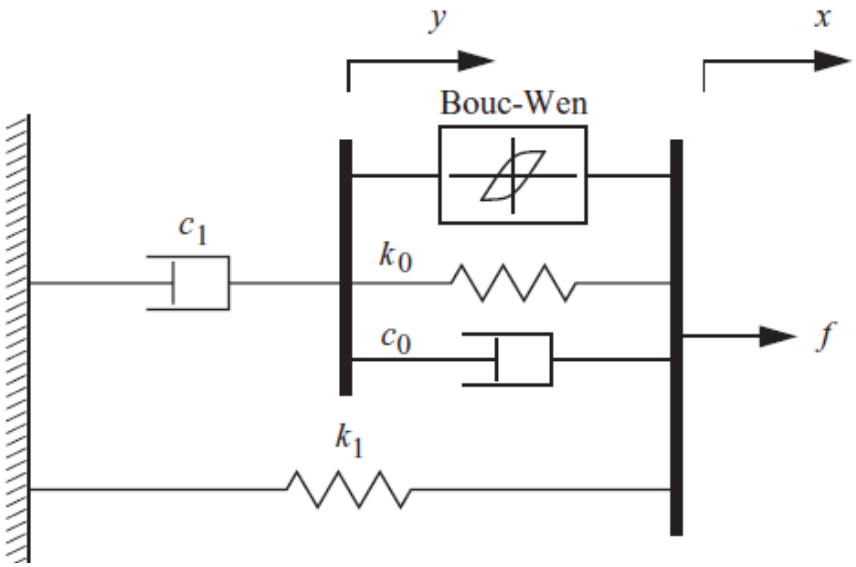

Figure 1.13: Phenomenological model of MR damper [101].

following equations:

$$\dot{z} = A(\dot{x} - \dot{y}) - \beta(\dot{x} - \dot{y})|z|^n - \gamma|\dot{x} - \dot{y}|z|z|^{n-1} \tag{1.8}$$

$$\dot{y} = \frac{1}{c_0 + c_1}\alpha z + c_0\dot{x} + k_0(x - y) \tag{1.9}$$

It is important to notice that variables α, c_0, and c_1 are functions of the input current or voltage to the damper.

The typical form of the Bouc-Wen hysteresis model is

$$\dot{z}(t) = A\dot{x}(t) - \beta\dot{x}(t)|z(t)|^n + \gamma|\dot{x}(t)|z(t)|z(t)|^{n-1} \tag{1.10}$$

in which A, β, γ, and n are model parameters that control the hysteresis shape of the system. There is another equivalent version of this relation, which introduces another parameter Y, to highlight the effect of the yielding displacement of the system on the resulted behavior:

$$\dot{z}(t) = Y(A\dot{x}(t) - \beta\dot{x}(t)|z(t)|^n + \gamma|\dot{x}(t)|z(t)|z(t)|^{n-1}) \tag{1.11}$$

where Y is the yielding displacement of the device. Reference

[111] presents the shape of the hysteresis loop for different values of the model parameters.

In general any model requires two important characteristics to be a good candidates for representation of a real hysteric device. Firstly, for any bounded input x, the output resulted force from the model must be bounded. Secondly, the model has to reproduce dissipation energy property in order to represent adequately the physical behavior of a real damping system like MR damper. Reference [48] has shown that these conditions are not generally satisfied by the typical form of the Bouc-Wen hysteresis model. To cope with this drawback, a normalized Bouc-Wen model was proposed [48].

Next section is dedicated to explain this normalized version of the Bouc-Wen model for hysteresis systems, which is the core of the proposed new parameter identification process.

1.4 Normalized Bouc-Wen model

The normalized version of the Bouc-Wen model ([48], p.39) is an equivalent representation of the original Bouc-Wen model [111]. The motivation of this new form is due to the fact that the input-output behavior of the original Bouc-Wen model is not described by a unique set of its parameters ([48], p.40, Lemma 2). This fact makes it difficult to compare results of different identification methods by comparing the identified parameters. The normalized version of the model has less number of parameters thus eliminating the overparametrization present in the original one, and relates the output force to the input displacement in a very unique form.

Consider a physical system with hysteresis component. The Bouc-Wen model represents the hysteresis behavior of this system in the form

$$\Phi_{BW}(x)(t) = \alpha k x(t) + (1-\alpha) D k z(t) \tag{1.12}$$

$$\dot{z} = D^{-1}(A\dot{x} - \beta|\dot{x}|z|z|^{n-1} - \gamma\dot{x}|z|^n) \tag{1.13}$$

where k controls the initial tangent stiffness, α controls the ratio of post-yield to pre-yield stiffness and z is the hysteresis parameter. D is the yield displacement and A, n, β and γ are parameters that control the shape of hysteresis loop of the system. Ikhouane and Rodellar have shown that this form is not always bounded input-bounded output (BIBO) model and not always represents an energy dissipation for a true hysteresis system ([48], p.14). Not BIBO model means that there exist some bounded input displacement x such that the Bouc-Wen model delivers unbounded output response $\Phi_{BW}(x)$ ([48], p.15, Example 1). Indeed, while the model may give a good approximation of a true hysteresis loop for a *specific* input excitation used with a specific set of parameters, they may not be appropriate to represent the behavior of the same system under general input excitation. To cope with the case of boundedness of the output, [48] offers some conditions, in the form of inequalities, for model parameters. Table 1.1 shows these conditions. It shows that classes I to V are BIBO stable. Each class is composed of a range for the Bouc-Wen model parameters and a range for the initial condition $z(0)$ of the hysteresis part of the model. Moreover, for all classes, the boundedness of the hysteresis signal $z(t)$ depends only on the parameters A, n, β and γ, and is independent of the boundedness of the input signal $x(t)$.

Moreover, [48] shows that, for classes I and II of Table 1.1, the states $x(t)$ and $z(t)$ go asymptotically to constant values and that the velocity $\dot{x}$ goes to zero. This means that both classes are good candidates for the description of the real physical behavior of a structural isolation device ([48], Theorem 2, p.25). Finally, the class I Bouc-Wen model is shown to be passive. This implies that this class is a good candidate in order to represent the physical passivity behavior in structural or mechanical devices.

Although, the adequate condition for a mathematical model can be found in class I of the Bouc-Wen hysteresis model, from parameter identification point of view there is a drawback in it. The input-output behavior of Bouc-Wen model is not described

Table 1.1: Classification of the BIBO-stable Bouc-Wen models [48]

Case		Ω	**Upper bound on** $\lvert z(t)\rvert$	**Class**
$A>0$	$\beta+\gamma>0$ and $\beta-\gamma\geq 0$	$\mathbb{R}$	$\max(\lvert z(0)\rvert, {z_0}^a)$	I
	$\beta-\gamma<0$ and $\beta\geq 0$	$[-{z_1}^b, z_1]$	$\max(\lvert z(0)\rvert, z_0)$	II
$A<0$	$\beta-\gamma>0$ and $\beta+\gamma\geq 0$	$\mathbb{R}$	$\max(\lvert z(0)\rvert, z_1)$	III
	$\beta+\gamma<0$ and $\beta\geq 0$	$[-z_0, z_0]$	$\max(\lvert z(0)\rvert, z_1)$	IV
$A=0$	$\beta+\gamma>0$ and $\beta-\gamma\geq 0$	$\mathbb{R}$	$\lvert z(0)\rvert$	V
All other cases		$\emptyset$		

$^a z_0 \triangleq \sqrt[n]{A/(\beta+\gamma)}$
$^b z_1 \triangleq \sqrt[n]{A/(\gamma-\beta)}$

by a unique set of parameters ([48], Lemma 2, p.40). To alleviate this drawback, users of the Bouc-Wen model often fix some parameters to arbitrary values, then try to find the rest [84]. Others compare the shape of the final force-displacement, or force-velocity with the corresponding plot resulted from tests [101]. Thus, it is necessary to elaborate some equivalent *normalized model* whose parameters define in a unique way the input-output behavior of it, allowing a parametric-base comparison of identification methods for the model. To this end, [48] defines

$$w(t) = \frac{z(t)}{z_0} \tag{1.14}$$

where $z_0 \triangleq \sqrt[n]{A/(\beta+\gamma)}$. Thus the model (1.4)-(1.5) can be written in the form

$$\Phi_{BM}(x)(t) = \kappa_x x(t) + \kappa_w w(t) \tag{1.15}$$

$$\dot{w}(t) = \rho(\dot{x}(t) - \sigma|\dot{x}(t)||w(t)|^{n-1}w(t) + (\sigma-1)\dot{x}(t)|w(t)|^n) \tag{1.16}$$

where

$$\rho = \frac{A}{Dz_0} > 0, \quad \sigma = \frac{\beta}{\beta+\gamma} \geq 0,$$
$$\kappa_x = \alpha k > 0, \quad \kappa_w = (1-\alpha)Dkz_0 > 0 \tag{1.17}$$

Table 1.2: Classification of the BIBO, passive and thermodynamically consistent normalized Bouc-Wen models [48]

Case	Ω	**Upper bound on** $\lvert w(t)\rvert$	**Class**
$\sigma \geq \frac{1}{2}$	$\mathbb{R}$	$\max(\lvert w(0)\rvert,1)$	I

Equations (1.15) and (1.16) define the so-called normalized form of the Bouc-Wen hysteresis model. In this model the variable $z(t)$ has been scaled to unity. The classification of this normalized form needs only one parameter σ as shown in the Table 1.2. This normalized model has less number of parameters thus eliminating the overparametrization exiting in the original model and relates the output force Φ_{BM} to the input displacement x in the unique form. The parameters $\rho > 0$, $\sigma > 1/2$, and $n \geq 1$ control the shape of the hysteresis loop. As its corresponding parameter, $z(t)$, the state $w(t)$ has not a physical meaning.

Chapter 2

Bouc-Wen hysteresis model identification

2.1 Introduction

The Bouc-Wen model is one of the most popular models used to describe the hysteretic behavior of structural damping devices. This model employs an internal variable, z, which has the forms (1.10) or (1.11). This variable depends on four or five parameters, A, n, β, γ and also in some expressions Y. The goal of all parameter identification methods is to find these parameters such that the output force of the model matches as close as possible to the real device responses. The reference [48] presents a normalized version of the Bouc-Wen hysteresis model, which has less parameters and can eliminate the overparametrization problem present in the original model. It has been applied in a specific class of shear type MR dampers. This chapter tries to make the method more general and applicable to any type of MR dampers. Then a modified identification technique will be presented based on this new model.

2.2 Literature review

Identifying the Bouc-Wen model parameters consists in proposing a signal input (or several signal inputs) and an identification

algorithm that uses the measured output of the model along with that input to determine the unknown model parameters. This problem has stirred a lot of research effort due to its difficulty being nonlinear and non-differentiable. Some identification methods have been proposed with a rigorous analysis of the convergence of the parameters to their true values, while others relied on numerical simulations and experimentation. In this section, an overview of these methods is presented.

2.2.1 Least-squares based identification

Reference [73] presents a three-stage identification algorithm that is a combination of sequential regression analysis, least-squares analysis and/or Gauss-Newton method along with the extended Kalman filtering technique. In the first stage of identification, assuming equivalent linear system at each time interval and by using the sequential regression analysis, the system stiffness and damping are identified. In the second identification stage, a fixed $n = 1$ is assumed, and the model parameters are identified using the least-squares method through minimizing an error function. In the third stage of identification, the extended Kalman filter technique is used to obtain identification results by using the results from the second stage as an initial guess to the third stage to speed convergence.

Paper [129] describes an iterative least squares procedure based on a modified Gauss-Newton approach to perform the parameter identification of an extended version of the Bouc-Wen model that accounts for strength and stiffness degradation. References [18, 71] present an on-line identification method based on a least-squares adaptive law. For an unknown mass m, a Bouc-Wen hysteresis element model with additional polynomial-type non-linear terms, is used to investigate the effects of persistence of excitation and of under-and overparameterization.

Paper [69] presents an adaptive on-line identification methodology with a variable trace method to adjust the adaptation gain matrix. In [72], a linear parameterized estimator is proposed for

the on-line estimation of the hysteretic Bouc-Wen model with unknown coefficients (including the parameter n). A discrete-time form then expanded. This discrete time model give rise discrete-time linearly parameterized estimator. Based on the data collected from a performance test, least-square method is used to estimate the model parameters, for each discrete frequency.

2.2.2 Kalman filter based identification

In [70], it is assumed that $n = 1$ and an extended Kalman filter is used to identify the rest of the parameters. A procedure for nonlinear system identification based on the extended Kalman filter is applied to soils under strong motion records [67]. The ground is modeled as 3DOFs hysteretic structure and the Bouc-Wen model is used in characterizing the nonlinear backbone curve of soils.

Reference [128] presents three algorithms based upon the simplex [8], extended Kalman filter [77], and generalized reduced gradient methods. The objective is to estimate the parameters of hysteresis for different classes of inelastic structures using the generalized Bouc-Wen model that accounts for degradation and pinching [5]. This model form contains 13 parameters to be identified.

In [68], an adaptive on-line identification algorithm is proposed for parametric and non-parametric identification of structural models, and is applied to a generalized Bouc-Wen model. The proposed identification methodology, a recursive least-square (Kalman filter) based algorithm, upgrades the adaptation gain matrix using an adaptive forgetting factor that is expressed as the ratio between the minimum value of the diagonal elements of the adaptation gain matrix and a set of pre-defined threshold values. This approach requires only acceleration measurements.

2.2.3 Genetic algorithm based identification

In [39], a genetic based identification algorithm is proposed. The reproduction procedure adopts the roulette wheel selection and the method of crossover and uniform mutation [1, 41].

A modification to the standard Bouc-Wen model is proposed in [60] to account for non-symmetrical hysteresis exhibited by an MR damper. The model parameters are identified by a genetic algorithm that is improved here by

1. Removing the selection stage (it is absorbed into the crossover and mutation operations).

2. Imposing a termination criterion on the basis of statistical tests which guarantees the quality of a near-optimal solution.

Reference [61] proposes an identification method based on differential evolution using simulated noise-free data and experimental data obtained from a nuclear power plant. The Bouc-Wen model parameter n is kept constant to the value 2. The used objective function is the mean square error (MSE) which is cast in the discrete normalized form.

In [76], a population-search algorithm is proposed to estimate the 13 parameters of the generalized Bouc-Wen model. With a given load-displacement trace as input, the optimization problem can be stated as the determination of the a parameter vector, such that an objective function is minimized.

2.2.4 Gauss-Newton iterative based identification

In [119], a method of estimating the parameters of hysteretic Bouc-Wen model on the based of possibly noise corrupted input-output data is proposed. In [63], Gauss-Newton iteration are used as a method of estimating the parameters of hysteretic system with slip on the basis of input-output data. The model used is called slip-lock [5] as an extended version of the Bouc-Wen model, and describes the pinching of hysteresis loops.

2.2.5 Bootstrap filter based identification

In [64], a parametric identification method is proposed for an extended form of the Bouc-Wen model that accounts for stick-slip phenomenon [5]. The method uses the bootstrap filter, a filtering method based on Bayesian state estimation and Monte Carlo method. Also, a method to decide the initial estimates of the parameters is suggested to obtain stable solutions as well as their fast convergence to the optimal values.

2.2.6 Identification using periodic signals

Reference [84] proposes a frequency domain parametric identification method of non-linear hysteretic isolators. The hysteretic restoring force is identified by taking measurements of both the external excitation and the displacement response $x(t)$ (or the acceleration $\ddot{x}$ alternatively).

In [47, 45], an identification method for the normalized Bouc-Wen model is proposed. Using the analytical description of the hysteresis loop developed in [47], an algorithm is proposed along with its analytical proof. It consists in exciting the Bouc-Wen model with two periodic signals with a loading-unloading shape (wave periodic) which give rise asymptotically to a hysteretic periodic response. The obtained two limit cycles are then used as input to determine exactly the unknown parameters.

2.2.7 Simplex method based identification

Reference [92] presents a two-step system identification approach that does not require the semiactive device to be tested apart from the structure, but rather mounted into it. It consists in (i) identification of a model for the primary structure without the semiactive damper attached; (ii) installation of the semiactive damper in the structure and simultaneous identification of the remaining parameters for the primary structure and of a model

for the semiactive control device. The simplex algorithm is employed to optimize the dynamical parameters. In [38], the simplex and Levenberg-Marquardt optimization methods are used to fit experimental data with curves given by a Bouc-Wen model in a dynamic suspension modeling problem.

2.2.8 Support vector regression based identification

Reference [129] proposes a non-linear structural identification scheme to identify the Bouc-Wen type structures. It produces the unknown power parameter n of the model by the model selection strategy, transforms the non-linear differential equation into a linear problem through the high order Adam Moulton implicit equation [97], and utilizes the support vector regression data processing technique to solve non-linear structural parameters.

2.2.9 Constrained nonlinear optimization based identification

Paper [95] uses the Bouc-Wen model to describe magnetorheological dampers, and proposes a methodology of identification to determine the model parameters. The value $n = 2$ is supposed and the model estimation problem is reduced to an optimization problem where the performance index is a classical normalized L_2-norm of the output fitting error. In [114], [109] and [120] a constrained nonlinear optimization are used for identification purpose.

2.2.10 Non-parametric identification

In [78], the Bouc-Wen nonlinear hysteresis term is approximated by a power series expansion of suitable basis function, then the coefficients of the function are determined using standard least-squares methods. In [71], a method relying on deconvolution to estimate the non-linear hysteretic force z from experimental records is used.

Reference [55] develops a computational algorithm for the modeling and identification of the MR dampers by using wavelet systems to handle the nonlinear terms. By taking into account the Haar wavelets, the properties of integral operational matrix and of product operational matrix are introduced and utilized to find an algebraic representation form instead of the differential equations of the dynamical system.

2.3 Normalized Bouc-Wen model of MR dampers

The identification method presented in [48] is based on a model which has two terms, elastic and hysteretic ones, in the form

$$F(x)(t) = \kappa_x x(t) + \kappa_w w(t) \tag{2.1}$$

$$\dot{w}(t) = \rho(\dot{x}(t) - \sigma|\dot{x}(t)||w(t)|^{n-1}w(t) + (\sigma - 1)\dot{x}(t)|w(t)|^n) \tag{2.2}$$

where x is the displacement, F is the output force and w is the hysteretic variable. In order to identify the parameters, one has to use input signals $x(t)$ that are wave T-periodic ([48], p.38). The characteristics of these signals are given in Figure 2.1. It has shown that, under this type of signal waves, the output force goes asymptotically to a periodic limit function, $\bar{F}$ ([48], Theorem 3, p.47). The summarized parameter identification method is presented in the Appendix A.

To show the efficiency and accuracy of the model, [48] presents an application to a shear type MR damper. The model is modified in the form

$$F(x)(t) = \kappa_x(v)\dot{x}(t) + \kappa_w(v)w(t) \tag{2.3}$$

$$\dot{w}(t) = \rho(\dot{x}(t) - \sigma|\dot{x}(t)||w(t)|^{n-1}w(t) + (\sigma - 1)\dot{x}(t)|w(t)|^n)$$

note that in this form the elastic term has been replaced with a viscous term.

A variation of this method has been studied by Rodríguez et al. [93, 94]. They identified both small- and large-scale MR

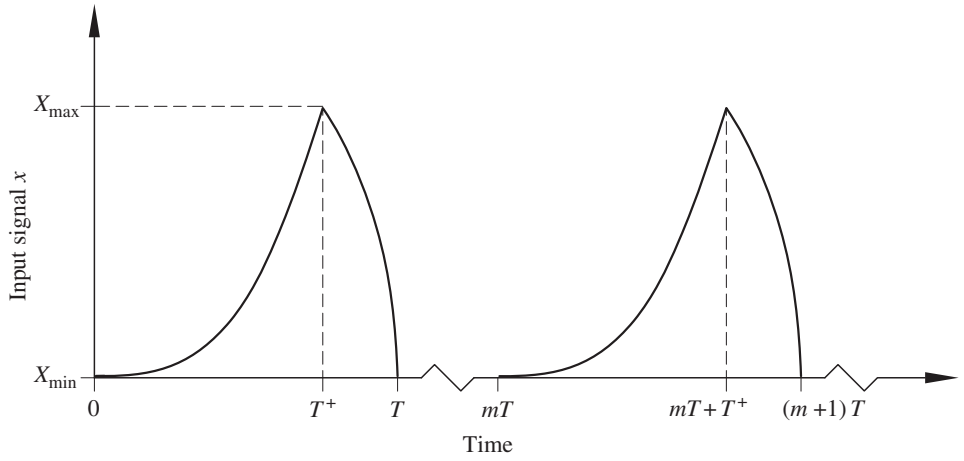

Figure 2.1: A sample T-wave periodic signal.

dampers based on the normalized Bouc-Wen model, according to the parameter identification method proposed in [48]. In both cases a drawback has been observed. They found that if the MR damper has a viscous friction ($\kappa_x(v)\dot{x}(t)$) small enough with respect to the dry friction ($\kappa_w(v)w(t)$), large relative errors can be observed in the identification of the parameter κ_x. To alleviate this drawback, a proper modification was introduced. This modification is established based on the plastic branch of the resulted force-velocity plot from test data when the excitation displacement is large enough. Therefore, the value of κ_x can be captured from the slop of the plastic branch of this plot by a simple numerical regression. The rest of the identification procedure can be followed similar to the main algorithm [93, 94].

The results of the above modified method show good agreement with the output laboratory test data of the devices, but still cannot be applied to general types of MR dampers. In fact, this methodology is a good candidate for identification of shear type MR dampers. In this specific category of MR dampers, because of the internal mechanism of operation, the elastic characteristic does not exist. The response of such devices to the external excitation is highly based on the viscous behavior together with the non-linearity, which comes from the magnetorheological fluid. On the other hand, in the structural application of

the MR dampers, these shear type devices cannot offer adequate damping force for medium to large scale structures. So, in practice the so called linear or tube type MR dampers are under consideration. In majority of these linear shape MR dampers, the device has an accumulator, which is normally filled with nitrogen. The role of this accumulator has been mentioned in Section 1.2.1. The effect of this accumulator is to add an elastic behavior to the device. As a consequence, the resulted damping force generated in such an MR dampers must be modeled, in general, with three terms: elastic, viscous and hysteretic ones.

This type of behavior has been reported in the literature (for example [23, 58, 24, 62, 21]). Before highlighting the effect of this new added term, let us look at the resulted plots for force-displacement and force-velocity graphs of these two category of MR dampers in the literature. There is not any direct mention about the name or category of the used devices, but a clear difference between these two groups of plots can be easily found.

Figure 2.2 shows two examples of the force-displacement graph. There are two main difference between these two plots. The first one is about the offset of the left plot, which is not the topic of this study, and the other is about the general shape of them. It seems that the left graph has a sort of inclination with respect to the horizontal line. In Figure 2.3 also two sample plots, for force-velocity, are shown. Regardless of the offset effect, these two plots have a clear difference in the plastic branches. In the left plot, the loading and unloading curves are clearly apart from each other. But this is not the case in the right plot. Next section is devoted to find out why this behavior can be seen in some MR dampers and not in others.

2.3.1 Numerical experiment with an MR damper model

One of the reported models of MR dampers is chosen and the resulted force-displacement and force-velocity plots are presented. The model describes a shear-mode prototype MR damper tested at Washington University [121, 122]. The identified parameters

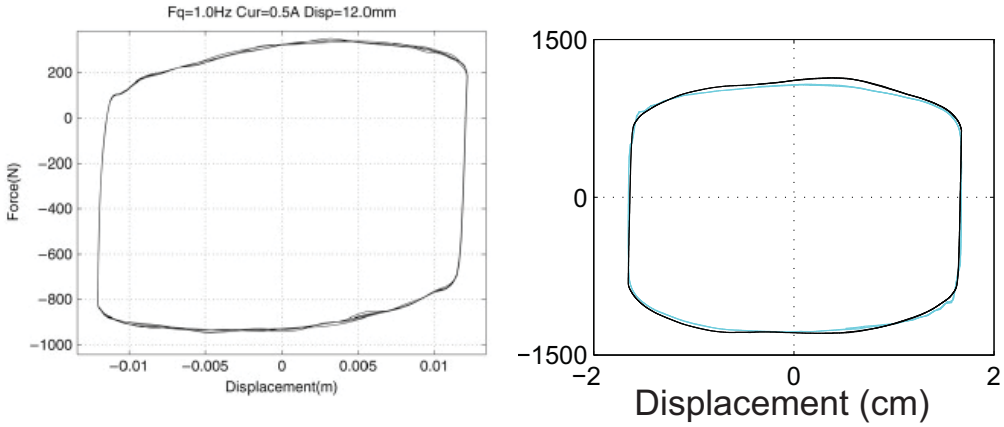

Figure 2.2: Sample Force-Displacement plots from literature. Right: Shear-type [101], Left: Non shear-type [62].

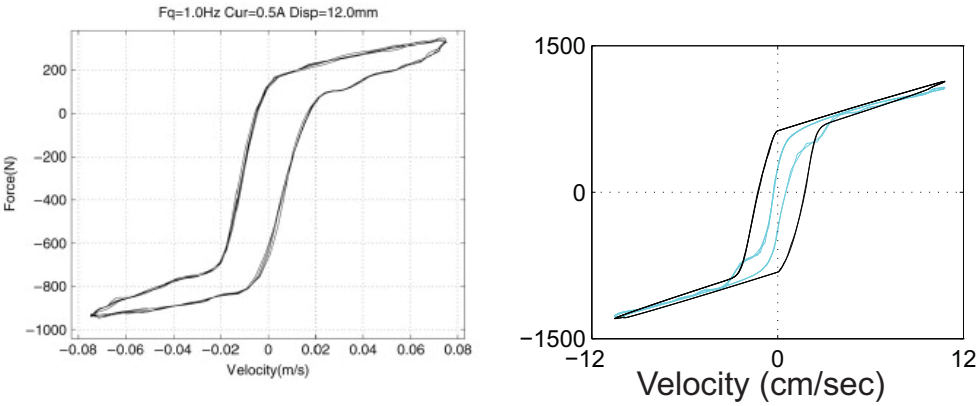

Figure 2.3: Sample Force-Velocity plots from literature. Right: Shear-type [101], Left: Non shear-type [62].

are shown in Table 2.1. Figure 2.4 shows the simulink block for simulation of the model in MATLAB®.

The equations governing the output force f predicted by this model are

$$f = C_0\dot{x} + \alpha z \tag{2.4}$$

$$\dot{z} = -\gamma|\dot{x}|z|z|^{n-1} - \beta\dot{x}|z|^n + A\dot{x} \tag{2.5}$$

Table 2.1: Sample MR damper parameters [50]

Parameter	C_{0a}	C_{0b}	α_a	α_b	γ	β	A	n
Value	0.0064	0.0052	8.66	8.86	300	300	120	2
Unit	$\frac{Nsec}{cm}$	$\frac{Nsec}{cmV}$	$\frac{N}{cm}$	$\frac{N}{cmV}$	cm^{-2}	cm^{-2}		

where z is an evolutionary variable that accounts for the history dependence of the response. The model parameters depend on the voltage v to the current driver as follows:

$$\alpha = \alpha_a + \alpha_b u \quad and \quad C_0 = C_{0a} + C_{0b} u \tag{2.6}$$

where u is given as the output of the first-order filter

$$\dot{u} = -\eta(u - v) \tag{2.7}$$

Equation (2.7) is used to model the dynamics involved in

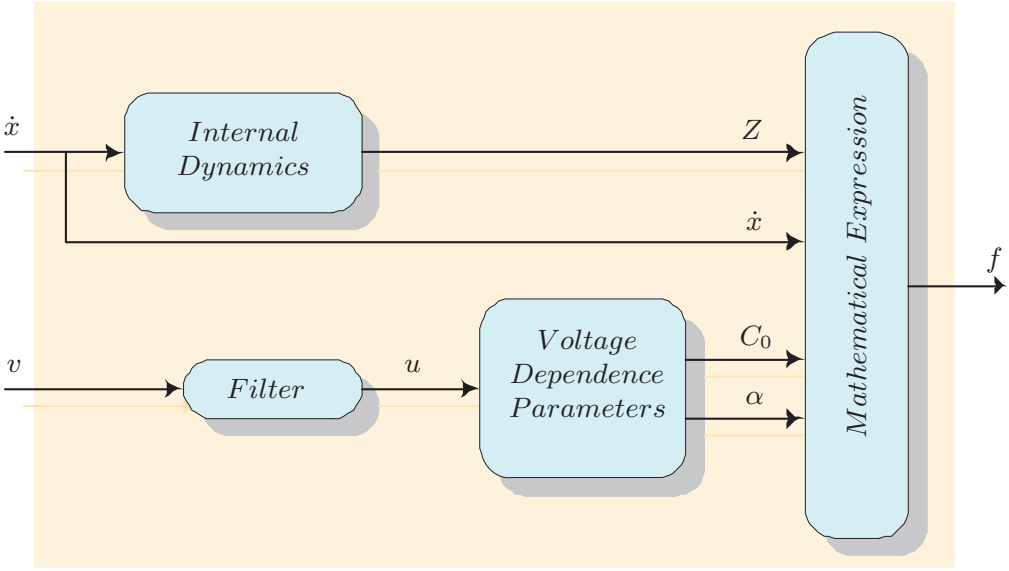

Figure 2.4: Sample MR damper simulink block.

reaching rheological equilibrium and in driving the electromagnet in the MR damper [122].

Figure 2.5 shows the resulted plot for the force-displacement relation of the model for different levels of command voltage: 0, 0.5, 1.0, 2.5 and 5 Volts. As it is clear, the resulted curve is completely horizontal.

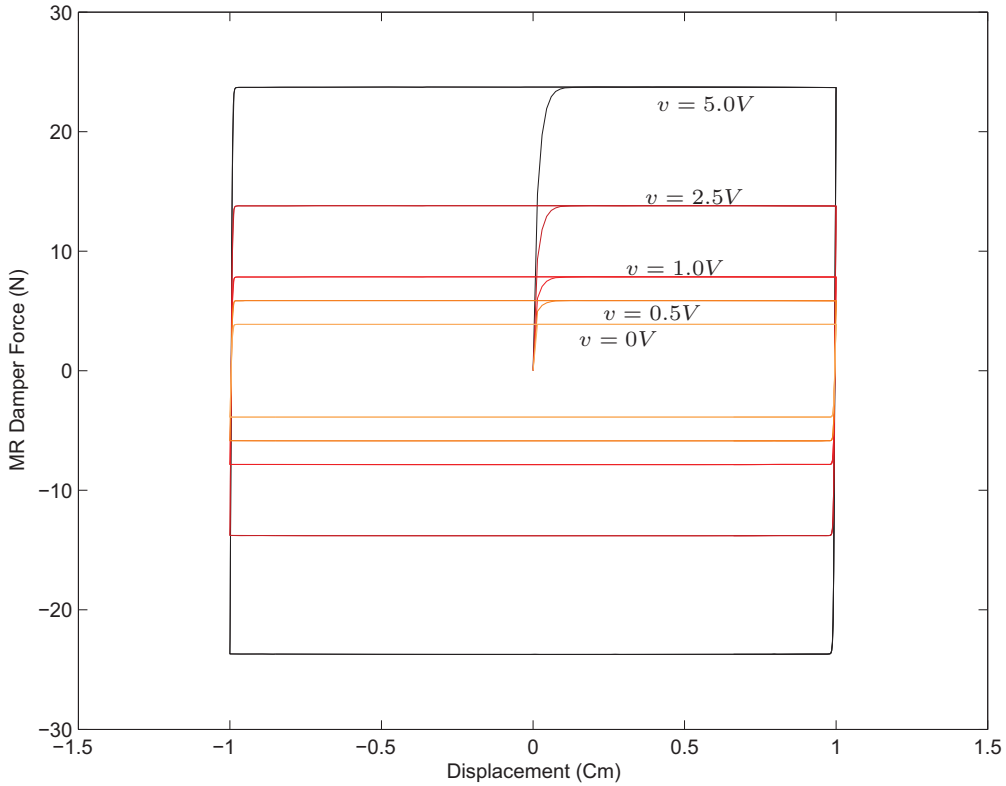

Figure 2.5: Force-Displacement plot of sample model.

Figure 2.6 shows the results of the same numerical test for the force-velocity diagram. In this case the status of the plastic branch is under consideration. This part is a line for all levels of command voltage. It means that the values of resulted force of the MR damper in both the loading and unloading stages in this range are equal. Another information which can be found from this graph is about the parameter C_0 that multiplies the velocity $\dot{x}$. Here the plastic branch seems very close to horizontal

line, and this means that the coefficient C_0 of the viscous term is small (a view to the value of parameters C_0 in the Table 2.2 can support this result).

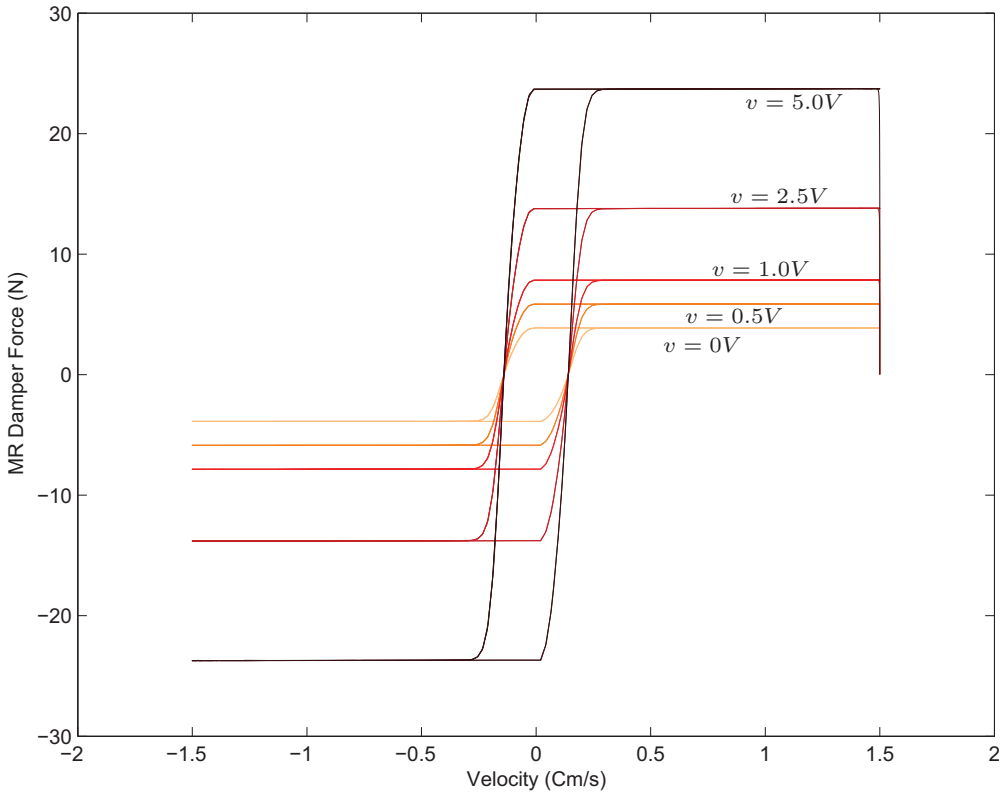

Figure 2.6: Force-Velocity plot of sample model.

To show the effect of the displacement term in the resulted force and the corresponding cycle, let's introduce a new elastic term to the Equation (2.4). The rest of the equations will keep the same, that is,

$$f = kx + C_0\dot{x} + \alpha z \tag{2.8}$$

$$\dot{z} = -\gamma|\dot{x}|z|z|^{n-1} - \beta\dot{x}|z|^n + A\dot{x}$$

In general the displacement coefficient k can be voltage dependent, but we keep it constant to make the study as simple as possible. Therefore

$$\alpha = \alpha_a + \alpha_b u \quad , \quad C_0 = C_{0a} + C_{0b} u \quad and \quad k = k_0 \qquad (2.9)$$

$$\dot{u} = -\eta(u - v)$$

A new simulation has been done for this new model. The results corresponding to three different values of stiffness k_0 (0, 2.5 and 5 N/cm), are plotted in Figures 2.7 and 2.8. As can be seen, the effect of augmenting the value of k is making the force-displacement graph more inclined where the force-velocity plot, in the plastic branch, becomes wider.

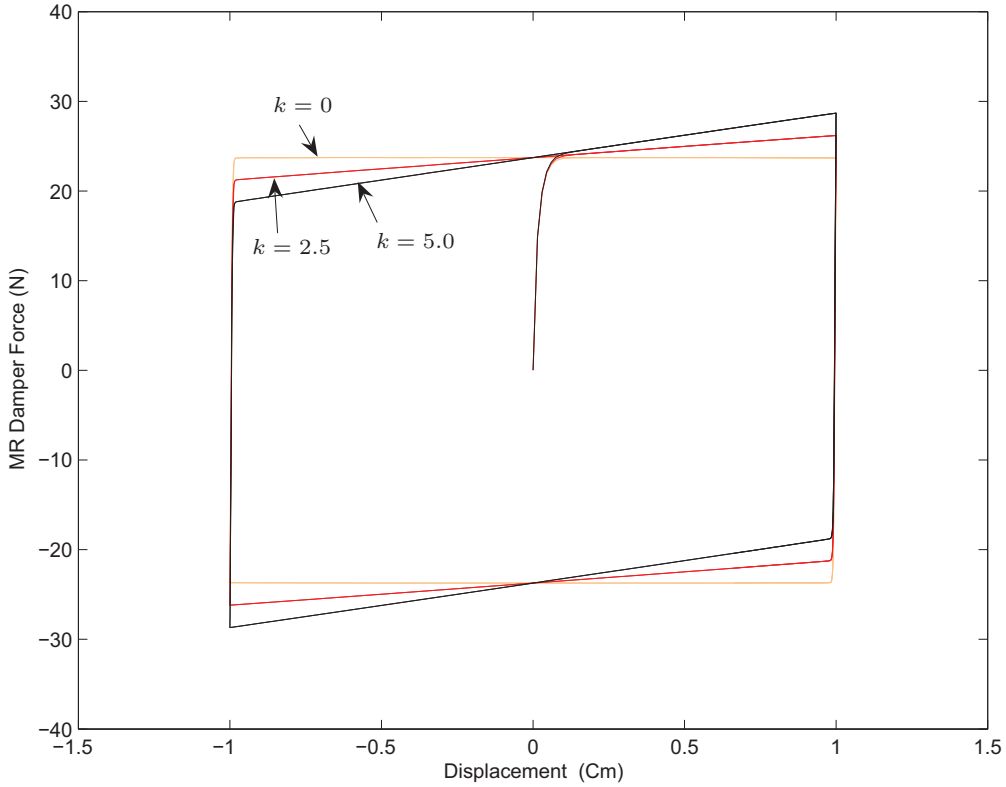

Figure 2.7: Force-Displacement plot of sample model with elastic term.

As a conclusion, having the three terms makes the Bouc-Wen model more general to be adapted to a wider range of MR dampers, specially the devices which are more effective in the

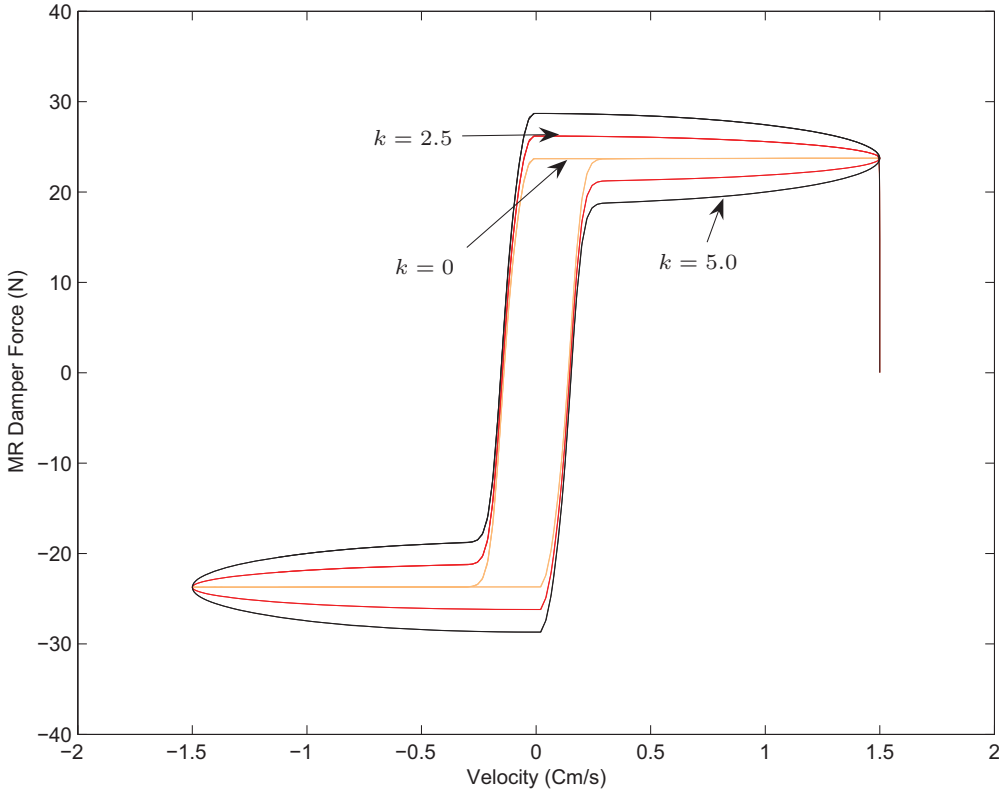

Figure 2.8: Force-Velocity plot of sample model with elastic term.

vibration control of real structures.

Next section will offer a new version of the normalized Bouc-Wen model for MR dampers, which can combine both benefits of normalization of the model and the generality.

2.4 New extended normalized Bouc-Wen model

We consider the following model:

$$F_e(x, \dot{x}, w)(t) = \kappa_x(v)x(t) + \kappa_{\dot{x}}(v)\dot{x}(t) + \kappa_w(v)w(t) \tag{2.10}$$

$$\dot{w}(t) = \rho(\dot{x}(t) - \sigma|\dot{x}(t)||w(t)|^{n-1}w(t) + (\sigma - 1)\dot{x}(t)|w(t)|^n) \tag{2.11}$$

where $F(t)$ is the output force of the MR damper, $x(t)$ and $\dot{x}(t)$ are the input displacement and velocity of the damper, respectively. The input voltage v is the applied command voltage at the coil of the MR damper. The system parameters $\kappa_x(v) > 0$, $\kappa_{\dot{x}}(v) > 0$ and $\kappa_w(v) > 0$ are the ones which define how each of the three main terms will participate in the final resulted damping force of MR damper, and generally are voltage dependent. The parameters $\rho(v) > 0$, $\sigma(v) > 1/2$ and $n(v) \geq 1$ define the manner of handling the hysteresis behavior of the device and their meaning can be found in [46]. These parameters can also be voltage dependent. Their dependency on command voltage is not highlighted in (2.11) to simplify the notation. The input-output variables of the MR damper are schematized in Figure 2.9.

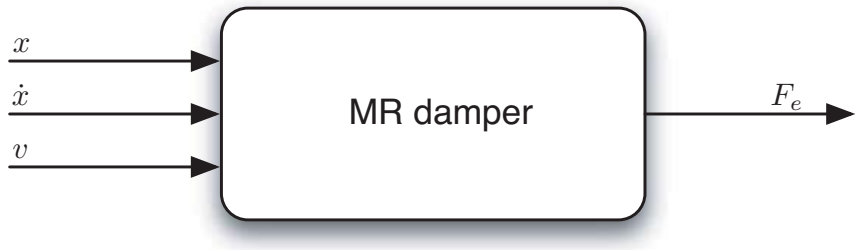

Figure 2.9: Input-output variables of the MR damper.

2.5 New parameter identification for extended normalized Bouc-Wen model

This section is concerned with the computation of the parameters of the extended model in equations (2.10)-(2.11). The proposed algorithm will be divided in two steps: (a) the estimation of the value of $\kappa_x(v)$ and (b) the estimation of the rest of the parameters based on the identification algorithm in [93] or [94].

In the parameter identification methodology, to estimate the voltage dependence of the system parameters, sets of experiments are performed for fixed values of the voltage. At each

constant voltage, the computation of the parameter κ_x can be performed graphically by considering the force-displacement diagram of the MR damper under consideration, because, this parameter is the source of inclination of the resulted plot (as it shown in Section 2.3.1). When this device is excited by a sinusoidal displacement with a large enough amplitude, the average inclination of the resulted plot gives a good estimation of this parameter. To make sure about the accuracy of the estimated value, the best way is plotting the diagram for the resulted value of $\{F_e(x, \dot{x}, w)(t) - \kappa_x x\}$ versus velocity, where κ_x is the current estimated value of this parameter. As explained in Section 2.3.1, if the measured value is a good approximation of the true value of the parameter, the plastic branch in the resulted plot will be very close to a line. The under-estimation and/or over-estimation situations, can also be traced based on the situation of the loading and unloading curves of the diagram in the plastic region of the same plot.

As an example, consider the same numerical test presented in Section 2.3.1. The chosen value for the elastic coefficient κ_x was 5 N/cm. Figure 2.10 shows the three graphs of force-velocity for the same test using the three different values for κ_x corresponding to 4.5, 5 and 5.5 N/cm in calculating the updated force $\{F_e(x, \dot{x}, w)(t) - \kappa_x x\}$. In the case of under-estimation of the parameter κ_x, the two curves of loading and unloading stages, in the plastic region, will be apart from each other (Fig. 2.10, up). For the good estimation case, the two branches overlap, which means that the estimated value is practically exact (Fig. 2.10, middle). For over-estimation case, these two curves will cross each other (Fig. 2.10, down). To estimate the rest of the parameters, we use the knowledge of the parameter κ_x to update the resulted force by canceling the displacement dependency from data. Then

$$F_n(\dot{x}, w)(t) = F_e(x, \dot{x}, w)(t) - \kappa_x(v)x(t). \tag{2.12}$$

As mentioned, this new function $F_n(\dot{x}, w)(t)$ will depend on the

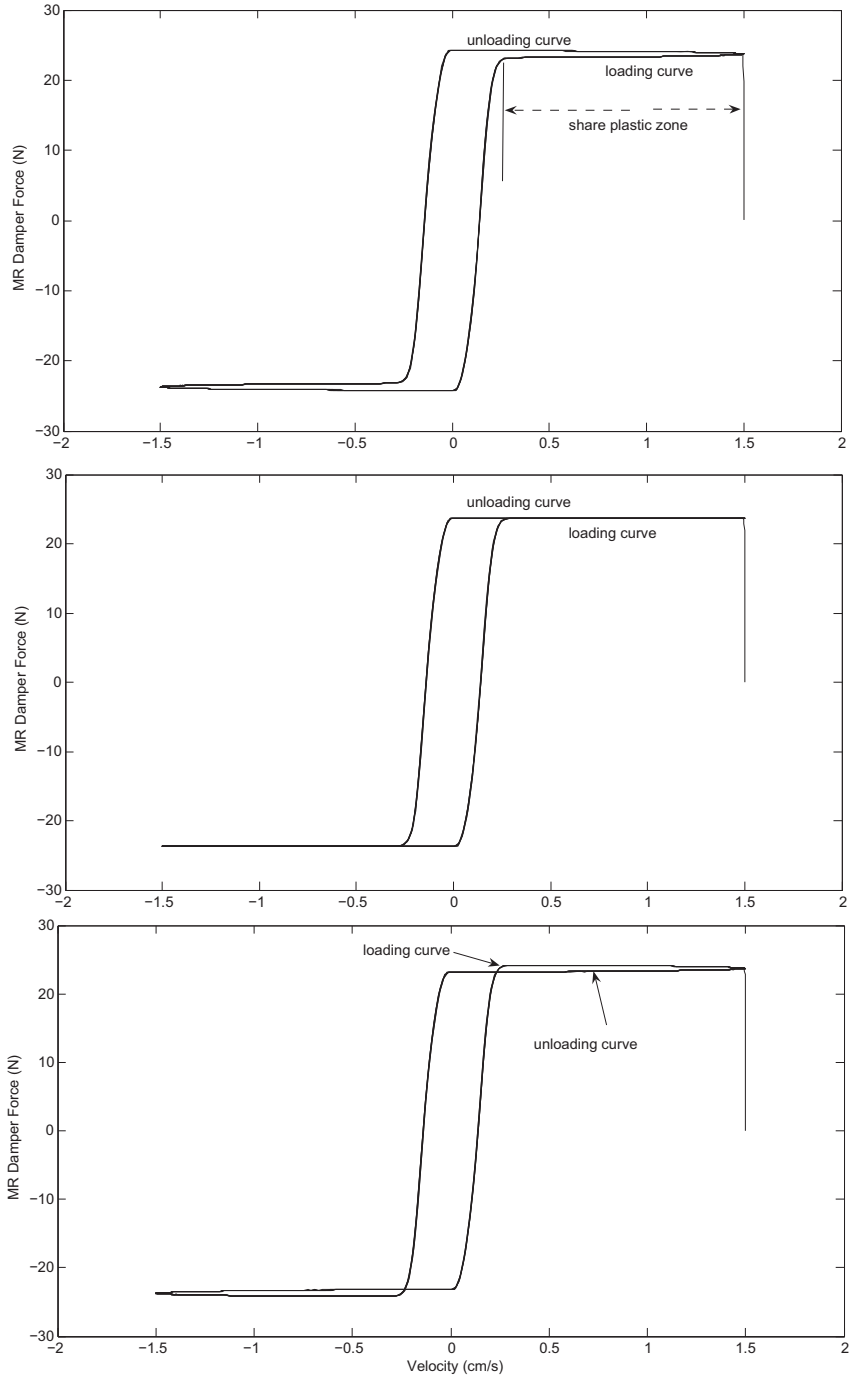

Figure 2.10: The effect of estimation of κ_x on the force-velocity plot. Up: under-estimation; middle: good estimation; Down: over-estimation.

velocity and the internal dynamic variable w. Therefore the F_n-displacement and F_n-velocity plots will have a general aspect like in Figure 2.11 (in solid line).

The rest of steps of the parameter identification method are basically similar to those in [93] and [94].

Therefore, the proposed parameter identification method can be summarized as follows:

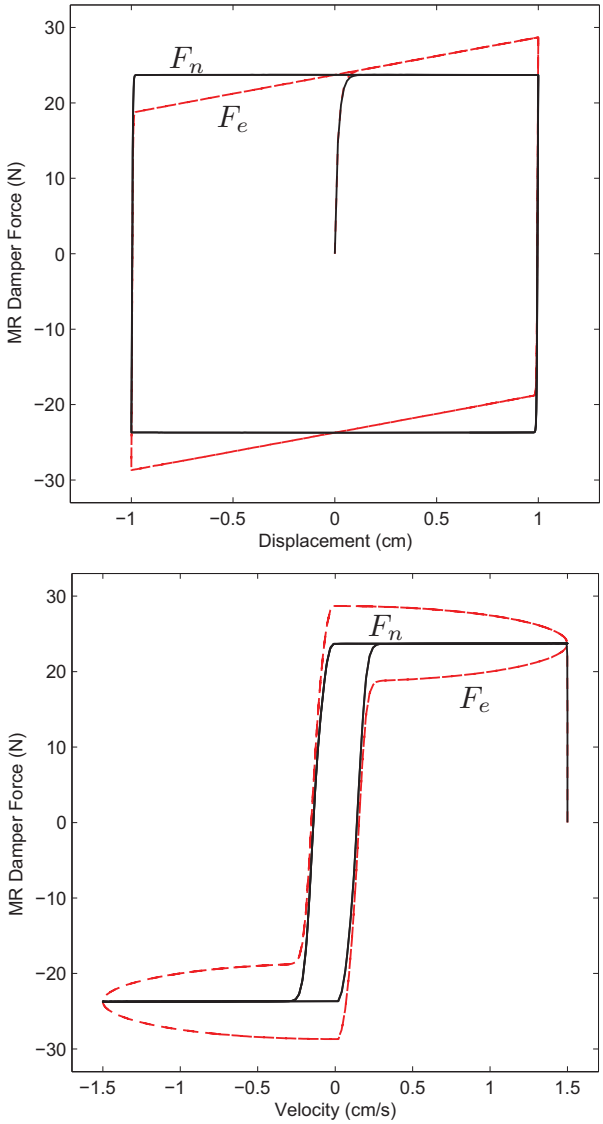

Figure 2.11: The results for the estimation of κ_x.

- Excite the MR damper with a sinusoidal displacement with amplitude large enough respect to its yielding displacement.
- Estimate the value of κ_x; this can be done graphically based on the force-displacement plot.
- Examine the estimated value of κ_x by studying the plastic branch status of the force-velocity plot.
- Construct the updated dynamic force F_n (2.12).
- Follow the rest of the method with the new constructed dynamic force F_n, based on [94], (Appendix A).

Next section is devoted to the numerical application of the method on a virtual MR damper as a sample device.

2.6 Application of the identification method

This section is concerned with the application of the proposed method on a virtual MR damper. More precisely, the proposed identification algorithm is tested using a black-box model of an MR damper, which is part of a smart base-isolated benchmark building problem [81] (Appendix B). This numerical platform has been used as a virtual laboratory test, where the inputs are the displacement x and the velocity $\dot{x}$ of the MR damper and the voltage v applied to modify the damper behavior (Figure 2.12). A first-order filter is necessary to model the dynamics involved in reaching rheological equilibrium and in driving the electromagnet in the MR damper [101, 80]. To validate the results, the output forces of the virtual device are compared with the output force of the model resulted from parameter identification, using seven predefined earthquake records of the benchmark problem as external excitation with their corresponding fluctuating voltage during full simulations.

Figure 2.13 shows the response of the virtual MR damper to a sinusoidal displacement with 0.5 m amplitude, under two extreme cases of command voltage, corresponding to zero and maximum voltage (in the benchmark MR model this value is 10 v [81]). As it is clear, the effect of the elastic term is apparent in the inclination of the cycle. Therefore the original normalized

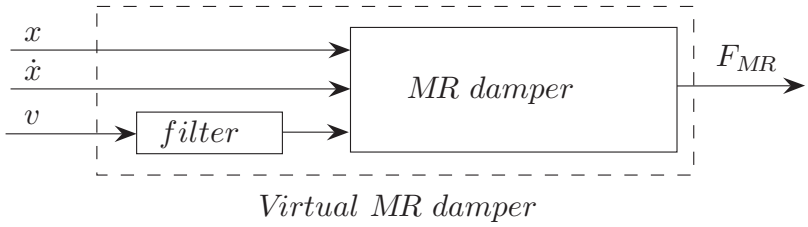

Figure 2.12: Input-output variables of the virtual MR damper.

Bouc-Wen model cannot catch the correct results for this MR damper. The new extended method will be applied. Additionally, the system parameters are also identified using the original identification method. In this way the comparison between the accuracy of the two methods will be possible.

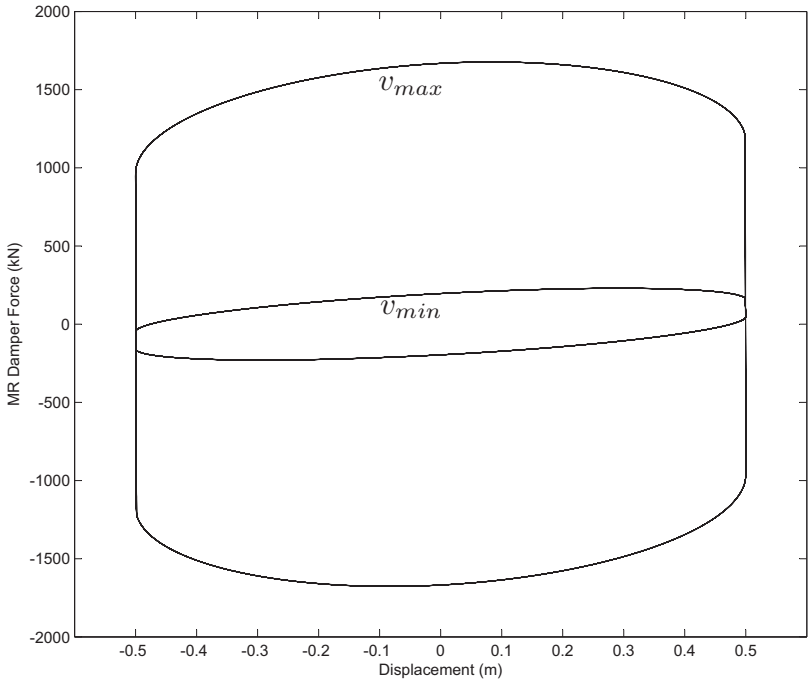

Figure 2.13: Force-displacement of the virtual MR damper.

2.6.1 Identification procedure

This section describes a numerical example for the proposed identification method of the MR damper introduced in previous section for a specific value of command voltage, which is assumed to be zero Volt. The same procedure will be applied for another value of command voltage.

When the black-box model of the MR damper in the smart base isolated benchmark building is driven with zero coil command voltage, the force-displacement diagram in Figure 2.14 is obtained. The estimated value for κ_x is then computed from the slop of the main diameter of the resulted ellipse as

$$\kappa_x = \frac{82.8}{0.4} = 207kN/m.$$

Calculating this value, the output force of MR damper can be updated by subtracting the whole elastic term from the resulted force (Eq. 2.12). To be sure about the accuracy of the

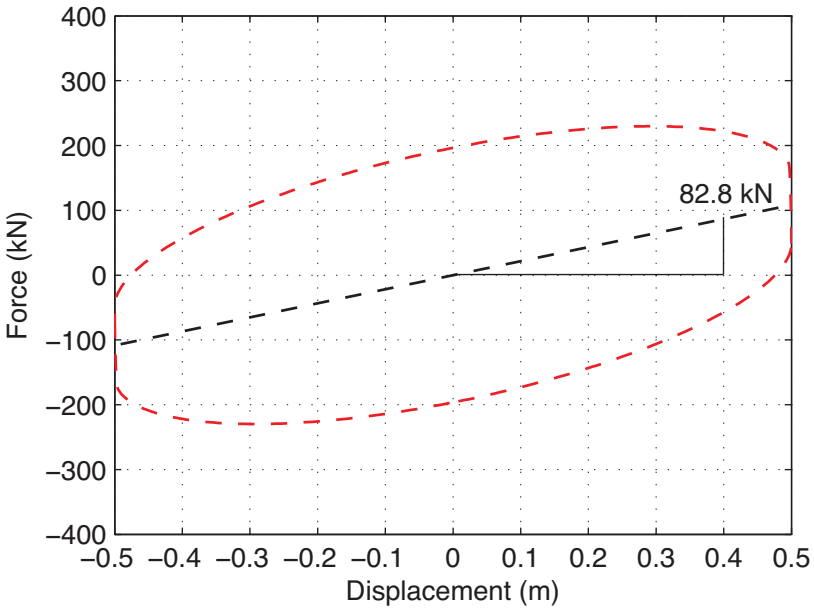

Figure 2.14: Computation of κ_x from the slop of the main diameter of the resulted diagram.

estimated value for κ_x, the updated force-velocity must be plotted. Figure 2.15 shows this graph. Since the plastic branch of the resulted plot becomes a line, the estimated value is acceptable.

From now on, the rest of the process will be applied on the updated value of the output force

$$F_n = F_e - \kappa_x(v)x(t) = \kappa_{\dot{x}}(v)\dot{x}(\tau) + \kappa_w(v)w(t) \tag{2.13}$$

In [46] it is shown that the hysteresis Bouc-Wen loop has a plastic region when the displacement is large enough. This region is characterized by $w \simeq 1$. Let's assume that there is a specific time interval within which the damper is in its plastic response

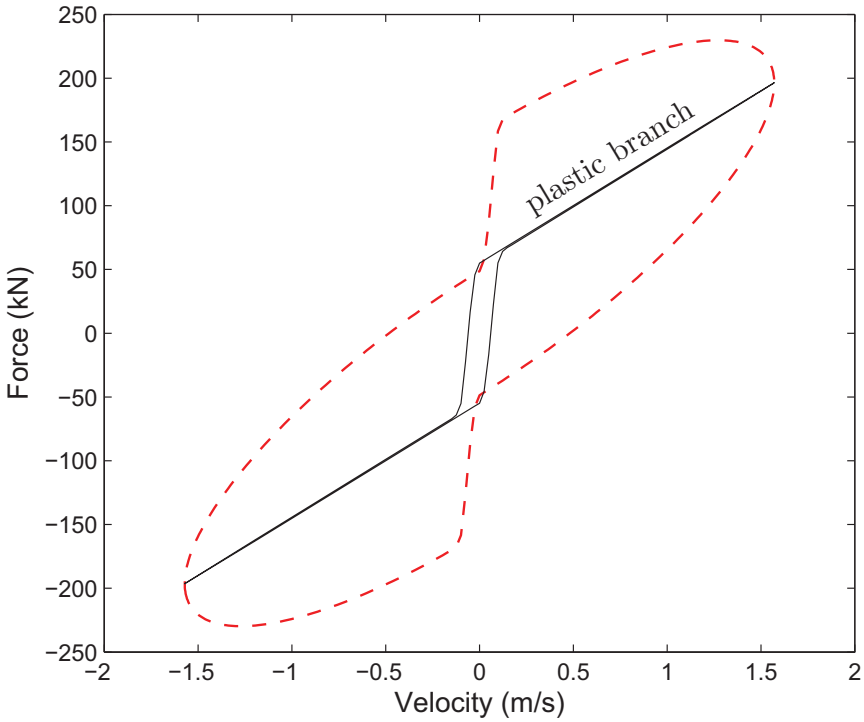

Figure 2.15: Force-velocity diagram for the resulting output force F_e (dashed) and the force $F_n = F_e - \kappa_x(v)x(t)$ (solid).

phase. Therefore, during this interval the equation (2.13) becomes

$$F_n(\tau) = F_e(\tau) - \kappa_x(v)x(\tau) = \kappa_{\dot{x}}(v)\dot{x}(\tau) + \kappa_w(v) \qquad (2.14)$$

This equation is linear in $\dot{x}$, so the parameters $\kappa_{\dot{x}}$ and κ_w can be determined by a linear regression of this part of the graph. This plastic linear branch is clearly observed in Figure 2.15. The whole identification method can be applied using the resulted data force from the black-box MR damper excited with sinusoidal displacement. But to retain the similarity of the process with the original method, and to prepare the possibility of comparing the results of the extended model (2.10) with the original one (2.1) in similar conditions, $\kappa_{\dot{x}}$ and the other parameters will be calculated based on the excitation of the black-box MR model with a predefined T-wave displacement as given in the Figure 2.16 in a similar manner as in the original procedure [48] .

Figure 2.16 illustrates the excitation displacement and the resulted force F_e for a zero voltage. Figure 2.17 shows the plots for the output force F_e (dashed) and the corresponding value for F_n (solid).

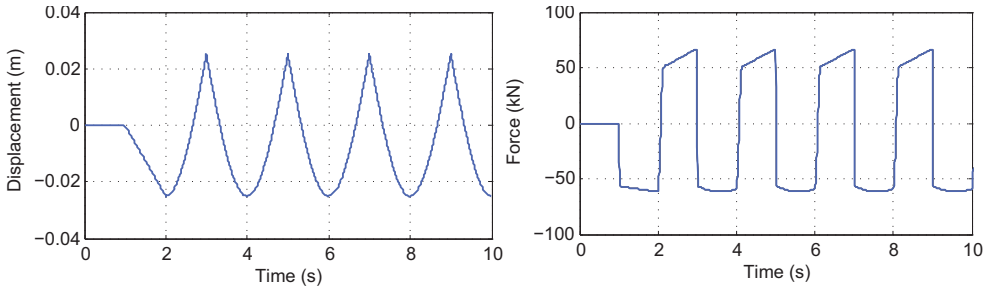

Figure 2.16: Response of the MR damper model in the benchmark building platform.

Updated by the equation (2.14), the loading stage of the updated force F_n versus velocity and the fitted line to identify the parameter $\kappa_{\dot{x}}$ are shown in Figure 2.18.

It is found the value of $\kappa_{\dot{x}} = 89.643$ kN.s/m and $\kappa_w = 54.652$

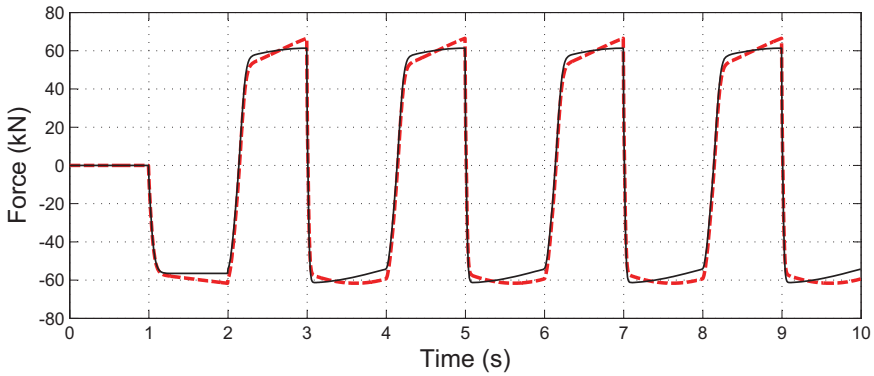

Figure 2.17: Time history for F_e (dashed) together with the updated function F_n (solid).

kN. To make the rest of the process more convenient an m-file has been written in MATLAB®. This m-file will read the updated force F_n and calculate the remaining parameters based on the procedure summarized in Appendix A. The next step is calculating the function θ which is an interface function for identifying the rest of parameters (Appendix A, (A.6)). Conceptually, it is similar to the function F_n. To calculate it, one has to subtract the viscous term from F_n function, then it will only depend on the hysteresis characteristics of the model. Therefore the function θ can be computed as

$$\theta(\tau) = F_n(\tau) - \kappa_{\dot{x}}\dot{x}(\tau) \quad \tau \in [0, T^+] \tag{2.15}$$

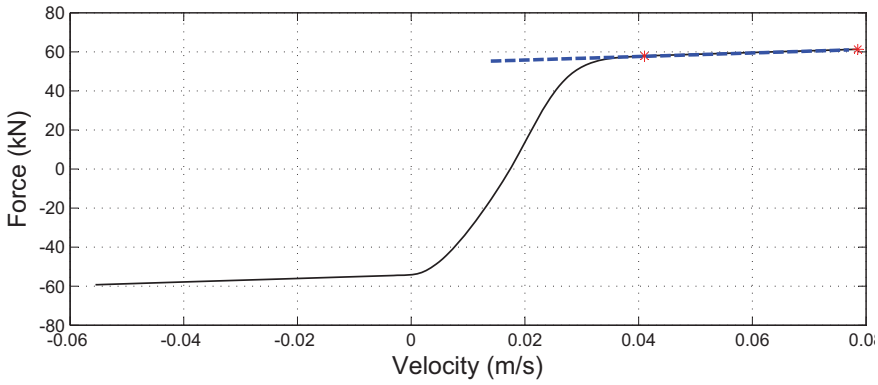

Figure 2.18: Loading stage of the F_e-velocity plot for calculating $\kappa_{\dot{x}}$.

where $[0, T^+]$ is the loading phase (Fig. 2.1). The corresponding zero point, x_* (Fig. 2.19, up), and the derivative at this point are defined as $x_* = -0.02465$ m and $a = 129607.56$ kN/m.

To determine the parameter n, two design parameters $x_{*2} > x_{*1} > x_*$ are to be chosen. Since n characterizes the sharpness of the transition from linear to plastic region ([48], p 110), the parameter $x_{*1} = -0.0245$ m $> x_*$ is chosen within the linear region while the parameter $x_{*2} = 0.0211$ m $> x_{*1}$ is chosen within the plastic region, close to the largest displacement value (Fig. 2.19, up). The derivative at those two points are computed, and the parameter $n = 1.4557$ is calculated using equation (A.8). The intermediate parameter $b = 386.566$ is computed using equation (A.9), which gives the parameter $\kappa_w = 54.652$ kN from equation (A.10). The parameter $\rho = 644.92$ m^{-1} is then computed (equation A.11) which allows the determination of the function $\bar{w}(x)$ using equation (A.12) (Figure 2.19, down). It is worth to note that this stage can be a good point to control the accuracy of

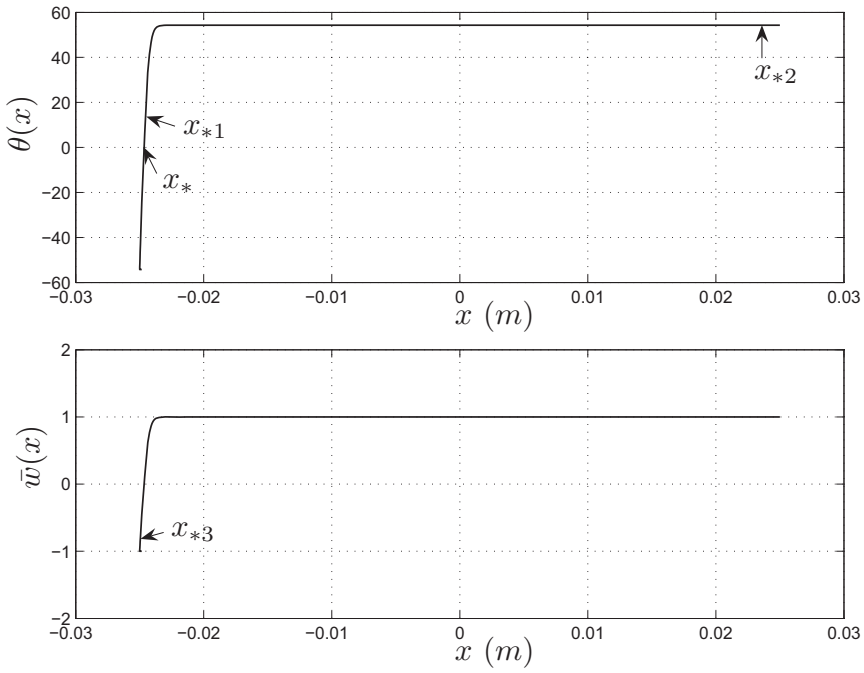

Figure 2.19: Up: $\theta(x)$ verses x. Down: $\bar{w}(x)$ verses x.

the parameters identified up to here. Indeed, the value of the variable $\bar{w}$ in normalized Bouc-Wen model is bounded by ± 1, and in the plastic region it has its maximum value (1 or -1). Figure 2.19, down, plots the resulted values of this variable in the plastic region. It can be observed that these conditions are satisfied, which is a checking of the accuracy.

The last parameter to determine is σ, which can be calculated using equation (A.13). To this end, the design parameter $x_{*3} = -0.024961$ m $< x_*$ is chosen close to the smallest value of the displacement. It is found that $\sigma = 0.773$. The whole steps of the identification procedure are listed in Table 2.2.

Table 2.2: Identification parameters for the extended normalized Bouc-Wen model.

Steps		Action	Results
1	•	Plot force-displacement for respond of MR damper to a sinusoidal excitation (figure 2.14)	$\kappa_x = 207$ kN/m
2	•	Linear regression (figure 2.18)	$\kappa_{\dot{x}} = 89.643$ kNs/m
3	◦	Equation (2.15) (figure 2.19, up)	θ
4	◦	The corresponding zero of θ	$x_* = -0.025$ m
5	◦	Equation (A.7)	$a = 129607.56$ kN/m
6	◦	Two design parameters x_{*1} and x_{*2}	$x_{*1} = -0.025$ m $> x_*$ $x_{*2} = 0.021$ m$> x_{*1}$
7	•	Equation (A.8)	$n = 1.456$
8	◦	Equation (A.9)	$b = 386.566$
9	•	Equation (A.10)	$\kappa_w = 54.652$ kN
10	•	Equation (A.11)	$\rho = 644.92$ m^{-1}
11	◦	Equation (A.12) (figure 2.19, down)	$\bar{w}(x)$
12	◦	Last design parameter	$x_{*3} = -0.025$ m $< x_*$
13	•	Equation (A.13)	$\sigma = 0.773$

2.6.2 Identification results

The identification procedure given in previous section has been applied for different voltages in the range $[0, 1]$ Volts. Table 2.3 gives the identified Bouc-Wen model parameters.

To find an accurate voltage-dependent relation for each of these parameters, first these data are plotted as discrete points, then an specific mathematical form is decided with parameters adjusted by a linear algebraic solver by means of MATLAB®.

Figure 2.20 plots these data for the parameter n. The overall form of variation seems close to an exponential function, which is written in the form

$$n(v) = a + b\ e^{(-cv)}$$

Table 2.3: Identification results

v	κ_x	$\kappa_{\dot{x}}$	κ_w	ρ	n	σ
0.00	207	89.643	54.652	644.92	1.4557	0.7733
0.05	207	104.24	125.97	647.34	1.4436	0.7674
0.10	207	118.84	214.49	648.11	1.4398	0.7656
0.15	207	133.44	313.47	648.45	1.4381	0.7648
0.20	207	148.04	416.96	648.64	1.4372	0.7643
0.25	207	162.64	519.87	648.75	1.4366	0.7641
0.30	207	177.24	617.94	648.82	1.4362	0.7639
0.35	207	191.84	707.73	648.87	1.4360	0.7638
0.40	207	206.44	786.63	648.90	1.4358	0.7637
0.45	207	221.04	852.86	648.92	1.4357	0.7636
0.50	207	235.64	905.48	648.94	1.4357	0.7636
0.55	207	205.25	944.37	648.95	1.4356	0.7636
0.60	207	264.84	970.24	648.96	1.4356	0.7636
0.65	207	279.44	984.64	648.96	1.4355	0.7636
0.70	207	294.04	989.94	648.96	1.4355	0.7636
0.75	207	308.64	989.34	648.96	1.4355	0.7636
0.80	207	323.24	986.89	648.96	1.4355	0.7636
0.85	207	337.84	987.43	648.96	1.4355	0.7636
0.90	207	352.44	996.67	648.96	1.4355	0.7638
0.95	207	367.04	1021.1	648.96	1.4355	0.7636
1.00	207	381.64	1068.2	648.98	1.4355	0.7635

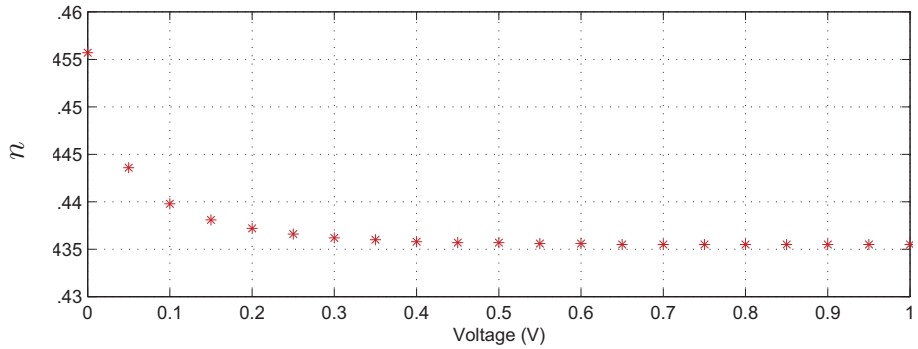

Figure 2.20: Identified values for parameter n versus voltage.

Figure 2.21 shows three functions obtained by fixing a priori three values of $c = 8, 13, 20$. Finally the middle function has chosen with corresponding coefficients.

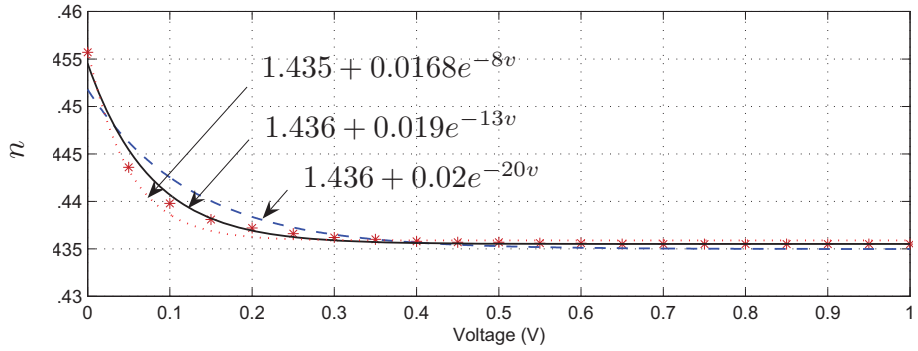

Figure 2.21: Three candidate functions for voltage dependency of parameter n.

The same procedure is repeated for the rest of the parameters and the corresponding voltage dependency function is found. Figure 2.22 shows all of the resulted functions. According with the functional dependence in these plots, it is considered that $\kappa_x(v)$ is constant, $\kappa_{\dot{x}}(v)$ is linear and $n(v)$, $\rho(v)$ and $\sigma(v)$

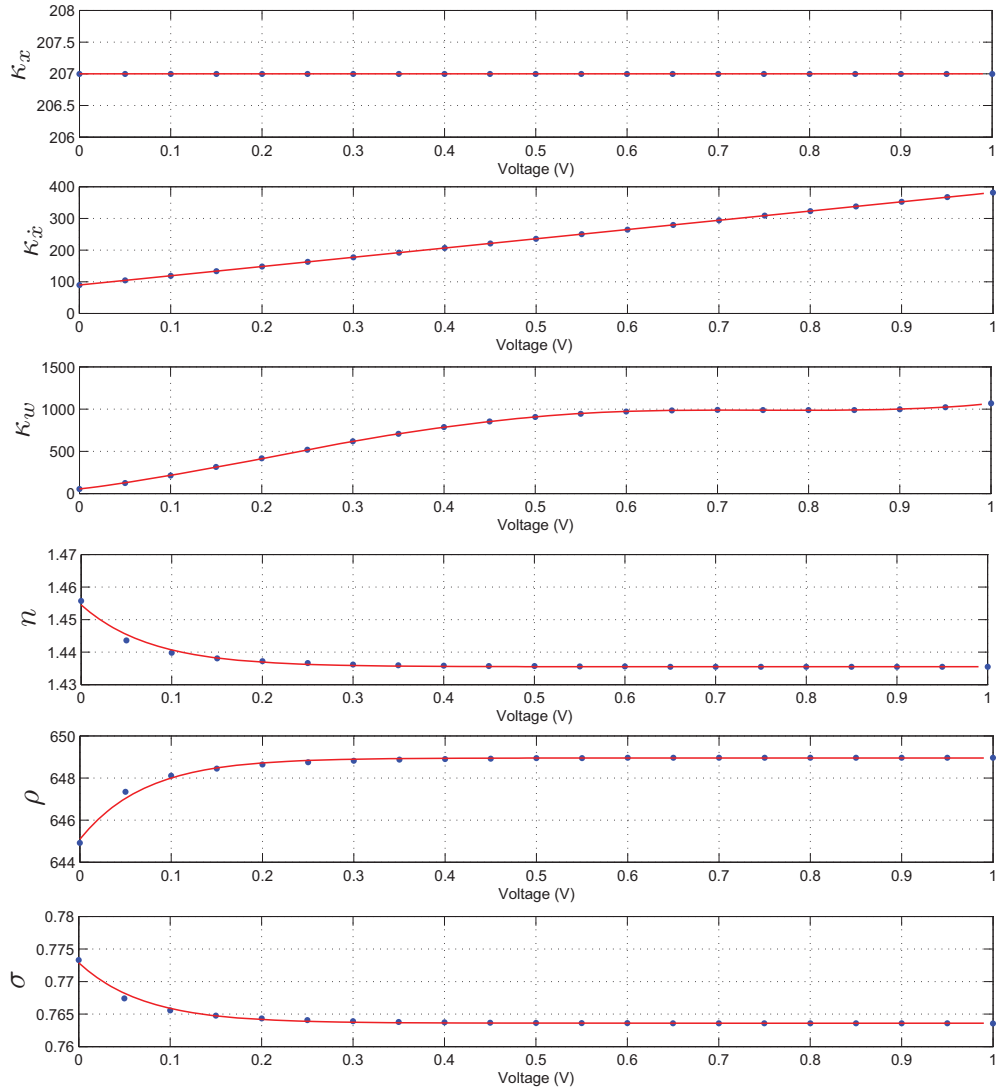

Figure 2.22: Results of the parameter identification algorithm.

are exponential:

$$\kappa_x(v) = \kappa_x \tag{2.16}$$
$$\kappa_{\dot{x}}(v) = \kappa_{\dot{x},a} + \kappa_{\dot{x},b} v \tag{2.17}$$
$$n(v) = n_a + n_b \exp(-13v) \tag{2.18}$$
$$\rho(v) = \rho_a + \rho_b \exp(-14v) \tag{2.19}$$
$$\sigma(v) = \sigma_a + \sigma_b \exp(-14v) \tag{2.20}$$

The parameter κ_w has a more complicated form, therefore it is difficult to find a unique suitable function for curve fitting. Because this parameter is very important due to its great influence in the resulted force (the range of its magnitude is, approximately, from 50 kN to 1000 kN, as can be seen in Table 2.3), its voltage dependence function is estimated in three different regions:

$$\kappa_w(v) = \begin{cases} \kappa_{w_1} + \kappa_{w_2} v^{1.15}, & v \leq 0.3 \\ \kappa_{w_3} + \kappa_{w_4} \sin(\frac{\pi(v-0.3)}{0.8}) & \\ \quad +\kappa_{w_5} \sin(\frac{3\pi(v-0.3)}{0.8}), & 0.3 \leq v \leq 0.7 \\ \kappa_{w_6} + \kappa_{w_7} v + \kappa_{w_8} v^3 & \\ \quad +\kappa_{w_9} v^5, & 0.7 \leq v \end{cases} , \qquad (2.21)$$

based on the variation of the resulted values (Figure 2.23). The coefficients κ_x, $\kappa_{\dot{x},a}$, $\kappa_{\dot{x},b}$, κ_{w1},...,κ_{w9}, n_a, n_b, ρ_a, ρ_b, σ_a and σ_b are presented in Table 2.4.

Therefore, the identification has been completed. In the next section this identified model will be validated under a very carefully chosen simulation.

2.6.3 Model validation

The identified models presented in the literature usually have good accuracy when they are validated under constant command voltage. However, because of the role of the MR dampers as semi-active devices in the structural control systems, the final identified model has to be checked under a simulated condition using, for instance, an earthquake record together with the corresponding fluctuating command voltage which will be consequence of the control process. To do this, the resulted identified model has to be compared with the main black-box model of MR damper in the benchmark building problem, under exactly the same simulation. To measure the discrepancy between two

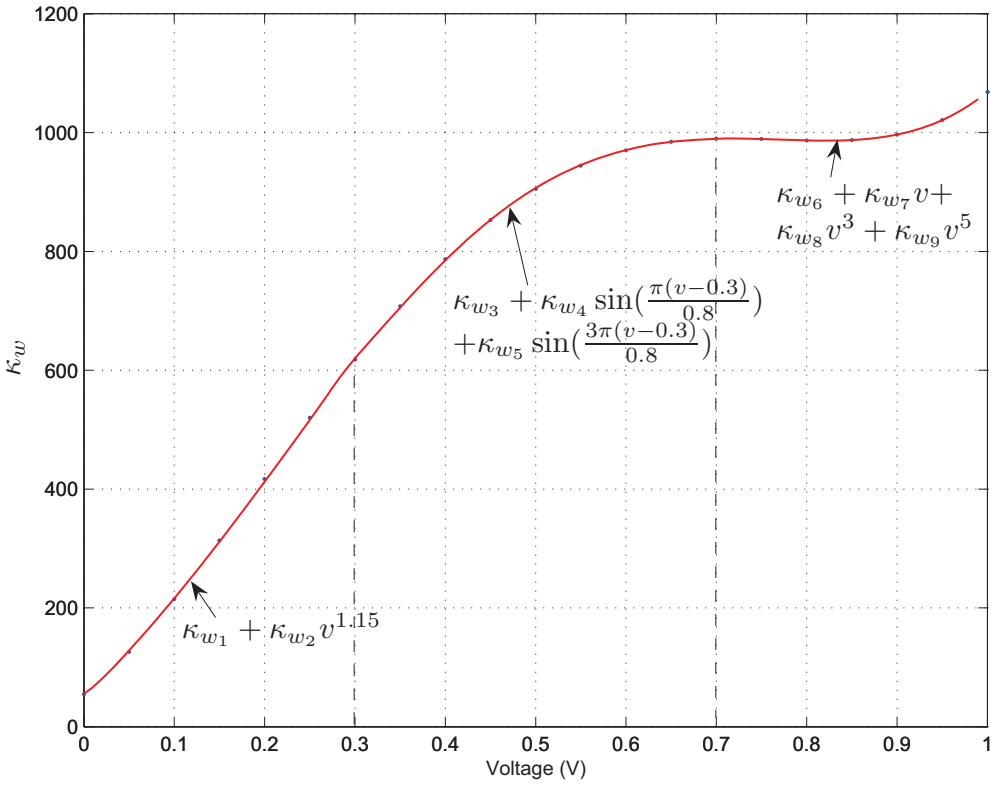

Figure 2.23: Results of the parameter identification algorithm for parameter κ_w.

models, the 1-norm error (ε) is used [93]:

$$\varepsilon = \frac{\|F_{BM} - F_{id}\|_1}{\|F_{BM}\|_1}, \tag{2.22}$$

$$\|f\|_1 = \int_0^{T_r} |f(t)| dt, \tag{2.23}$$

where F_{BM} is the output force of the black-box model (benchmark building platform) and F_{id} is the resulting force of the identified MR damper based on the model in equations (2.10)-(2.11). The length in time of each earthquake is denoted by T_r. The 1-norm is a measure that reflects the average size of a signal and thus it is a good tool for computing the discrepancy between these two models. Based on the resulted value of the

Table 2.4: Identification results

parameter		value
κ_x		207
$\kappa_{\dot{x}}$	$\kappa_{\dot{x},a}$	89.64
	$\kappa_{\dot{x},b}$	292
ρ	ρ_a	648.95
	ρ_b	-3.86
n	n_a	1.44
	n_b	0.02
σ	σ_a	0.76
	σ_b	0.009
κ_w	κ_{w1}	55.38
	κ_{w2}	2270.0
	κ_{w3}	619.85
	κ_{w4}	387.34
	κ_{w5}	18.42
	κ_{w6}	-87.52
	κ_{w7}	2665.0
	κ_{w8}	-3054.7
	κ_{w9}	1545.5

1-norm, if the computed value of the damping force is far from the reference value, the value of ε will be large. On the contrary, if it is small, the identified model can produce forces which are very close to the *real* ones. Table 2.5 presents the model errors for several earthquakes (FP-x and FP-y are the estimation errors in the x-force and y-force directions). A sample earthquake record and the corresponding command voltage during the control process are presented in Figure 2.24. In this application, the MR damper is used as a semi-active device in which the voltage is varying by a feedback control loop [50].

2.6.4 Comparison of results

It is interesting to compare the resulting model errors in Table 2.5 with the resulting model errors when the parameter identification is performed with the model in equations (2.1)-(2.2). The

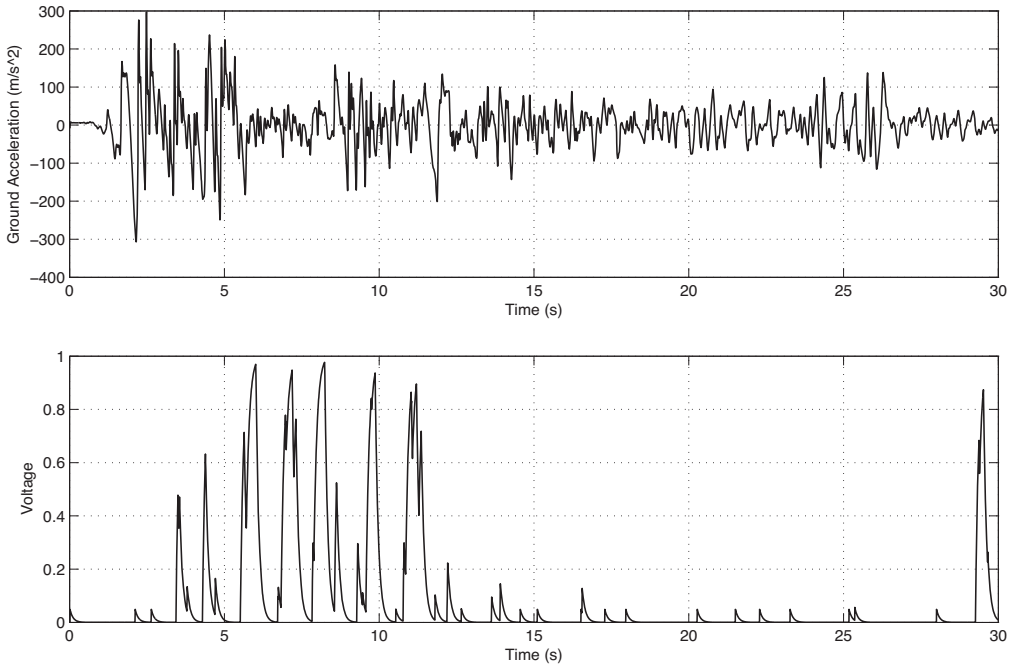

Figure 2.24: El Centro, ground acceleration (top) and corresponding control command voltage (bottom).

resulted voltage dependence functions for model parameters are

$$\kappa_{\dot{x}}(v) = 275.47 + 386.63v \tag{2.24}$$

$$\kappa_w(v) = \begin{cases} 43.374 + 1765.4v, & 0.0 \leq v \leq 0.5 \\ 824.921 + 202.277v, & 0.5 \leq v \leq 1.0 \end{cases}, \tag{2.25}$$

$$n(v) = 1.82 - 0.5\exp(-18v) \tag{2.26}$$

$$\rho(v) = 629.83 + 53.16\exp(-12v) \tag{2.27}$$

$$\sigma(v) = 0.933 - 0.14\exp(-8v) \tag{2.28}$$

Table 2.5: Error norm (ε) for the proposed parameter identification

	Newhall	Sylmar	El Centro	Rinaldi	Kobe	Jiji	Erzinkan
FP-x	6.47%	5.67%	7.78%	7.12%	6.52%	3.61%	4.88%
FP-y	3.84%	8.44%	7.90%	5.67%	7.85%	4.02%	5.35%

Table 2.6: Error norm (ε) for the method in [93]

	Newhall	Sylmar	El Centro	Rinaldi	Kobe	Jiji	Erzinkan
FP-x	16.15%	18.06%	22.89%	17.55%	18.22%	14.16%	14.91%
FP-y	15.83%	24.14%	19.68%	18.48%	24.72%	20.09%	18.80%

Table 2.6 shows the values of the errors for this case. By comparing these two tables, the proposed parameter identification algorithm is clearly more accurate than the method presented in [93, 94].

Figure 2.25 shows the comparison between the output force of the black-box MR damper during the simulation of the benchmark building under Kobe earthquake, with the two identified models, the proposed one and the model in [93, 94]. Since the two plots in Figure 2.25 (top) are very close, Figure 2.26 shows the corresponding errors in both cases. Figures 2.27 and 2.28 show the same comparison under Sylmar earthquake.

Figures 2.29 and 2.30 show three graphs; time history of the output force, force-displacement and force-velocity diagrams, for the identified model and the black-box one under El Centro and Rinaldi earthquakes, respectively.

These figures illustrate that the proposed identification method improve the results given in [93, 94].

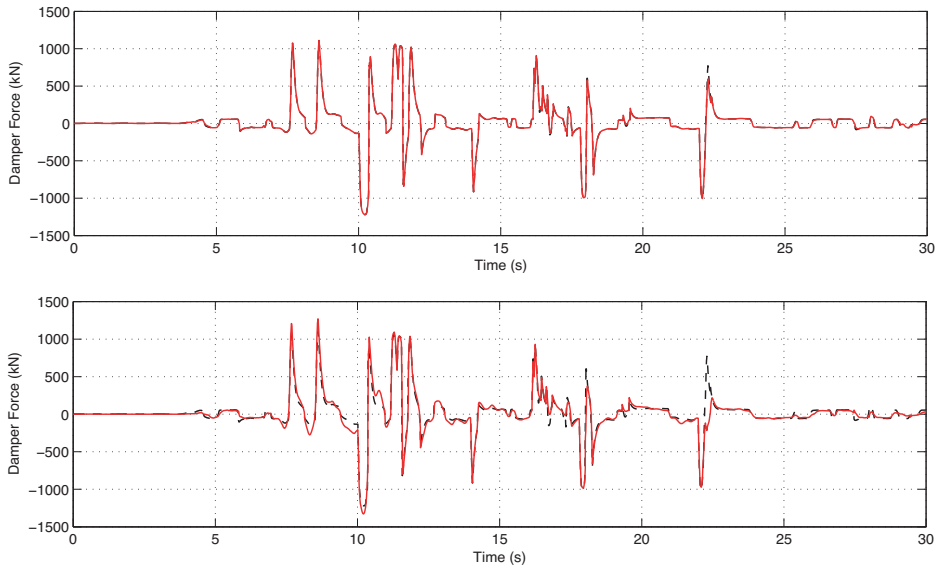

Figure 2.25: Comparison of the MR damper force for the proposed model (top/solid) and for the model in [93] (bottom/solid), both with the response of the original black-box model (dashed), under Kobe ground motion (FP-y).

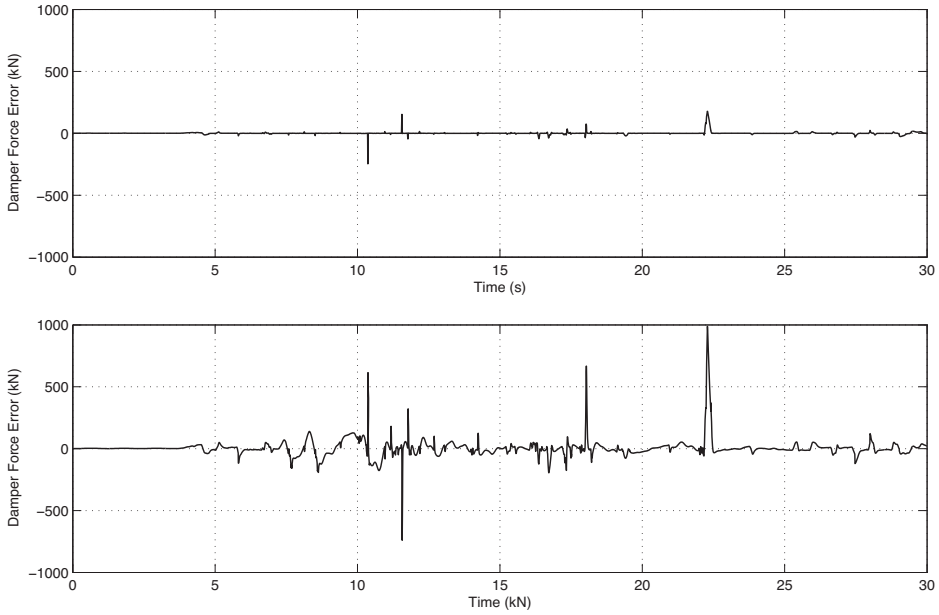

Figure 2.26: Generated damper force errors for proposed model (above), and the method in [93] (below) , under Kobe ground motion (FP-y).

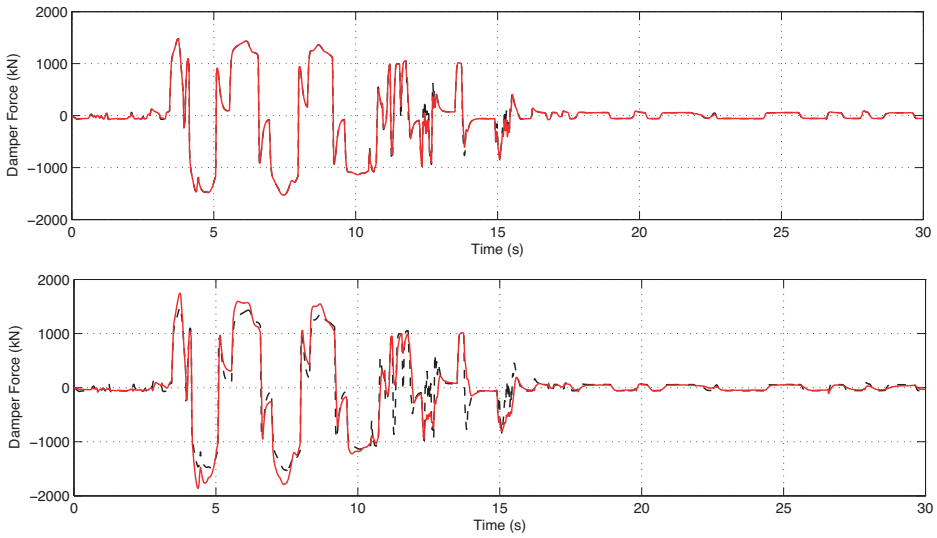

Figure 2.27: Comparison of the MR damper force for the proposed model (top/solid) and for the model in [93] (bottom/solid), both with the response of the original black-box model (dashed), under Sylmar ground motion (FP-y).

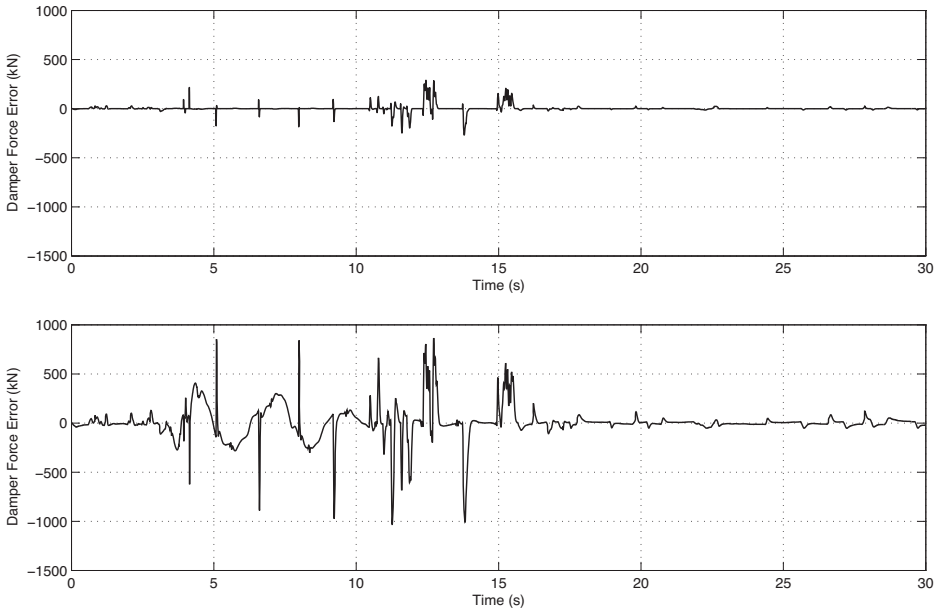

Figure 2.28: Generated damper force errors for proposed model (above), and the method in [93] (below), under Sylmar ground motion (FP-y).

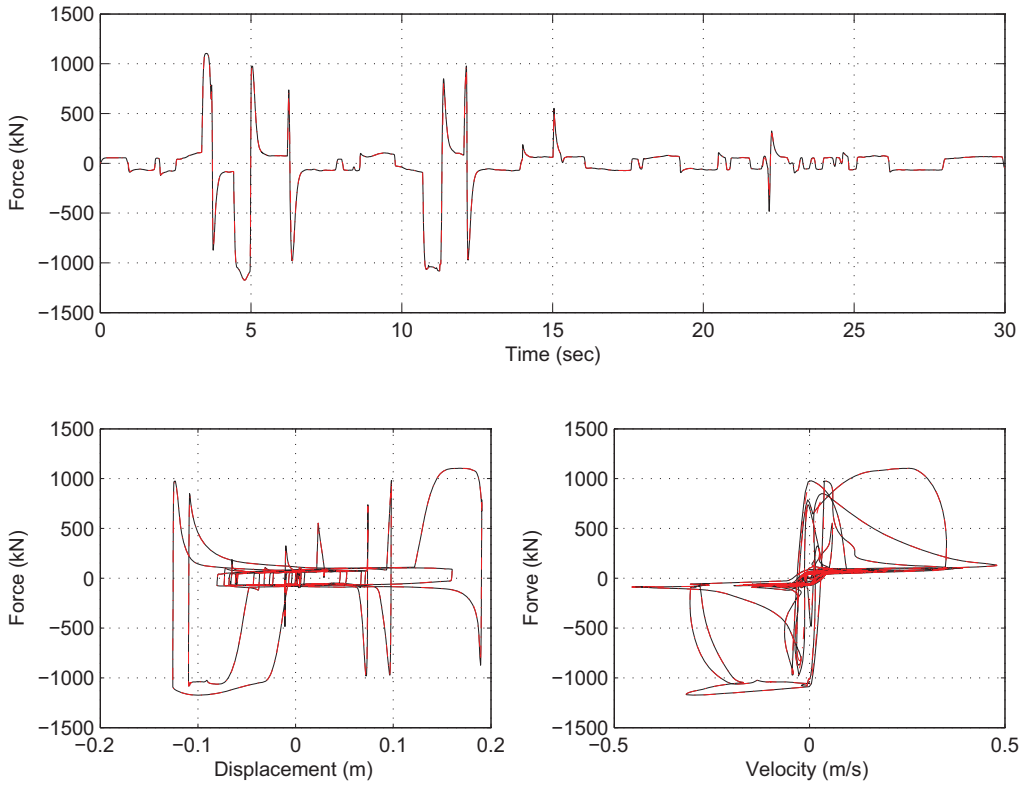

Figure 2.29: Compare the resulted plots for the original black-box model (solid) and identified one (dashed) under El Centro earthquake (FP-X).

2.7 Conclusion

This chapter has proposed an extension of a parameter identification method for MR dampers. This extension allows to identify a larger class of MR dampers more accurately. The validation of the parameter identification method has been carried out using a black-box model of an MR damper in a smart base-isolated benchmark building. The versatility of the parameter identification method has been tested using the MR damper as a semi-active device under time-varying voltage and earthquake excitation.

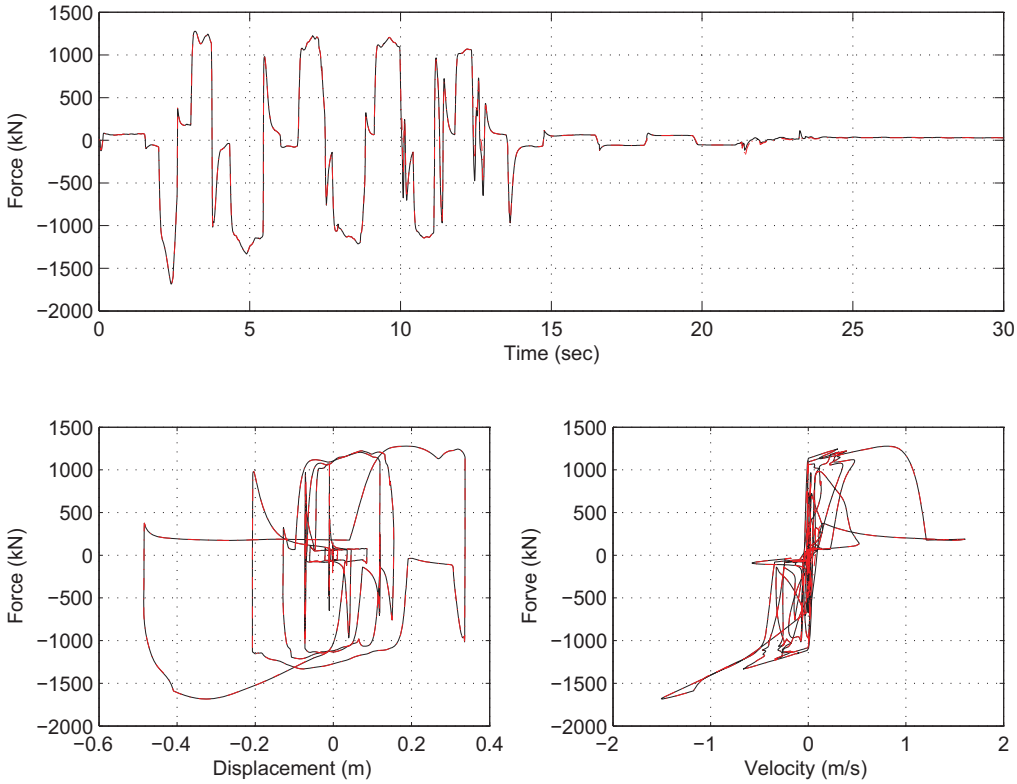

Figure 2.30: Compare the resulted plots for the original black-box model (solid) and identified one (dashed) under Rinaldi earthquake (FN-X).

Chapter 3

A new inverse model for MR dampers

3.1 Introduction

Most of the control strategies developed in the literature to be implemented by means of MR dampers are based on a two-stage process: (i) calculation of a desired active control force by a control algorithm; (ii) implementation of an actual force by means of the MR damper approaching the desired active force as better as possible.

Two main problems arise in this process: (i) the MR dampers are semi-active devices, being able to apply only dissipative control forces; (ii) they are intrinsically non-linear and their damping characteristics are changeable by external manipulation of a voltage (or a current).

In some recent papers [108, 17], it has been discussed on the benefits of developing inverse dynamic models to obtain the required input voltage for the MR dampers to produce forces as close as possible to the desired ones.

This chapter proposes a new inverse model for MR dampers based on the identified Bouc-Wen model developed in Chapter 2. This inverse model will be an essential part in the control strategy formulated in Chapter 4.

3.2 Literature review

Several approaches to determination of the input voltage of MR dampers have been proposed. Reference [17] successfully tackled this problem by employing a neural network (NN) emulation of inverse dynamics in the realization of the optimal control force. Recurrent NN models were constructed, based on a few previous time steps of displacement, damper force, voltage signal, and the optimal damper force. It was shown to be beneficial and essential to develop an inverse dynamics model to obtain the required input voltage or current for the MR damper to produce forces as close as possible to the optimal ones. Yet, it seems that generally this inverse dynamics model using a NN may be too complicated and difficult to implement. Reference [108] has developed a simplified approach, namely the simplified inverse dynamics (SID) model for both the Bingham plasticity model and the Bouc-Wen hysteresis model. Xia [**?**] presented an inverse model of the MR damper by using a multi-layer perception optimal neural network and system identification. Reference [16] presented an inverse dynamic model based on the Bouc-Wen hysteresis model.

3.3 A new inverse model for MR dampers

The inverse model will provide a suitable tool to compute the command voltage of MR dampers analytically. Consider again the extended normalized form of the Bouc-Wen model for MR dampers (2.10):

$$F_e(x, \dot{x}, w)(t) = \kappa_x(v)x(t) + \kappa_{\dot{x}}(v)\dot{x}(t) + \kappa_w(v)w(t) \qquad (3.1)$$

where $F_e(x, \dot{x}, w)(t)$ is the output force of the MR damper. It has been obtained in Section 2.6.2 that κ_x is constant, $\kappa_{\dot{x}}(v) = \kappa_{\dot{x},a} + \kappa_{\dot{x},b}v$ is linear and $\kappa_w(v)$ is a piecewise nonlinear function defined in equation (2.21). The inverse model (see Figure 3.1), that is, the computation of the voltage v as a function of the displacement, velocity and force, is based on two simplifications:

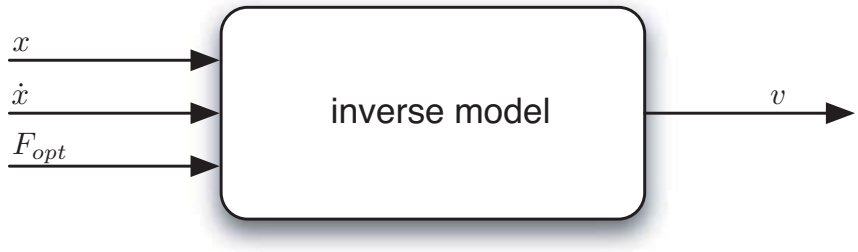

Figure 3.1: Input-output variables of the inverse model.

(a) on one hand, the piecewise nonlinear function κ_w is replaced by a piecewise linear representation as illustrated in Figure 3.2:

$$\kappa_w(v) = \kappa_{w,a} + \kappa_{w,b} v,$$

where $\kappa_{w,a}$ and $\kappa_{w,b}$ are defined in Table 3.1;

(b) on the other hand, the internal dynamic variable $w(t)$ is nonlinear and unmeasurable variable. Calculation of its

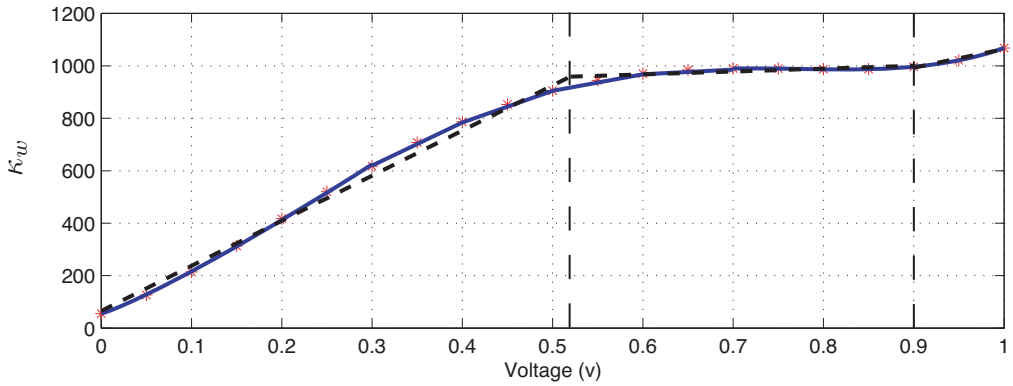

Figure 3.2: The piecewise nonlinear function k_w (solid) is approximated by a piecewise linear representation (dashed).

Table 3.1: Parameters value of the inverse model.

parameter			value
κ_x			207
$\kappa_{\dot{x}}$	$\kappa_{\dot{x},a}$		89.64
	$\kappa_{\dot{x},b}$		292.0
κ_w	$\kappa_{w,a}$	$0.0 \leq v^a \leq 0.52$	65.20
		$0.52 \leq v \leq 0.9$	902.1
		$0.9 \leq v \leq 1.0$	349.1
	$\kappa_{w,b}$	$0.0 \leq v \leq 0.52$	1720.8
		$0.52 \leq v \leq 0.9$	109.10
		$0.9 \leq v \leq 1.0$	715.30

[a]Command voltage of the MR damper

value is difficult and time consuming in a realtime operation, so it should be better replaced by a suitable function. In order to find this suitable function, one has to observe the response of the MR damper device during a moderate vibration. Figure 3.3 shows the force-velocity cycle of the black-box MR damper included in the benchmark structure, when excited under a sinusoidal displacement with one meter amplitude.

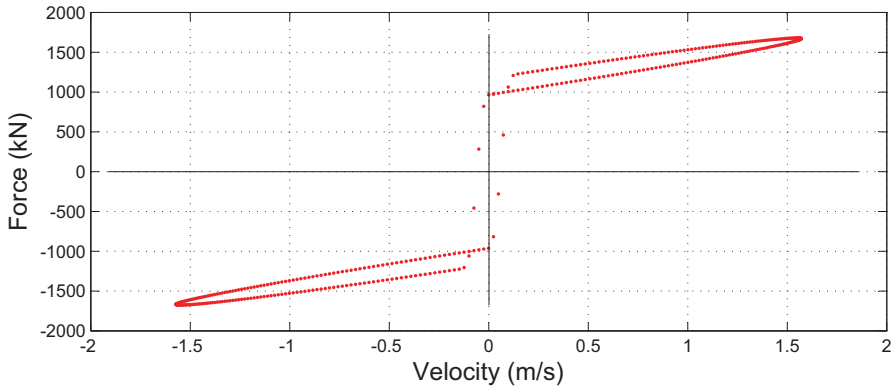

Figure 3.3: Response of the black-box MR model under sinusoidal displacement.

Assume that the force is represented by the Bouc-Wen

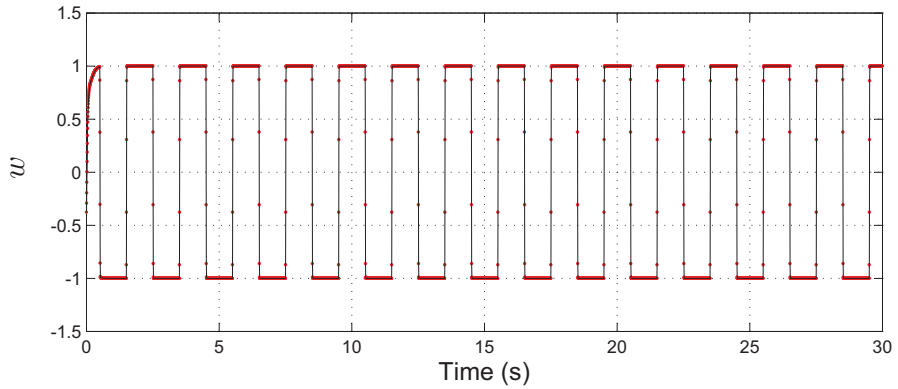

Figure 3.4: Internal dynamic time history.

model (Eq. 3.1), the corresponding dynamic variable $w(t)$ can be obtained from (3.1) using the information of the displacement x and the velocity $\dot{x}$. Figure 3.4 shows this result, which is plotted as a time history graph. It can be observed that most of the time the dynamic variable $w(t)$ has one of its extreme values ± 1. When $w(t)$ is plotted versus the excitation velocity $\dot{x}$, the observation leads to an important advantage (Figure 3.5). Indeed, this figure suggests to replace the hysteretic internal variable $w(t)$ with a signum function of $\dot{x}$:

$$w(t) = \mathrm{sgn}(\dot{x}) \in \{-1, 1\}. \tag{3.2}$$

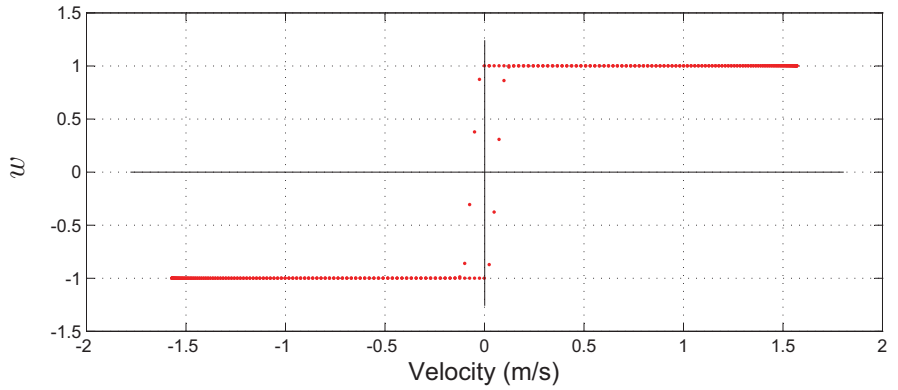

Figure 3.5: Internal dynamic parameter versus velocity.

This simplification will affect the accuracy of the model, but at the same time has a great advantage on simplifying the inverse model. The precision of this simplification is illustrated in Figure 3.6 in which the signum function in (3.2) is plotted together with the variable $w(t)$ of Figure 3.5.

We remark that, in the normalized version of the Bouc-Wen model, the value of this internal dynamic variable lies within the range $[-1, 1]$.

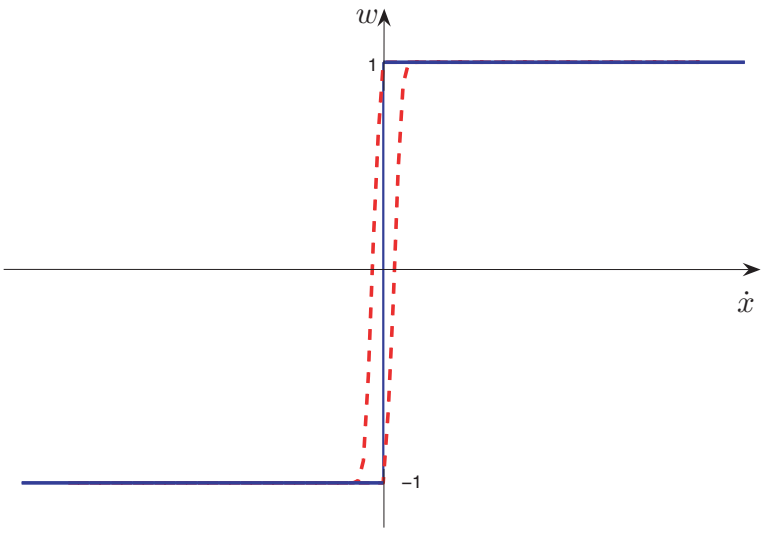

Figure 3.6: The internal dynamic variable $w(t)$ is approximated by the sign of the velocity.

As a result of this simplification, the MR damper model is

$$\begin{aligned} F_I(x,\dot{x})(t) &= \kappa_x x(t) + (\kappa_{\dot{x},a} + \kappa_{\dot{x},b} v)\dot{x}(t) \\ &\quad + (\kappa_{w,a} + \kappa_{w,b} v)\ \mathrm{sgn}(\dot{x}), \\ &= \kappa_x x(t) + \kappa_{\dot{x},a}\dot{x}(t) + \kappa_{w,a}\ \mathrm{sgn}(\dot{x}) \\ &\quad + (\kappa_{\dot{x},b}\dot{x}(t) + \kappa_{w,b}\ \mathrm{sgn}(\dot{x}))\ v. \end{aligned} \tag{3.3}$$

Thereby, the final form of the inverse model will be:

$$v(x, \dot{x}, F) = \frac{F_I - \kappa_x x(t) - \kappa_{\dot{x},a}\dot{x}(t) - \kappa_{w,a}\ \mathrm{sgn}(\dot{x}(t))}{\kappa_{\dot{x},b}\dot{x}(t) + \kappa_{w,b}\ \mathrm{sgn}(\dot{x}(t))}. \quad (3.4)$$

3.4 Additional constraints

In order to apply the inverse model of MR damper as a part of the control strategy, two constraints must be taken into account; The passivity and limitation constraints [108].

3.4.1 Passivity constraint

In active control, forces can be produced in any of the four quadrants in the force-velocity graph, while semiactive devices can only produce forces in the first and third quadrants (Figure 3.7) at which the forces are dissipative. If we call F_{opt} the optimal force value obtained using any chosen active control law, the ideal force $F(t)$ able to be implemented by a semiactive device is then written in the form

$$F(t) = \begin{cases} F_{opt}(t); & F_{opt}.\dot{x}(t) \geq 0 \\ 0; & F_{opt}.\dot{x}(t) \leq 0 \end{cases}, \quad (3.5)$$

where $\dot{x}(t)$ is the piston velocity.

As the actual damper resisting force $F_{actual}(t)$ will have the same sign as the piston velocity $\dot{x}(t)$ at time t [108], the obtained control force $F_{opt}(t)$ can be compared with $F_{actual}(t)$. Hence, $F_{opt}(t)$ is physically realizable only if they have the same sign, that is

$$sgn(F_{opt}(t)) = sgn(F_{actual}(t)). \quad (3.6)$$

For the actual MR dampers responses, this condition is observed during most of the operating time. Figure 3.8 shows the response of the black-box MR damper in the benchmark structure under a sinusoidal displacement with the 5 Volts command voltages.

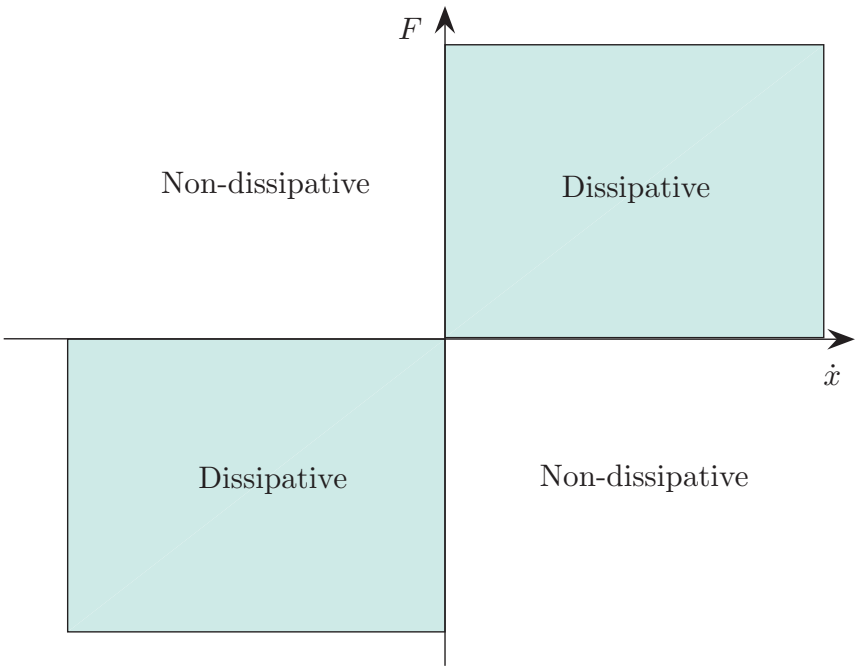

Figure 3.7: Semi-active MR damper dissipative quadrants.

3.4.2 Limitation constraint

In addition to the passivity constraint, since the force generated in the MR dampers depends on the local responses of the structural system, there are upper and lower limits on the force that the MR damper can produce, which are dependent on the motion of its piston, i.e.

$$|F_{min}(t)| \leq |F_{opt}(t)| \leq |F_{max}(t)|. \tag{3.7}$$

$|F_{min}(t)|$ and $|F_{max}(t)|$ are, respectively, the magnitudes of the maximum and minimum damper forces that can be achieved at time t. On the basis of the two constraints above, if $F_{opt}(t)$ is realizable with the MR damper, implying that it satisfies both

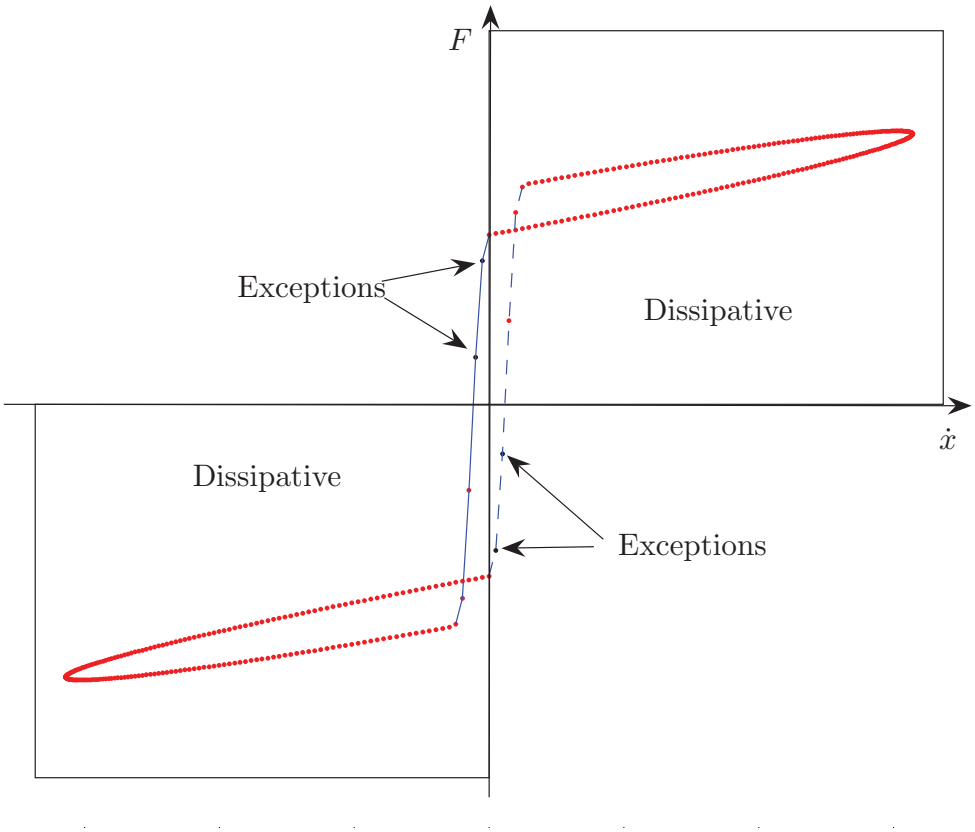

Figure 3.8: The MR dampers force and velocity, in most of the operating time, have the same sign.

(3.5)-(3.7), then theoretically, any inverse model may be employed to obtain the optimal input current or voltage and produce the desirable damper force. Otherwise, the input voltage or current should be set at either zero or the maximum achievable level.

Based on the equation (3.3) and the minimum and maximum values of the command voltage, two surfaces correspond to the minimum and maximum available force in x-$\dot{x}$-F space can be found (Figure 3.9). Any intermediate voltage would produce another surface inside the volume bounded by these two extrema. This volume represents the range of forces realizable

by the MR damper with different voltage inputs. Another realizable region also exists in the third quadrant and is antisymmetrical to the one in the first quadrant.

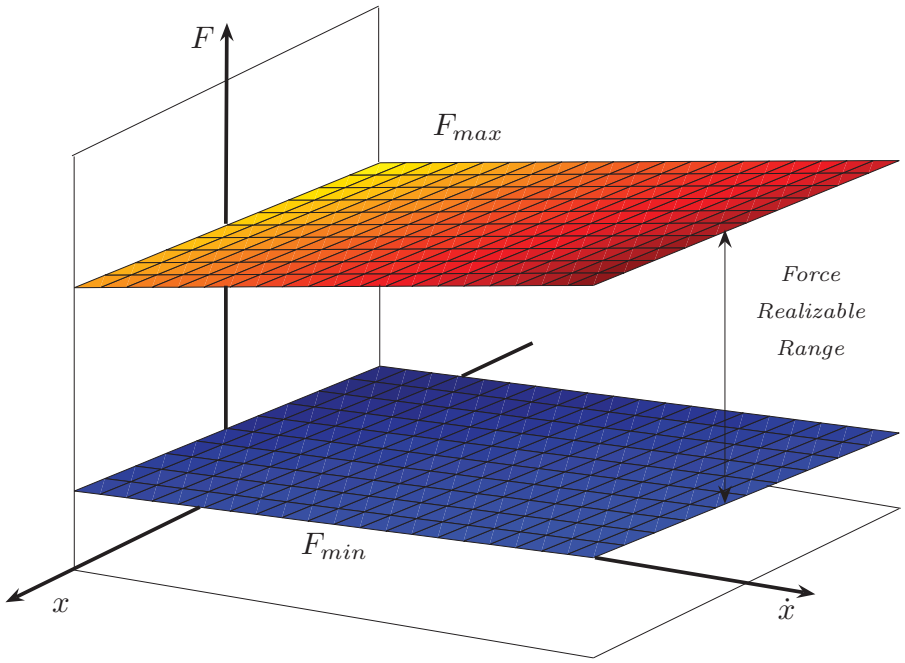

Figure 3.9: Representation of the realizable force for block-box MR damper.

The rule of the constraints is quite straightforward. For a given displacement and the corresponding velocity, the voltage is set at the maximum when the desirable control force F_{opt} is larger than F_{max}, and set at the minimum when F_{opt} is smaller than F_{min}. If the desirable control force falls inside the realizable region (Figure 3.9), then the force together with the building response at the MR dampers' location are passed into the inverse model (3.4) to calculate the required command voltage.

3.5 Conclusion

This chapter has proposed a new inverse model for MR dampers. This model has been obtained based on two simplifications. First the piecewise nonlinear function κ_w is replaced by a piecewise linear representation, and then the internal dynamic variable $w(t)$ of the Bouc-Wen hysteretic model has been replaced by the Coulomb friction model. The final form of the inverse model has been presented by Equation (3.4). If the two additional constrains are satisfied, then the voltage of the MR dampers can be manipulated by the inverse model. Next chapter will deal with this concept.

Chapter 4

Hierarchical semi-active control of base-isolated structures

4.1 Introduction

Base isolation is one of the most well accepted methods to protect moderate high and weight structures from earthquake hazard because of its simplicity, reliability, and effectiveness [98, 100]. This system by itself can reduce the interstory drift and the absolute acceleration of the structure, but the absolute base displacement of the structure may be large and hard to accommodate. Passive high-damping devices incorporated within the isolation system can control large bearing displacements associated with pulse-like earthquake ground motions, but the beneficial effects of the base isolation system may be significantly reduced for both moderate and strong earthquakes due to the transfer of energy into higher modes which can result in increased interstory drift and floor acceleration responses [57, 79, 91]. Semi-active controllers in hybrid base-isolation systems can achieve almost the same performance as an active base isolation system in protecting the safety of buildings against

strong earthquakes [65]. Therefore, a hybrid base isolation system with semi-active devices, like MR dampers, in parallel to isolation bearings, can significantly overcome this problem by means of the application of a single force at the base [49, 91].

This Chapter deals with a new hierarchical semi-active control strategy. A hybrid seismic control system for building structures is chosen, which combines a set of passive base isolators with a semi-active control system. Because the force generated in the MR dampers is dependent on the local responses of the structural system, the *desired* control force cannot always be produced by the devices. Only the control voltage can be directly controlled to increase or decrease the force produced by the devices. The desired control force is based on an active controller presented in [90] which has shown sufficient compatibility with the inherent characteristics of MR dampers. In general, in the semi-active control strategies presented in the literature, for instance [50, 53, 22, 116, 127], they managed a single MR damper per floor or, in the case of multiple MR dampers, they receive the same command voltage. In this work, a new practical method has also been defined to compute the command voltage of each MR damper independently according to the desired control force. The management of these MR dampers is based on a hierarchical strategy: it first compare the total damping force generated in the MR dampers with respect to the desired control force and then it decide what dampers need to apply more damping force and the corresponding command voltage. In this study only linear bearing isolation systems is under consideration, but because of the inherent character of the chosen controller, the types of isolation systems are not a limitation. Application to the other non-linear isolation systems are straightforward.

4.2 Literature review

Since base isolation systems often exhibit nonlinear behavior, and MR dampers are highly nonlinear devices, developing control algorithms to fully take advantage of their characteristics

has been challenging. Several control strategies have been proposed for use with these devices and, as shown in [54], they can be categorized as model-based control, that is, algorithms that require an accurate mathematical model of the system, and intelligent control.

4.2.1 Model-based control

Optimal-control based algorithms

References [27, 28] proposed an algorithm for control of MR damper based on the acceleration feedback. This strategy consists of a bang-bang type of controller that causes the damper to generate a desirable control force which is determined by a linear quadratic (LQ) optimal controller, combined with a force feedback loop. This method was experimentally verified [28, 29]. The algorithm then extended to the multiple MR damper case [26] and [123] verified experimentally the effectiveness of it for the case of multiple MR dampers. Johnson et al. [51] performed a feasibility study on the applicability of semiactive control using the clipped-optimal control algorithm and an MR damper to a base isolated building system, and [91] considered a base isolation system in which a lead rubber bearing (LRB) was used in parallel with an MR damper. Experimental verification of the effectiveness of a hybrid base-isolated building along with semiactive MR device has been studied in [124]. A modified version of clipped-optimal control used by [123]. In the modified version of the control algorithm, the control voltage can be any value between zero and V_{max} . Another modification is done by applying a threshold to the control voltage for the MR damper to make the controller more robust for the ambient vibration [124]. A third modification on the clipped-optimal control presented in [53]. In this case when the control voltage is nonzero the value of it will be calculated based on the same linear relation unless the force of MR damper be very smaller than the value of desired control force, then, the maximum possible voltage will be chosen (V_{max}).

Two optimal displacement control strategies were proposed by [115] for control of MR and ER devices. The first control strategy is referred to as clipped-optimal displacement control. Unlike the clipped optimal force control algorithm, which determines the desired optimal force and varies the voltage to trace such force, this algorithm attempts to trace the optimal damper displacement, which is calculated using a linear quadratic regulator (LQR). Since the damper displacement cannot be directly controlled, the damper force is varied so that this desirable displacement is achieved.

The second control algorithm was named optimal displacement control. It also attempts to trace a desirable displacement by applying some modification on the first method.

Lyapunov function-based control

Lyapunov function-based algorithms, such as control based on Lyapunov stability theory, decentralized bang-bang control and maximum energy dissipation, have quite effective performance in reducing seismic response. The first step consisted in selecting a Lyapunov function which must be a positive function of the system's states. Control inputs were then chosen to make the derivative of the function negative and large in magnitude [75]. Ha et al. [40] presented a Lyapunov-based control strategy with the objective to minimize an internal energy function. The feasibility of using MR damper for motion control of a two-degree-of-freedom system is studied by [113] by means of a quadratic Lyapunov function, which has been chosen as a function of the relative position and velocity of two masses. This strategy was also used in [53, 35, 74, 20, 82, 83].

4.2.2 Intelligent control

Although model-based control strategies have been successful in reducing structural vibrations, all models developed are based on assumptions and uncertainties. One must therefore make

sure that these model-based controllers are robust enough to control the real life structures [103]. Intelligent technology-based control has therefore been suggested as an alternative to strategies that rely on system model. Three main categories of intelligent control algorithms have been proposed for use with the MR dampers: neural network-based control, neuro-fuzzy-based control, and fuzzy logic-based control. Pioneering studies by [36, 19] showed that neural networks can be applied successfully to the control of large civil structures. The vibration of nonlinear structures showing hysteretic behavior was also controlled via nonlinearly trained neural networks [7, 126].

An improved semi-active neural network-based controller in conjunction with MR dampers is employed in vibration reduction of a base-isolation benchmark structure [62]. The key problem of controlling the strong nonlinear structures with MR dampers successfully is to choose current or voltage input in MR damper quickly and precisely [117]. Fuzzy control technique is considered as a tool to solve this problem. An adaptive fuzzy strategy for the control of a structure installed with a magnetorheological (MR) damper has been proposed in [66]. The fuzzy rules are usually defined according to personal experiences, without proving the rules they adopt are the better ones.

4.3 Hierarchical semi-active control algorithm development

Each of the proposed controllers is able to reduce the structural response to some degree. From a structural point of view, a reasonable controller has to reduce the base displacement while decreases or slightly increases the accelerations. Li and Ou [65] showed that the active control forces in base-isolated structures have damping characteristics. In addition, an active robust control for nonlinear base-isolated structures which has a damping characteristic and is in line with the results of [65] was proposed in [90].

In this study, this class of active controller will be applied

in a semi-active way to the base-isolated benchmark building [81]. The control forces will be applied at the base through manipulation of the command voltage at the MR dampers.

4.3.1 The desired control force

For control design, a nonlinear base-isolated building structure as shown in Figure 4.1 is considered. More precisely, a dynamic model composed of two coupled subsystems, namely, the main structure or superstructure (Sr) and the base isolation (Sc), is employed:

$$S_r : \boldsymbol{M}\ddot{\mathbf{x}} + \boldsymbol{C}\dot{\mathbf{x}} + \boldsymbol{K}\mathbf{x} = -\boldsymbol{M}\mathbf{J}\ddot{\mathbf{x}}_g + \mathbf{F}_c + \mathbf{F}_k \tag{4.1}$$

$$S_c : m_0\ddot{x}_0 + c_0\dot{x}_0 + k_0 x_0 = c_1\dot{r}_1 + k_1 r_1 - m_0\ddot{x}_g - \phi, \tag{4.2}$$

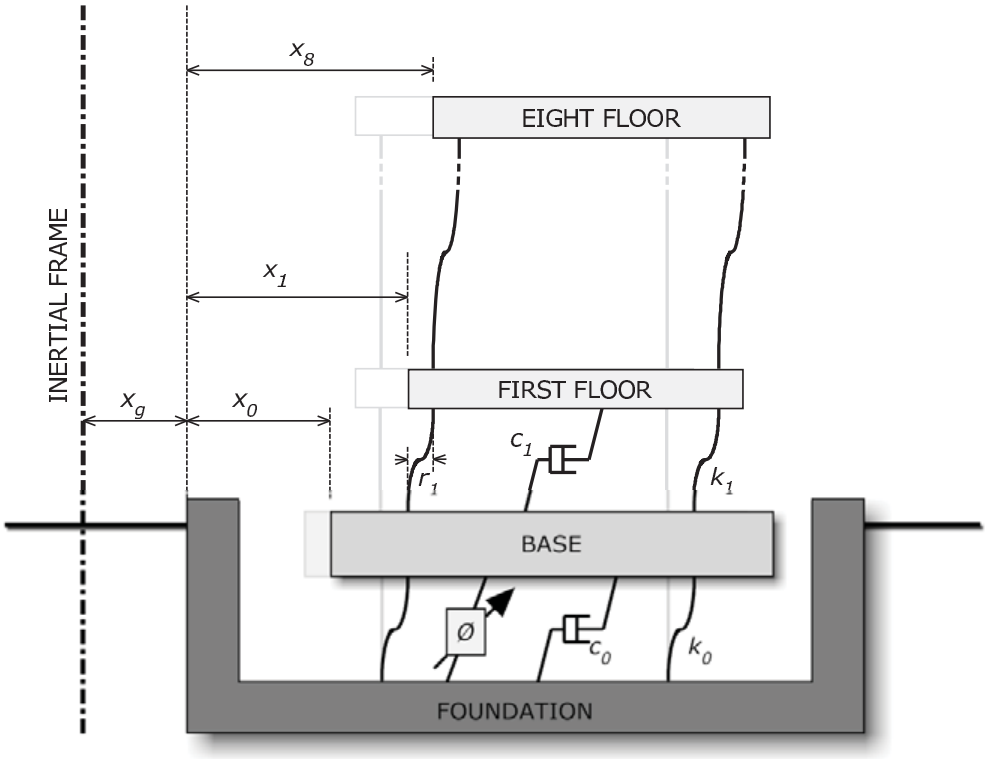

Figure 4.1: Base isolated structure with semi-active device.

where $\ddot{x}_0$ is the relative base acceleration, $\mathbf{x} = [x_1, x_2, \cdots, x_8]^{\mathrm{T}} \in \mathbb{R}^8$ represents the horizontal displacements of each floor with respect to the ground. The mass, damping and stiffness of the ith story is denoted by m_i, c_i and k_i, respectively, and r_1 represents the horizontal displacements of the first floor relative to the base (Fig. 4.1). As the base is assumed rigid, it is described as a single degree of freedom with horizontal displacement x_0. The nonlinearity, which is represented by a hysteretic restoring force ϕ, comes from MR damper which is installed at the base. The matrices $\boldsymbol{M}$, $\boldsymbol{C}$, $\boldsymbol{K}$, $\mathbf{F}_c$ and $\mathbf{F}_k$ of the structure have the following form:

$$\boldsymbol{M} = \mathrm{diag}(m_1, m_2, \cdots, m_8) \in \mathbb{R}^{8\times 8}$$

$$\boldsymbol{C} = \begin{bmatrix} c_1 + c_2 & -c_2 & & & & \\ -c_2 & c_2 + c_3 & -c_3 & & \underset{\sim}{0} & \\ & & \ddots & & & \\ & \underset{\sim}{0} & & -c_7 & c_7 + c_8 & -c_8 \\ & & & & -c_8 & c_8 \end{bmatrix} \in \mathbb{R}^{8\times 8}$$

$$\boldsymbol{K} = \begin{bmatrix} k_1 + k_2 & -k_2 & & & & \\ -k_2 & k_2 + k_3 & -k_3 & & \underset{\sim}{0} & \\ & & \ddots & & & \\ & \underset{\sim}{0} & & -k_7 & k_7 + k_8 & -k_8 \\ & & & & -k_8 & k_8 \end{bmatrix} \in \mathbb{R}^{8\times 8}$$

$$\mathbf{J} = [1, \cdots, 1]^{\mathrm{T}} \in \mathbb{R}^8$$
$$\mathbf{F}_c = [c_1\dot{x}_0, 0, \ldots, 0]^T \in \mathbb{R}^8$$
$$\mathbf{F}_k = [k_1 x_0, 0, \ldots, 0]^T \in \mathbb{R}^8$$

The restoring force ϕ can be calculated based on the extended normalized version of the Bouc-Wen model (2.10)-(2.11).

Assuming that the earthquake disturbance is unknown but

bounded, the following velocity feedback control law is considered [90]:

$$f_{\mathrm{d}} = -\zeta \ \mathrm{sgn}(\dot{x}_0) \tag{4.3}$$

where ζ is a positive real number and f_{d} is the desired control force.

4.3.2 The selection of the command voltage v

It is well known that the force generated by the MR damper cannot be directly commanded; only the voltage v applied to the current driver for the MR damper can be directly changed [27]. In the clipped-optimal control algorithm [27], the command voltage takes the values zero or the maximum, according to

$$v = V_{\max} H\left\{(f_{\mathrm{d}} - \Phi)\Phi\right\},$$

where $V_{\max}$ is the maximum voltage to the current driver associated with saturation of the magnetic field in the MR damper, $H(\cdot)$ is the Heaviside step function, f_{d} is the desired control force and Φ is the measured force of the MR damper. In some situations, when the dominant frequencies of the system under control are low, large changes in the forces applied to the structure may result in high local acceleration [123]. In this sense, a modification to the original clipped-optimal control algorithm in which the control voltage can be any value between zero and $V_{\max}$, was proposed in [123]. A similar approach can be found in [37], where a force-feedback control scheme is employed to overcome the difficulty of commanding the MR damper to produce an arbitrary force.

In this work we consider the same idea of changing the voltage but according to the inverse model proposed in Chapter 3. More precisely, if passivity (3.5) and limitation (3.7) constraints are satisfied then, to induce the MR damper to generate approximately the desired control force f_{d}, the algorithm for selecting

the command signal can be concisely stated as

$$v = \frac{f_{\mathrm{d}} - (\kappa_x x + \kappa_{\dot{x},a}\dot{x} + \mathrm{sgn}(\dot{x})\kappa_{w,a})}{\kappa_{\dot{x},b}\dot{x} + \mathrm{sgn}(\dot{x})\kappa_{w,b}}, \tag{4.4}$$

where f_{d} is computed according to equation (4.3).Note that is just the inverse model (3.4) where the desired control force is used as reference input force. Both equations (4.3)-(4.4) define a semi-active controller. Figure 4.2 illustrates the corresponding closed-loop system.

4.4 Hierarchical control scheme

In the benchmark building considered in this study, MR dampers are placed at eight specific locations (Figure 4.3). At each location, there are two controllers –one in the x- and the other in the y-direction. These actuators are used to apply the damping control forces to the base of the structure.

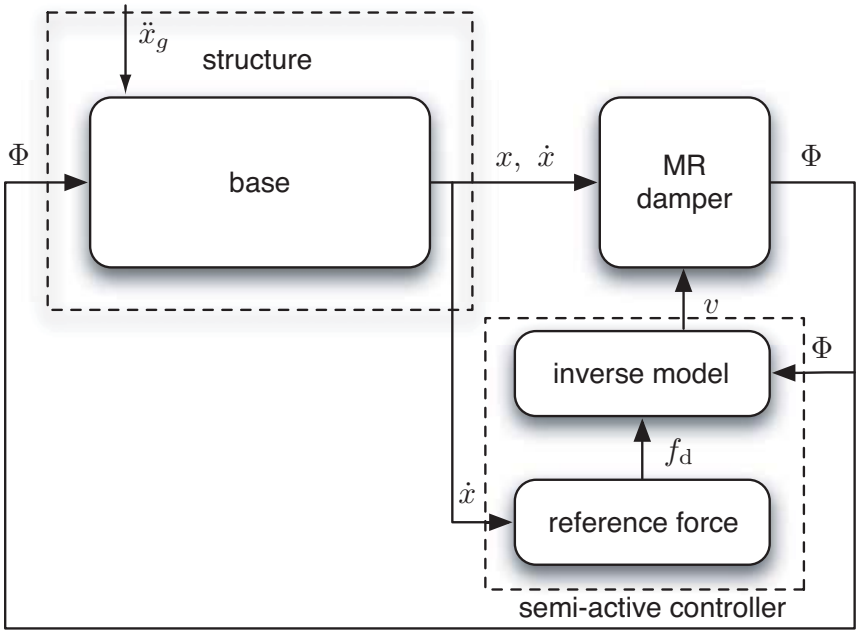

Figure 4.2: Block diagram of the semi-active control system for a single MR damper.

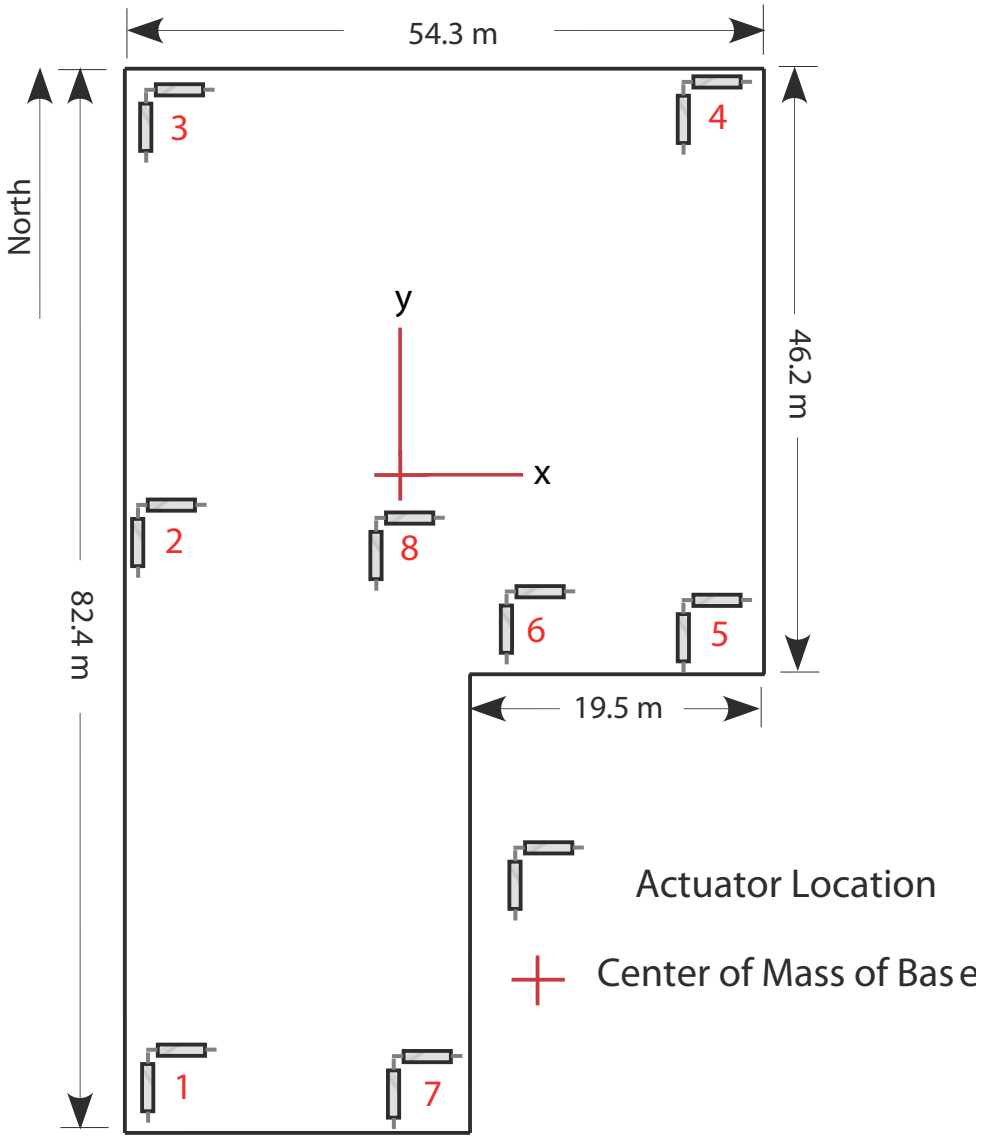

Figure 4.3: Locations of MR dampers.

This section proposes an overall strategy to implement the previous control loop no through a single damper but by means of a set of several MR dampers.

$$L = \{i \in \{1, \dots 8\} \mid \text{sgn}(f^i_{\text{MR}})\text{sgn}(f_{\text{d}}) > 0\}.$$

Let N be the cardinal of this set.

The final goal of the semi-active control scheme is that the total damping force generated by the whole set of MR dampers closely follows the desired control force f_{d}. With this aim, a hierarchical semi-active control strategy is proposed, as illustrated in Figure 4.4. With this scheme, we have to decide whether it is necessary to apply voltage to the dampers, to which dampers, and the magnitude of the voltage. More precisely, this procedure can be summarized in the following steps to be implemented real-time at each sampling instant:

`Step 1`. Compute the desired control force f_{d}, according to the control law in equation (4.3).

`Step 2`. If the magnitude of the total damping force generated by the MR dampers, $f_{\text{MR}} := \sum_{i=1}^{8} f^i_{\text{MR}}$, is smaller than the magnitude of the desired control force f_{d} and the two forces have the same sign, that is, if the following expression holds

$$(f_{\text{d}} - f_{\text{MR}})\, f_{\text{MR}} > 0,$$

it means that the MR dampers need to apply more damping force and then we go to `Step 3`. Otherwise, the voltage applied to each damper is set to $v_i = 0,\ i = 1, \dots, 8$, and we leave them work *passively*.

`Step 3`. Compute the number of dampers that are applying force in the same direction that the desired control force. As a consequence of the base rotation during excitation, the displacement (the value and the sign) of the MR dampers installed in different locations of the base may be different

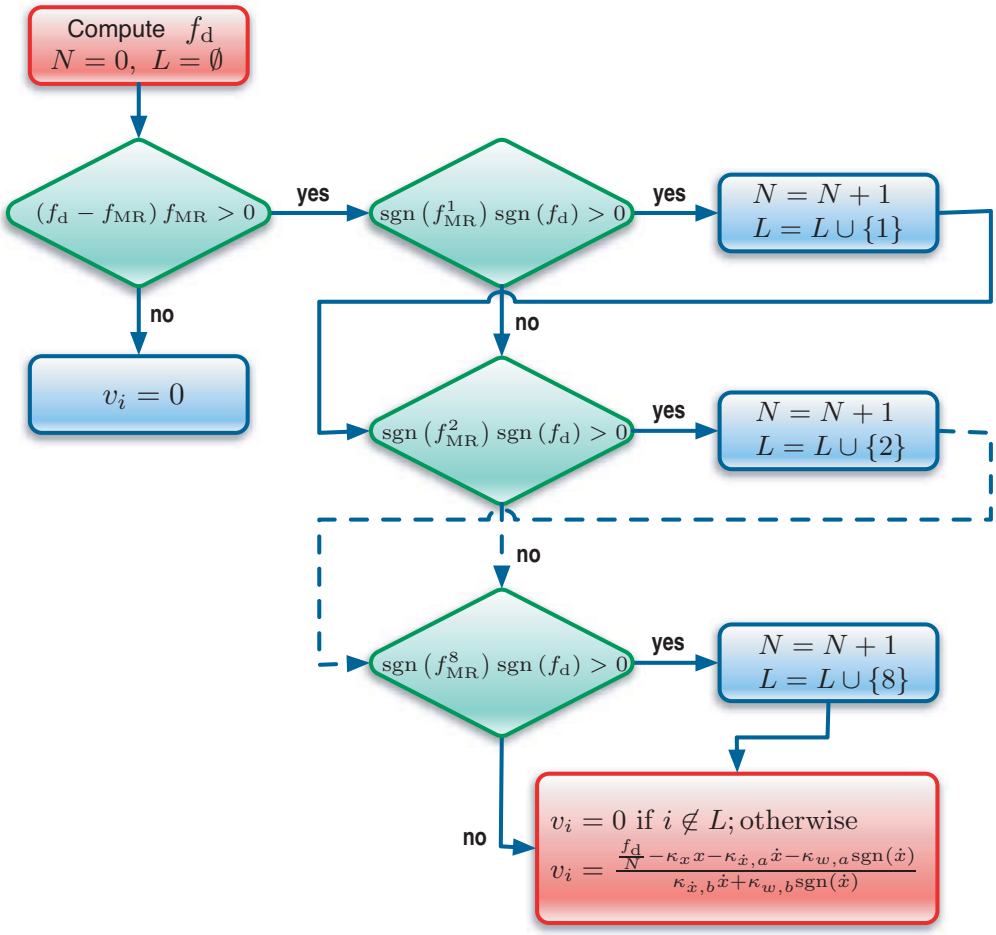

Figure 4.4: Hierarchical semi-active control: flow diagram.

(Figure 4.5). In this sense, we define the following set:

$$L = \{i \in \{1, \ldots 8\} \mid \mathrm{sgn}(f^i_{\mathrm{MR}})\,\mathrm{sgn}(f_{\mathrm{d}}) > 0\}.$$

Let N be the cardinal of this set.

`Step 4.` Compute the corresponding command voltage. Each of the N dampers has to offer a part of the control force equal to $\frac{f_{\mathrm{d}}}{N}$. Based on this desired value and equation (4.3), the corresponding command voltage that has to be

applied to each damper will be calculated in the form

$$v_i = \frac{\frac{f_{\mathrm{d}}}{N} - \kappa_x x - \kappa_{\dot{x},a}\dot{x} - \kappa_{w,a}\,\mathrm{sgn}(\dot{x})}{\kappa_{\dot{x},b}\dot{x} + \kappa_{w,b}\,\mathrm{sgn}(\dot{x})}, \quad i \in L,$$
$$v_i = 0, \quad i \notin L.$$

Finally, to take into account the effect of the constraints in the procedure, the implementation of the law (3.7) will be along with the truncation of the resulted values between

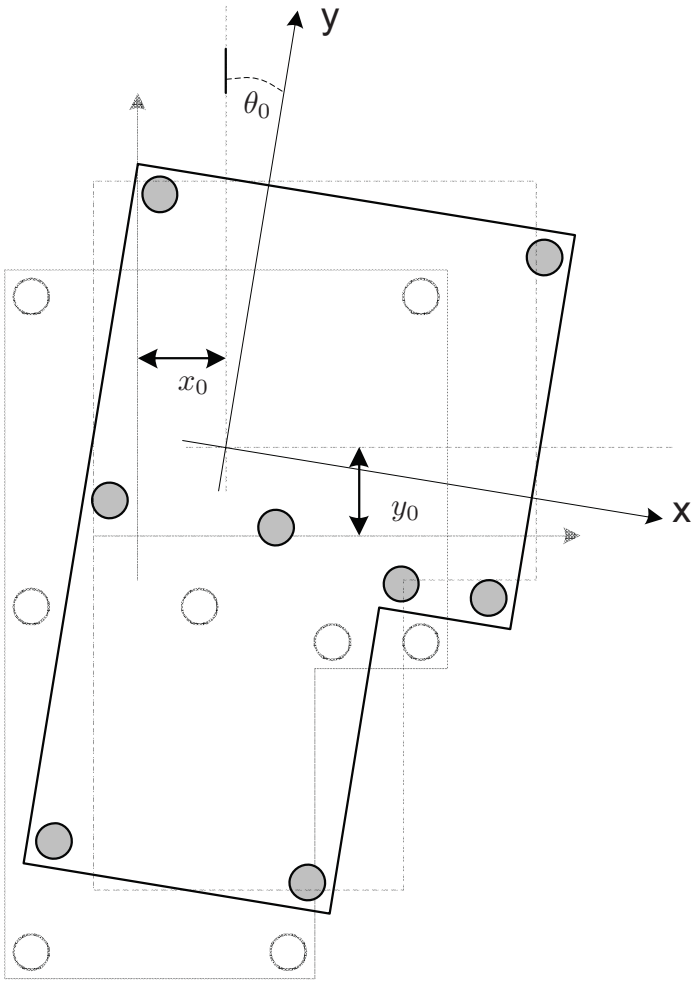

Figure 4.5: Effects of the base rotation on the resulted displacement of MR dampers.

zero and one. If the desired control force is less than the minimum realizable damping force of an specific damper, the inverse model will result in a negative voltage. In this case the output voltage will be zero. On the other hand, if the calculated voltage is greater than one, it means that the desired control force is greater than the maximum available force for that specific MR damper in that specific instant. Consequently, the output voltage will be one. More precisely, the applied voltage v_a will be finally computed as:

$$v_a = \min\{\max\{0, v(x, \dot{x}, f_{\mathrm{d}})\}, 1\}.$$

4.5 Conclusion

A hierarchical semi-active control strategy has been presented in this chapter for a building controlled by means of a set of MR dampers. The inverse model of an MR damper, proposed in Chapter 3, has been used to overcome the difficulty of commanding the MR dampers to follow the desired control force. The management of the MR dampers is based on a hierarchical strategy. The whole method will be applied and numerically validated in Chapter 5 on a three-dimensional smart base-isolated benchmark building which is used by the structural control community as a state-of-the-art model for numerical experiments of seismic control attenuation.

Chapter 5

Numerical assessment

5.1 Introduction

The performance of the semi-active control algorithm presented in Chapter 4 is now evaluated through numerical simulation using the smart base-isolated benchmark building. The smart base-isolated benchmark building [81] is employed as an interesting and more realistic example to further investigate the effectiveness of the proposed design approach. This benchmark problem is recognized by the American Society of Civil Engineers (ASCE) Structural Control Committee as a state-of-the-art model developed to provide a computational platform for numerical experiments of seismic control attenuation [86, 102].

The benchmark structure is an eight-storey frame building with steel-braces, similar to existing buildings in Los Angeles, California. Stories one to six have an L-shaped plan while the higher floors have a rectangular plan. The superstructure rests on a rigid concrete base, which is isolated from the ground by an isolator layer that consists of a variety of 92 isolation bearings. Figure 5.1 represents the benchmark structure (for more details refer to the Appendix B).

The results of the semi-active control strategy are presented for the fault normal (FN) and the fault parallel (FP) components acting in two perpendicular directions. The results are also compared with the clipped-optimal control algorithm in [27] and

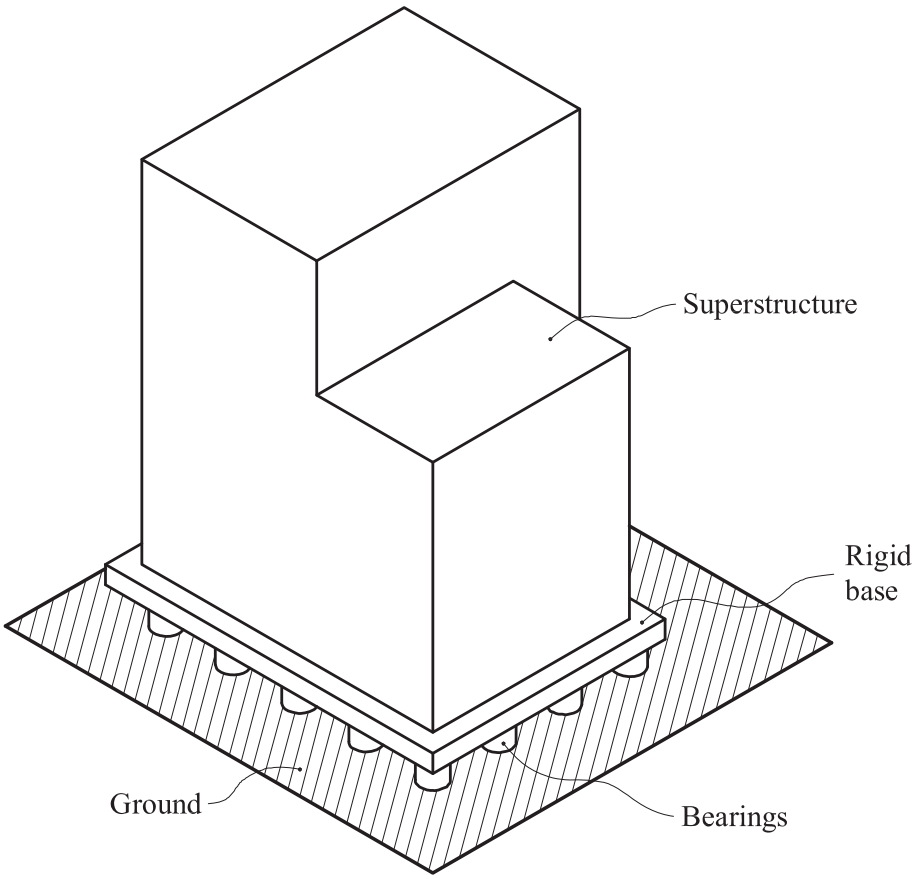

Figure 5.1: A representative figure of the benchmark structure.

also with two limit cases: *passive off* and *passive on*, that corresponds to the cases of *zero* voltage and *maximum* voltage. The evaluation is reported in terms of the performance indices described in the Appendix B. The controlled benchmark structure is simulated for seven earthquake ground accelerations defined in the benchmark problem (Newhall, Sylmar, El Centro, Rinaldi, Kobe, Ji-Ji and Erzinkan). All the excitations are used at the full intensity for the evaluation of the performance indices. The performance indices larger than one indicate that the response of the controlled structure is bigger than that of the uncontrolled structure.

5.2 Simulation procedure

To evaluate the hierarchical semiactive control in the base-isolated benchmark building, the black-box model of the MR damper that is implemented in the original program has been replaced by the corresponding identified model in Chapter 2. The overall aspect of the simulation for the hierarchical semiactive control is presented in Figure 5.2. The control block in the program has been replaced with the hierarchical semiactive control scheme (Figure 4.4) to calculate the desired value of command voltages for each of the MR dampers.

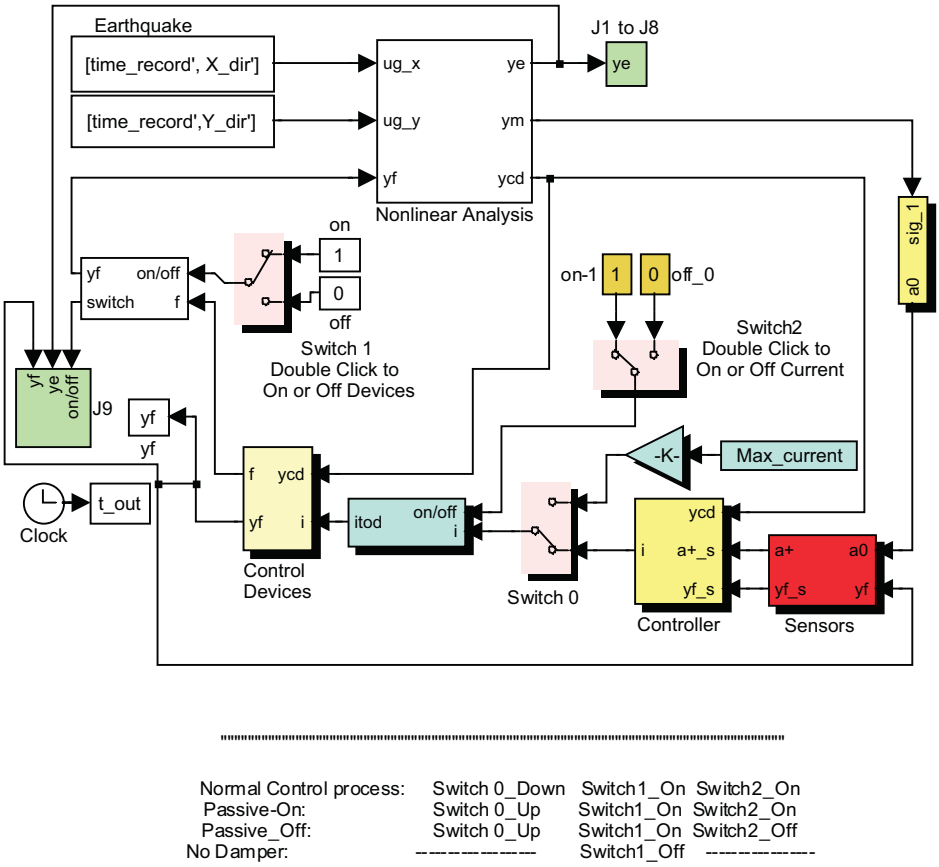

Normal Control process:	Switch 0_Down	Switch1_On	Switch2_On
Passive-On:	Switch 0_Up	Switch1_On	Switch2_On
Passive_Off:	Switch 0_Up	Switch1_On	Switch2_Off
No Damper:	----------	Switch1_Off	----------

Figure 5.2: Simulation block for hierarchical semi-active control of the benchmark building structure.

Figures 5.3 and 5.4 show the MR damper model simulink block and the hierarchical semiactive control scheme, respectively.

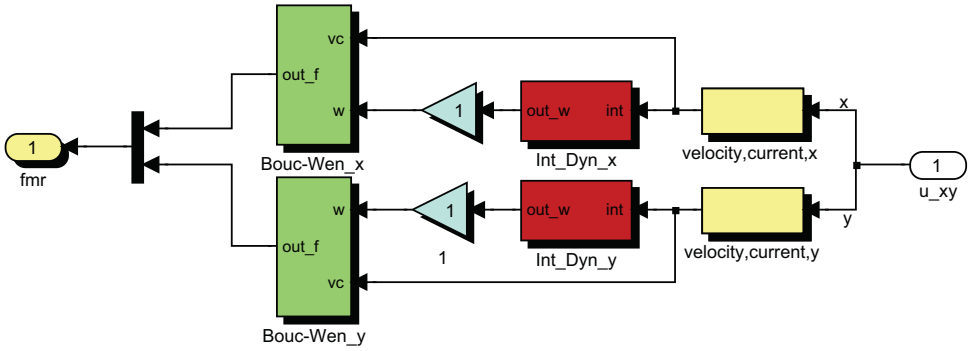

Figure 5.3: MR damper model block.

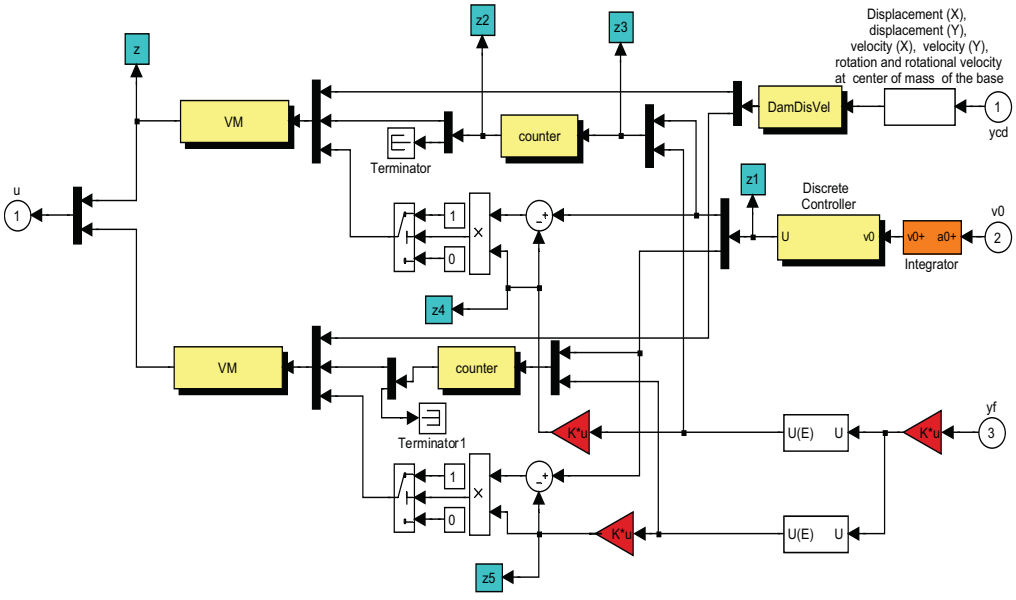

Figure 5.4: Hierarchical semi-active control scheme.

5.3 Performance indices

The results of the semi-active control strategy are summarized in Tables 5.1 and 5.2. The performance indices larger than one are highlighted in bold. In this control strategy most of the response quantities are reduced substantially from the uncontrolled cases.

The base and structural shears are reduced between 5% and 29% in all cases. The reduction in base displacement is between 11% and 68% also in all cases. Reductions in the inter-storey drifts between 3% and 40% are achieved in a majority of earthquakes (except Newhall) when compared to the uncontrolled case. The floor accelerations are also reduced by 1-14% in a majority of earthquakes (except Newhall, El Centro and Kobe).

The benefit of the presented scheme is the reduction of base displacements (J_3) and shears (J_1, J_2) of up to 30% without increase in drift (J_4) or accelerations (J_5). The reduction of the peak base displacement J_3 of the base-isolated building is one of the most important criteria during strong earthquakes.

For the base-isolated buildings, superstructure drifts are reduced significantly compared to the corresponding fixed-buildings because of the isolation from the ground motion. Hence, a controller that reduces or does not increase the peak superstructure drift (J_4), while reducing the base displacement significantly (J_3), is desirable for practical applications. In this respect, the proposed semi-active controller performs well.

Table 5.1: Evaluation criteria for the proposed semi-active scheme compared with the clipped-optimal control algorithm in [27] and also with two limit cases: *passive off* and *passive on* (FP-x and FN-y).

Earthq.	Case	J_1	J_2	J_3	J_4	J_5	J_6	J_7	J_8	J_9
Newhall	P-On	0.91	0.95	0.51	**1.30**	**2.49**	0.34	0.25	**1.07**	0.89
	P-Off	0.93	0.91	0.81	0.94	0.97	0.05	0.71	0.86	0.41
	Clip.	0.97	**1.01**	0.56	**1.03**	**1.48**	0.30	0.33	0.89	0.79
	Prop.	0.83	0.84	0.61	0.94	**1.09**	0.19	0.36	0.69	0.79
Sylmar	P-On	0.90	0.92	0.66	0.81	**1.49**	0.25	0.40	0.82	0.86
	P-Off	0.98	0.97	0.95	0.96	0.99	0.04	0.82	0.91	0.35
	Clip.	0.90	0.91	0.73	0.87	**1.16**	0.24	0.45	0.74	0.81
	Prop.	0.89	0.90	0.78	0.82	0.98	0.12	0.56	0.72	0.69
El Centro	P-On	0.73	0.87	0.14	**1.23**	**2.85**	0.67	0.09	**1.61**	0.82
	P-Off	0.96	0.94	0.76	0.84	0.87	0.05	0.69	0.73	0.50
	Clip.	**1.25**	**1.23**	0.54	**1.26**	**1.61**	0.38	0.41	0.76	0.65
	Prop.	0.72	0.71	0.32	0.60	**1.08**	0.42	0.18	0.69	0.86
Rinaldi	P-On	0.94	0.96	0.50	0.97	**1.12**	0.29	0.27	0.83	0.86
	P-Off	**1.00**	**1.00**	0.95	0.99	**1.01**	0.05	0.84	0.86	0.34
	Clip.	**1.05**	**1.02**	0.60	0.97	**1.03**	0.27	0.38	0.72	0.77
	Prop.	0.91	0.90	0.73	0.85	0.86	0.13	0.49	0.56	0.71
Kobe	P-On	0.84	0.81	0.36	**1.19**	**2.33**	0.39	0.16	**1.14**	0.87
	P-Off	0.88	0.88	0.80	0.91	0.98	0.05	0.78	0.83	0.40
	Clip.	**1.05**	**1.03**	0.52	0.99	**1.63**	0.28	0.26	0.73	0.73
	Prop.	0.77	0.78	0.45	0.72	**1.05**	0.20	0.27	0.56	0.77
Jiji	P-On	0.83	0.82	0.65	0.86	0.92	0.17	0.42	0.82	0.70
	P-Off	0.96	0.96	0.93	0.96	0.96	0.03	0.85	0.91	0.25
	Clip.	0.84	0.84	0.65	0.86	0.87	0.17	0.46	0.72	0.64
	Prop.	0.94	0.95	0.84	0.97	0.99	0.06	0.68	0.82	0.48
Erzinkan	P-On	0.94	0.95	0.49	0.85	**1.21**	0.25	0.32	0.60	0.87
	P-Off	0.98	**1.00**	0.88	0.92	0.97	0.04	0.88	0.91	0.30
	Clip.	0.93	0.70	0.47	0.86	**1.23**	0.25	0.34	0.63	0.80
	Prop.	0.90	0.91	0.57	0.77	0.89	0.12	0.49	0.57	0.74

Table 5.2: Evaluation criteria for the proposed semi-active scheme compared with the clipped-optimal control algorithm in [27] and also with two limit cases: *passive off* and *passive on* (FP-y and FN-x).

Earthq.	Case	J_1	J_2	J_3	J_4	J_5	J_6	J_7	J_8	J_9
Newhall	P-On	0.83	0.93	0.51	**1.32**	**1.86**	0.34	0.33	**1.05**	0.89
	P-Off	0.90	0.92	0.87	**1.01**	**1.03**	0.04	0.81	0.87	0.40
	Clip.	0.88	0.92	0.55	**1.24**	**1.40**	0.30	0.42	0.84	0.79
	Prop.	0.79	0.82	0.62	**1.00**	**1.02**	0.17	0.47	0.70	0.78
Sylmar	P-On	0.79	0.78	0.68	0.80	**1.25**	0.25	0.46	0.67	0.85
	P-Off	0.98	0.98	0.99	0.97	0.98	0.03	0.86	0.85	0.34
	Clip.	0.80	0.79	0.74	0.79	0.92	0.24	0.51	0.61	0.81
	Prop.	0.85	0.83	0.89	0.80	0.87	0.09	0.62	0.61	0.68
El Centro	P-On	0.73	0.93	0.19	**2.18**	**3.46**	0.69	0.12	**1.99**	0.81
	P-Off	0.97	0.97	0.81	0.97	0.97	0.05	0.73	0.82	0.48
	Clip.	**1.26**	**1.25**	0.65	**1.41**	**1.93**	0.37	0.45	0.94	0.69
	Prop.	0.71	0.72	0.44	0.69	**1.06**	0.39	0.23	0.79	0.86
Rinaldi	P-On	0.88	0.93	0.53	0.93	**1.12**	0.28	0.24	0.58	0.87
	P-Off	0.93	0.98	0.89	**1.00**	**1.01**	0.05	0.83	0.82	0.34
	Clip.	0.98	**1.01**	0.62	0.99	**1.02**	0.27	0.30	0.47	0.78
	Prop.	0.84	0.81	0.63	0.90	0.90	0.13	0.40	0.42	0.72
Kobe	P-On	0.96	0.99	0.40	**1.30**	**2.24**	0.41	0.20	**1.44**	0.87
	P-Off	**1.01**	**1.01**	0.78	**1.00**	1.00	0.05	0.75	0.85	0.41
	Clip.	**1.15**	**1.20**	0.53	**1.33**	**1.47**	0.30	0.38	0.98	0.72
	Prop.	0.86	0.86	0.45	0.89	0.99	0.22	0.30	0.74	0.77
Jiji	P-On	0.74	0.74	0.63	0.75	0.77	0.17	0.40	0.74	0.70
	P-Off	0.97	0.97	0.92	0.97	0.97	0.03	0.86	0.89	0.26
	Clip.	0.74	0.73	0.63	0.73	0.80	0.17	0.46	0.61	0.64
	Prop.	0.91	0.91	0.81	0.91	0.92	0.05	0.69	0.76	0.48
Erzinkan	P-On	0.85	0.85	0.51	0.95	**1.13**	0.29	0.29	0.48	0.87
	P-Off	0.89	0.88	0.85	0.92	0.91	0.04	0.85	0.88	0.31
	Clip.	0.85	0.84	0.51	0.88	**1.16**	0.24	0.32	0.52	0.78
	Prop.	0.80	0.81	0.58	0.84	0.88	0.12	0.46	0.52	0.75

5.3.1 Time-history plots

Figure 5.5 shows the ground acceleration of *Erzinkan* earthquake. Figures 5.6-5.8 show the time-history plots of various response quantities for the uncontrolled building, and the building with the hierarchical semi-active control scheme using the *Erzinkan* FP-x and the FN-y earthquake. More precisely, Figure 5.6 presents the plots for the displacement of the center of the mass of the base in both the x and the y direction. The plotted quantities in Figure 5.7 are the eighth floor absolute acceleration in the x direction and in the y direction for both the uncontrolled and the controlled situations. Finally, the interstorey drift between the eighth and the seventh floors in both the x and the y direction is depicted in Figure 5.8. It is observed from these figures that the controlled response quantities can be effectively reduced compared with the uncontrolled case.

Figure 5.9 shows the desired control force and the total damping force of the magnetorheological dampers in the x direction and in the y direction. It can be somehow observed that the total force generated by the MR dampers can closely follow the desired control force. Consequently, the implementation strategy presented in Chapter 4 seems reasonable.

Figure 5.10 shows the resulted force in each of the MR dampers under *Erzinkan* excitation (FP-X). As can be seen, sometimes during vibration the sign of the damping force of MR dampers are different. During these periods, the controller makes the force of the contrary damper(s) as small as possible, which is corresponds to the zero voltage.

Figure 5.11 shows the corresponding command voltage of the MR dampers for the same simulation under *Erzinkan* earthquake (FP-X).

Figure 5.12 presents the floor displacement of the controlled base-isolated building respect to the base for *Erzinkan* earthquake (FP-X).

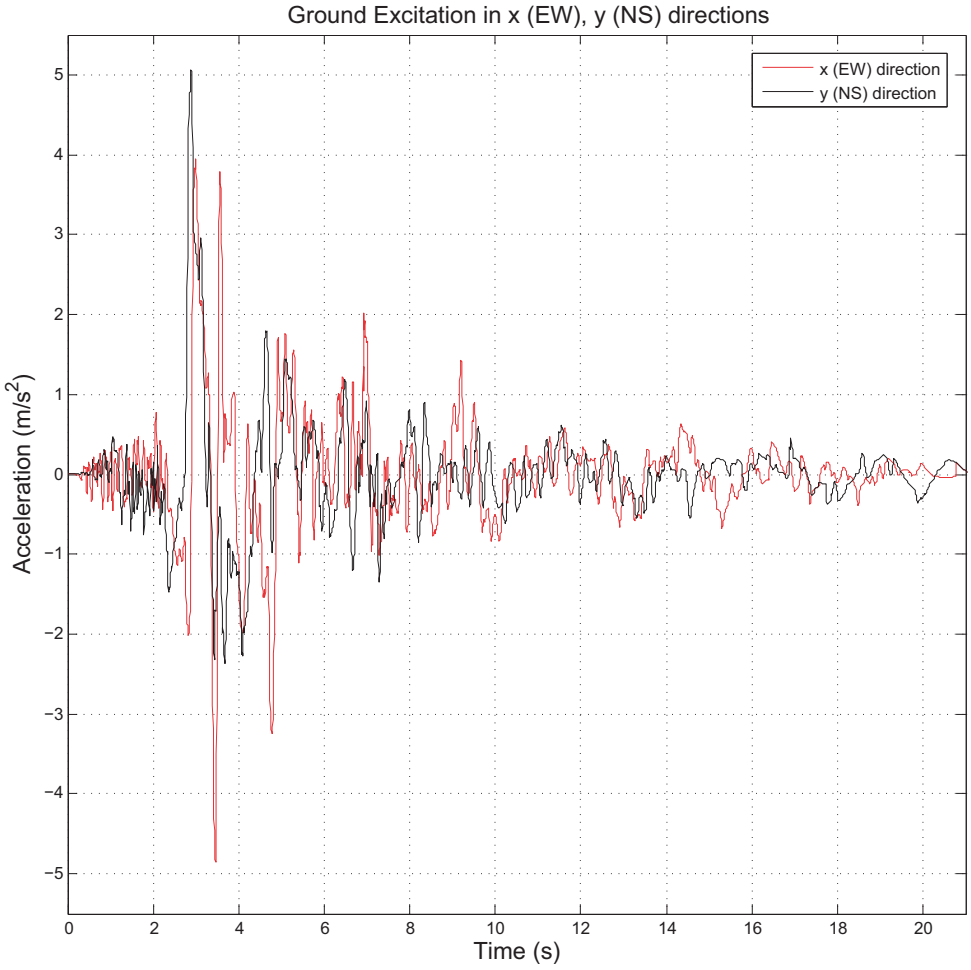

Figure 5.5: 1992 *Erzinkan* earthquake, ground acceleration.

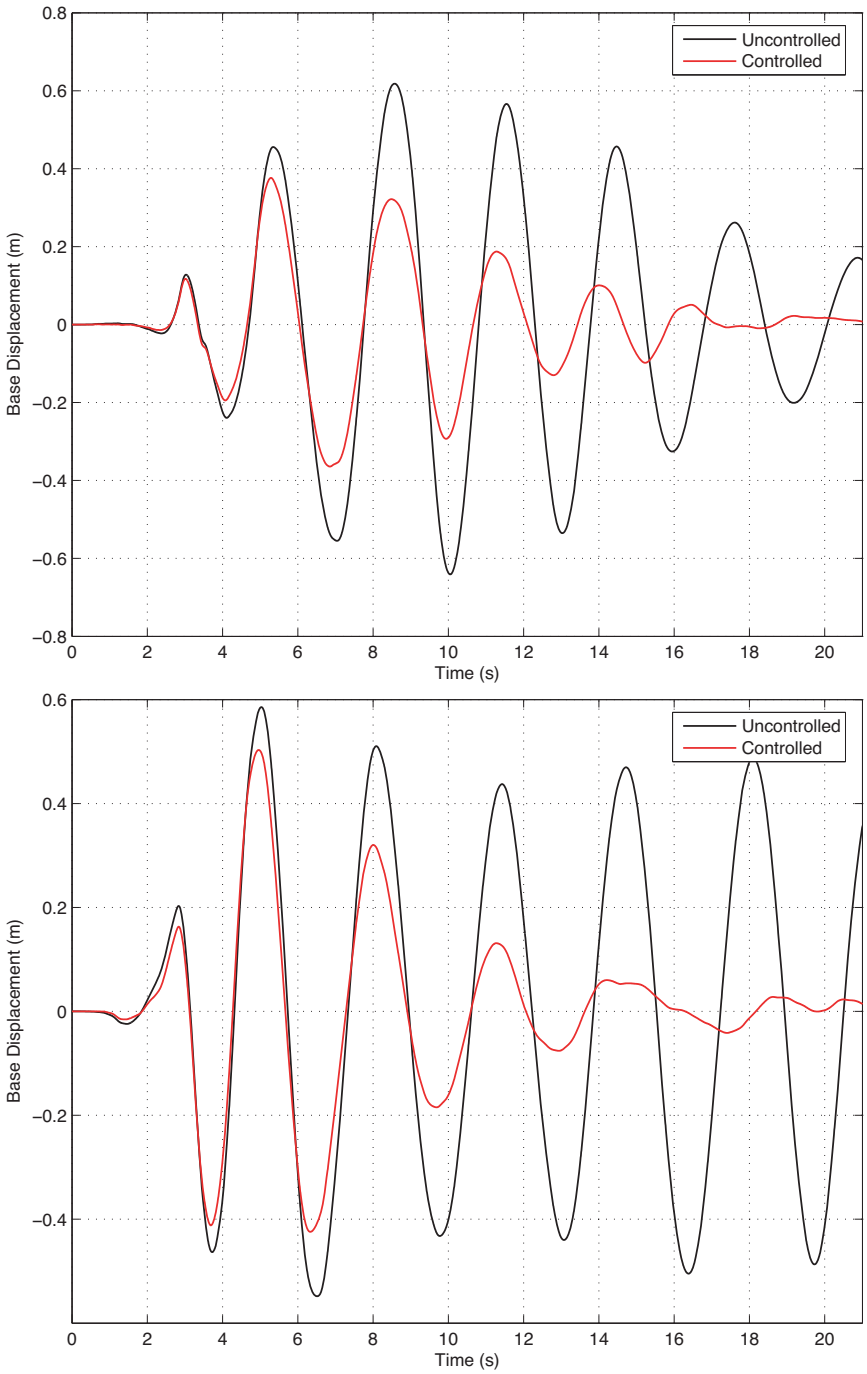

Figure 5.6: Time history of response of the isolated building under Erzinkan excitation. Displacement of the center of the mass of the base in the x-direction (up) and in the y-direction (down) for both the uncontrolled and the controlled situations.

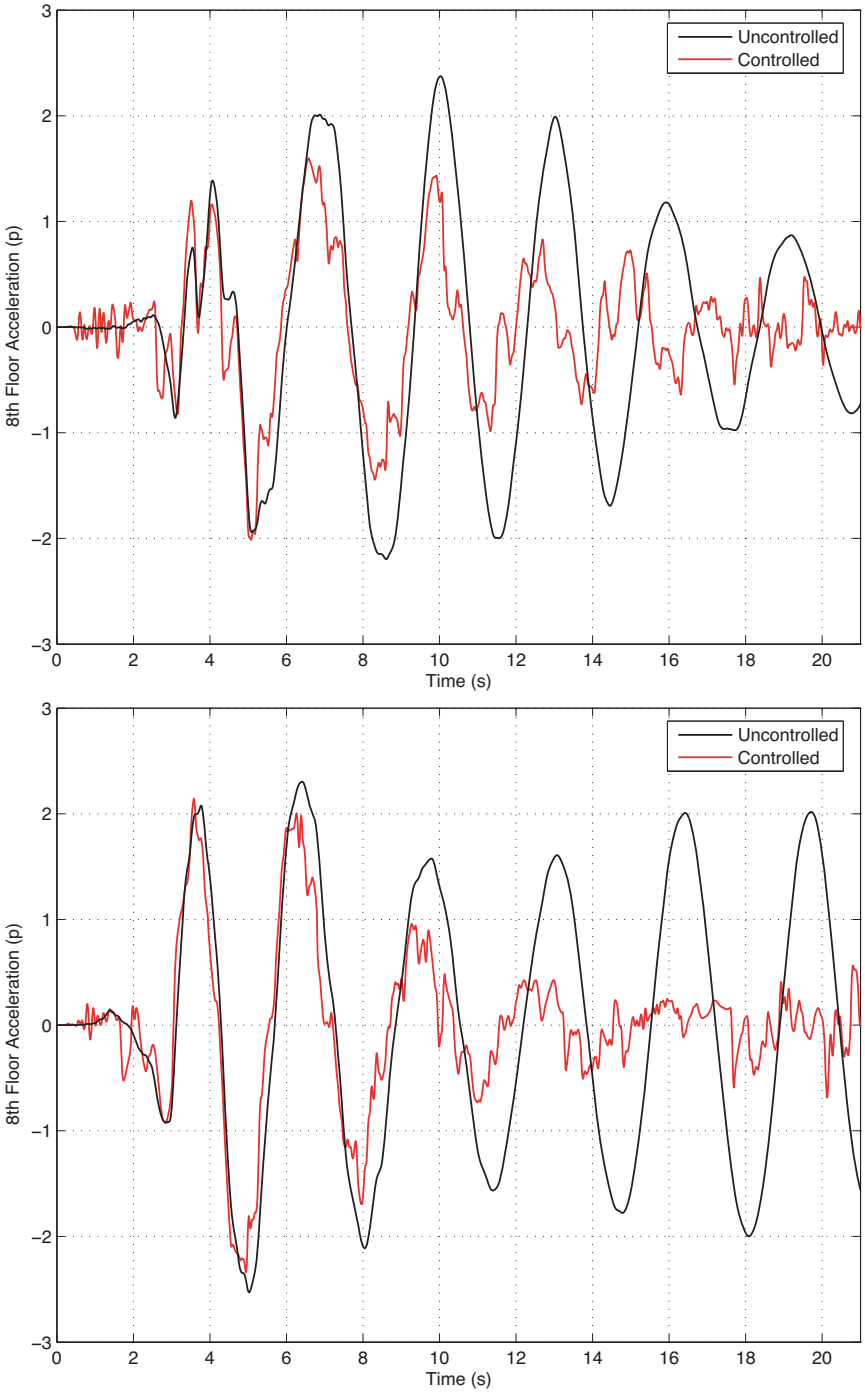

Figure 5.7: Time history of response of the isolated building under Erzinkan excitation. Absolute acceleration of the eighth floor in the x-direction (up) and in the y-direction (down) for both the uncontrolled and the controlled situations.

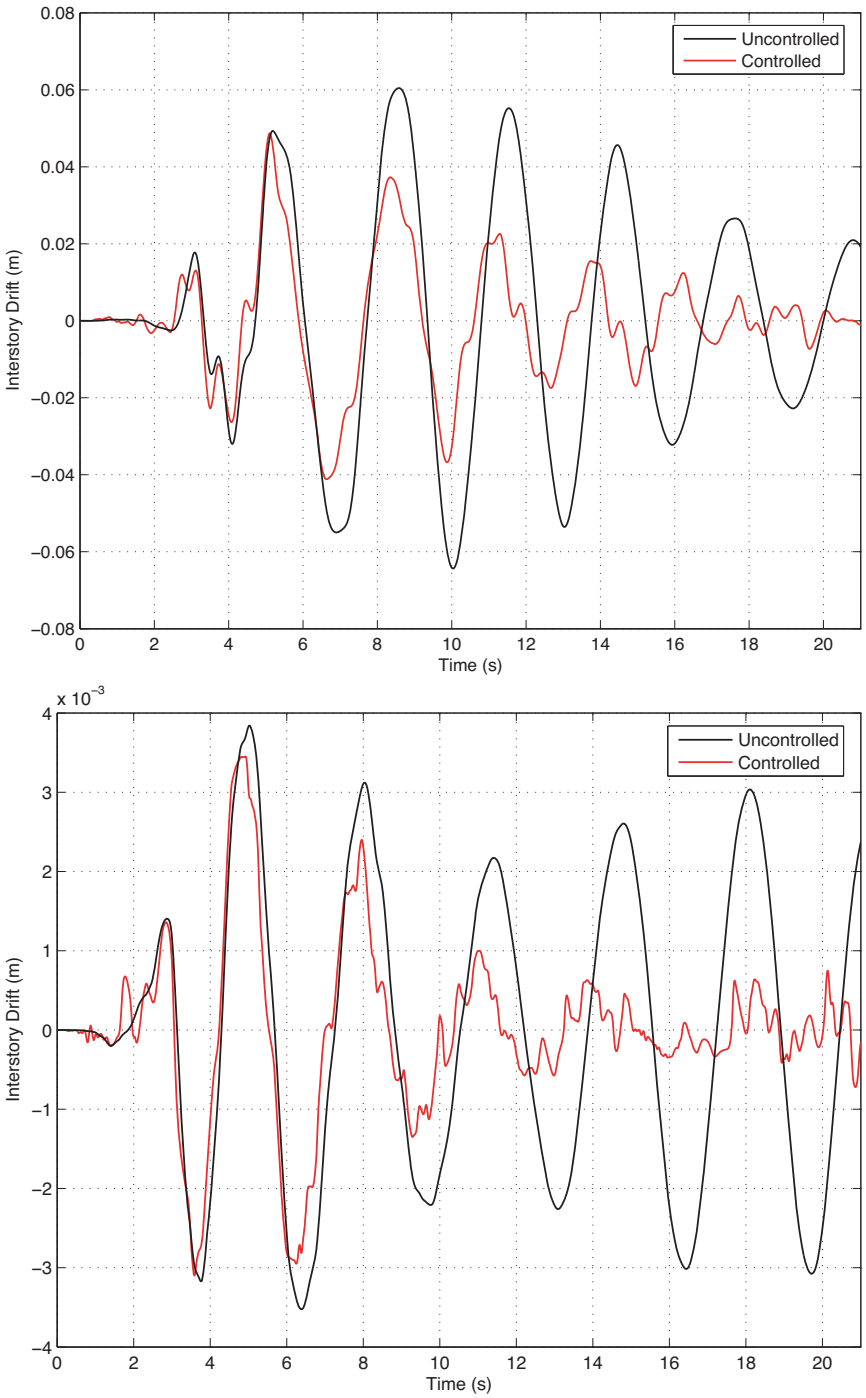

Figure 5.8: Time history of the isolated building under Erzinkan excitation. Interstorey drift between the eighth floor and the seventh floor in the x-direction (up) and in the y-direction (down) for both the uncontrolled and the controlled situations.

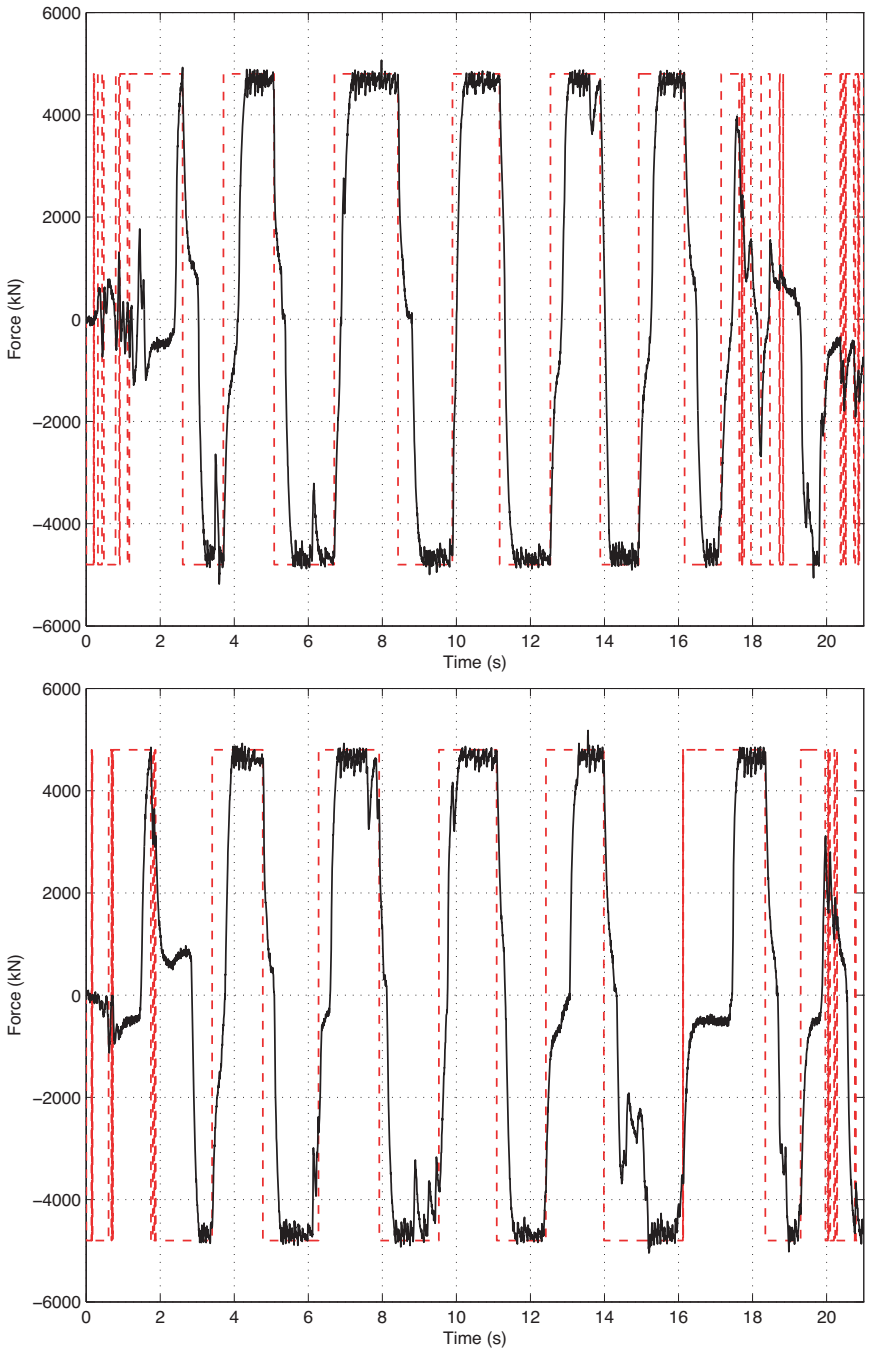

Figure 5.9: Time histories of the desired control force (dashed) and the control force generated by the magnetorheological dampers (solid) in the x-direction (up) and in the y-direction (down) under *Erzinkan* excitation.

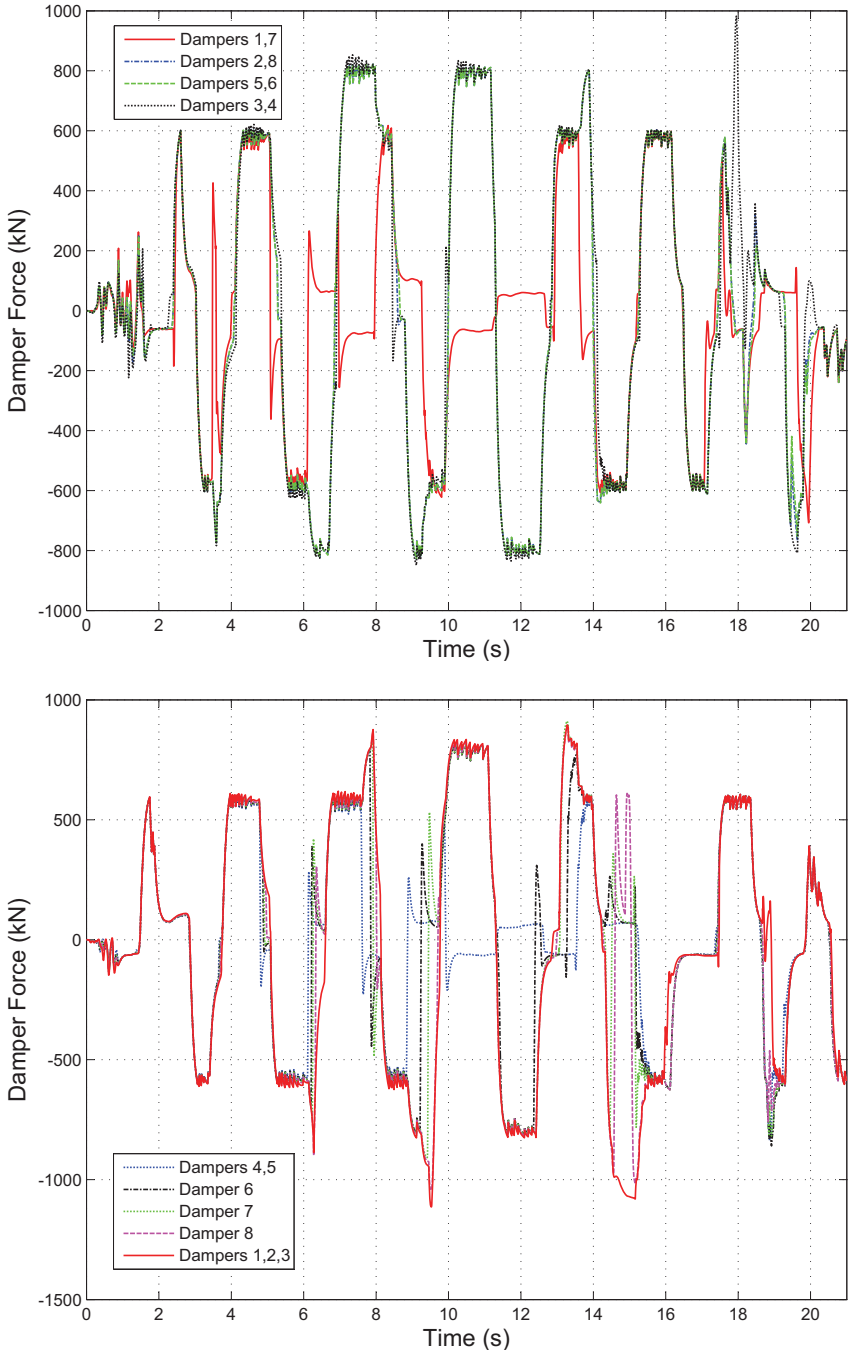

Figure 5.10: Time histories of the MR dampers force in the x-direction (up) and in the y-direction (down) under *Erzinkan* excitation.

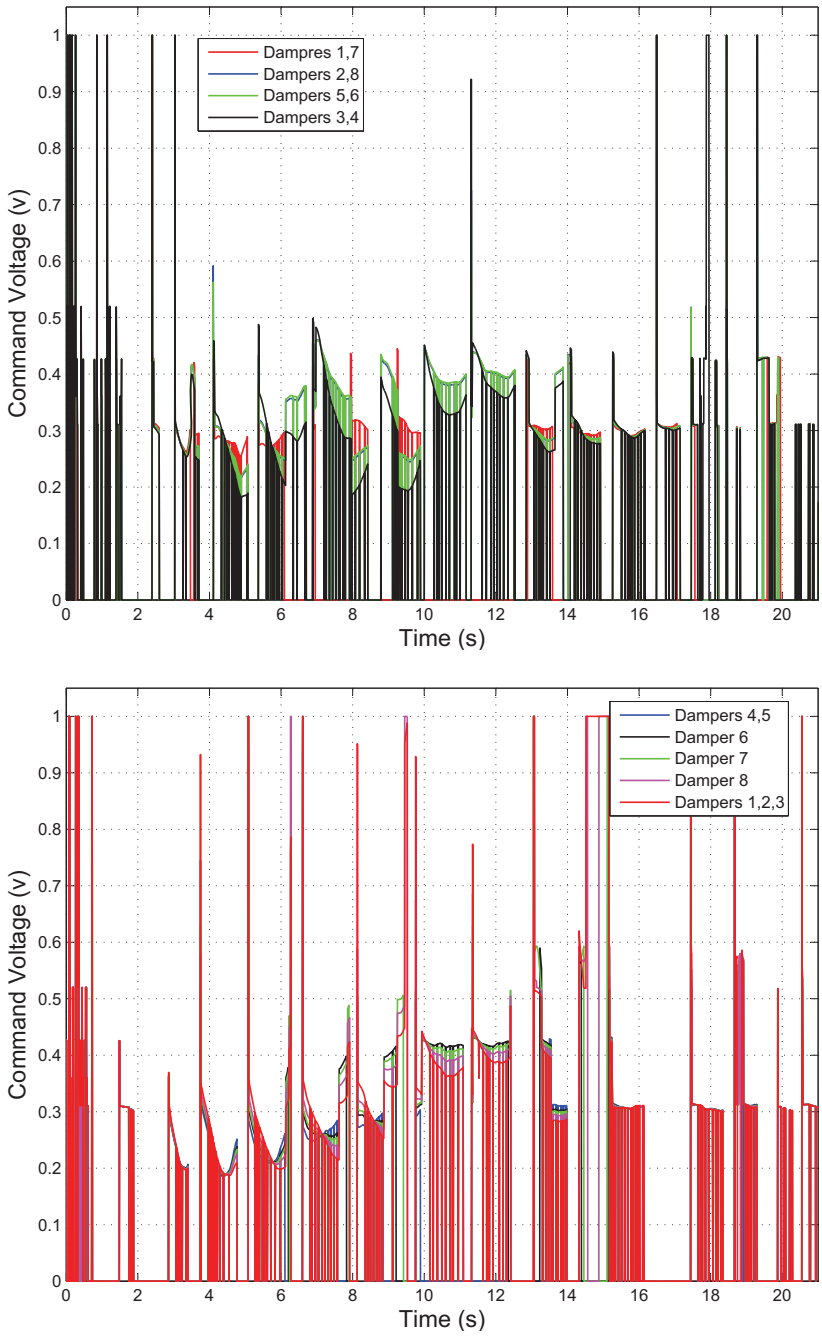

Figure 5.11: Time histories of the MR dampers command voltages in the x-direction (up) and in the y-direction (down) under *Erzinkan* excitation.

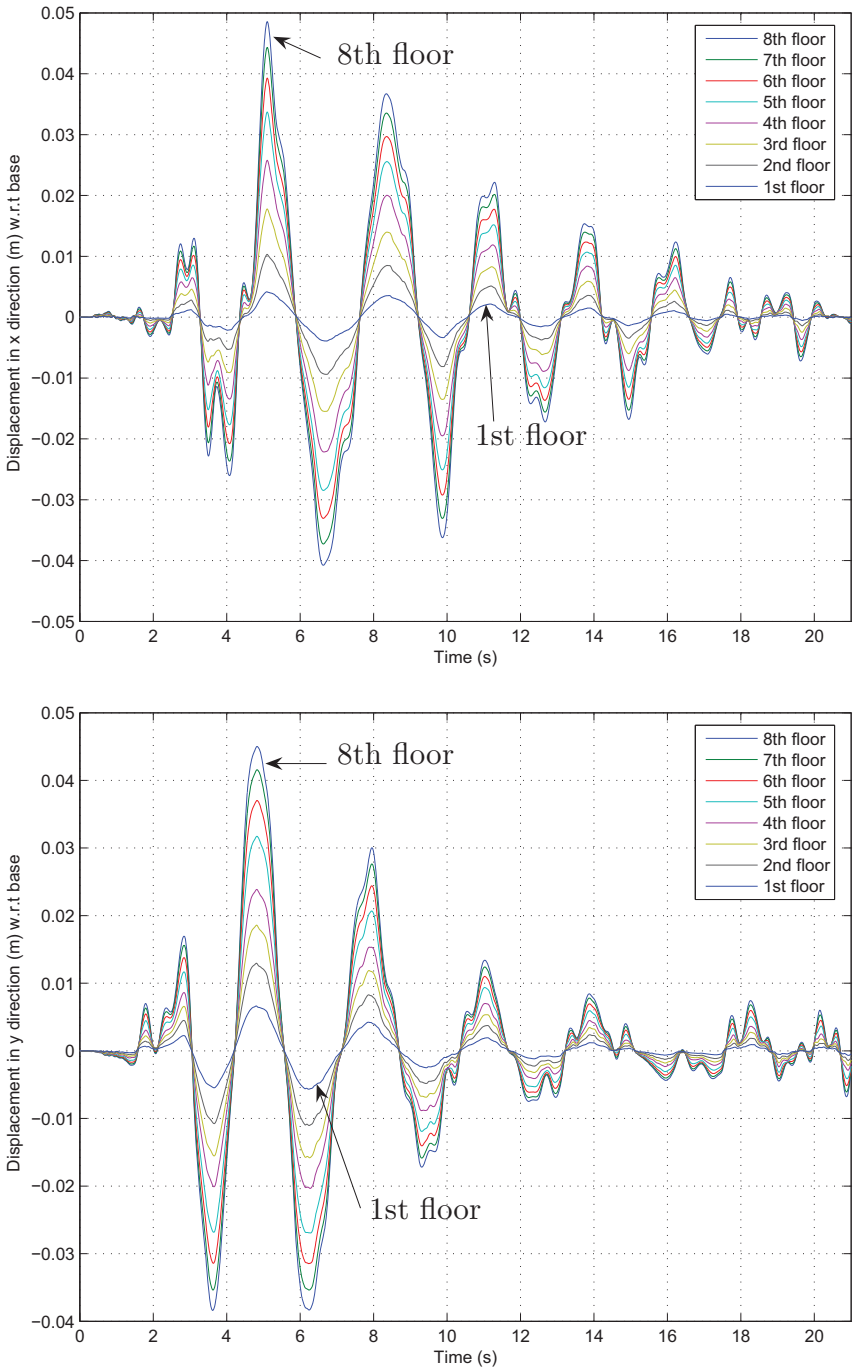

Figure 5.12: Displacement of the superstructure of the benchmark base-isolated building under *Erzinkan* Earthquake (FP-X), from 8th floor to the 1st one in the x and y-direction.

5.3.2 Comparison

Figure 5.13 shows that, as compared to the uncontrolled system –and for the Erzinkan excitation–, all of the isolation systems provide significant performance improvements in terms of reducing both peak and normed responses. The semi-active clipped optimal controller and the *passive on* performs better than the proposed hierarchical semi-active scheme with respect to the peak base displacement (J_3), but shows performance degradation with respect to the peak absolute floor acceleration (J_5). The results shown in Figure 5.13 demonstrates that the proposed semi-active scheme produces improved performance beyond the *passive off* controlled system for indices $J_1 - J_5$. The same conclusions can be drawn from Figure 5.14, where the performance indices under Kobe excitation are depicted. Overall, the proposed scheme produces simultaneous reduction in performance indices J_3, J_4 and J_5. Thus the goal of the hierarchical semi-active control, which is the simultaneous performance improvement of isolation system (J_3) and superstructure (J_4 and J_5) response, is achieved in the majority of cases. Therefore, the results provide validation of the effectiveness of the proposed algorithm.

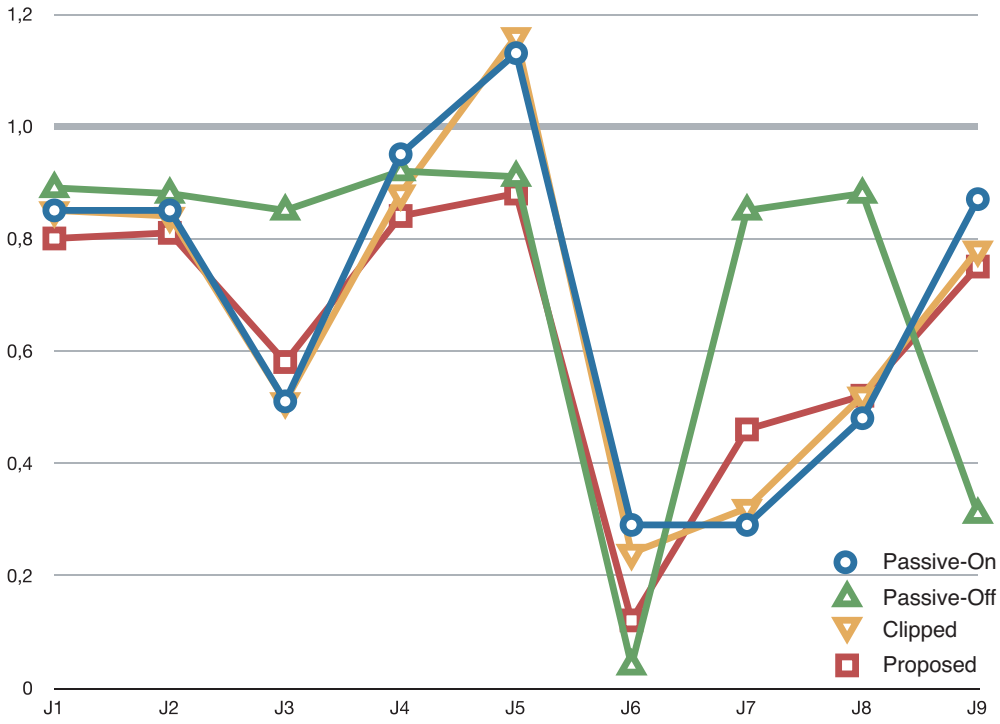

Figure 5.13: Comparison of performance indices for various control systems (*passive on*, *passive off*, clipped-optimal and the proposed one) under Erzinkan excitation (FP-y and FN-x).

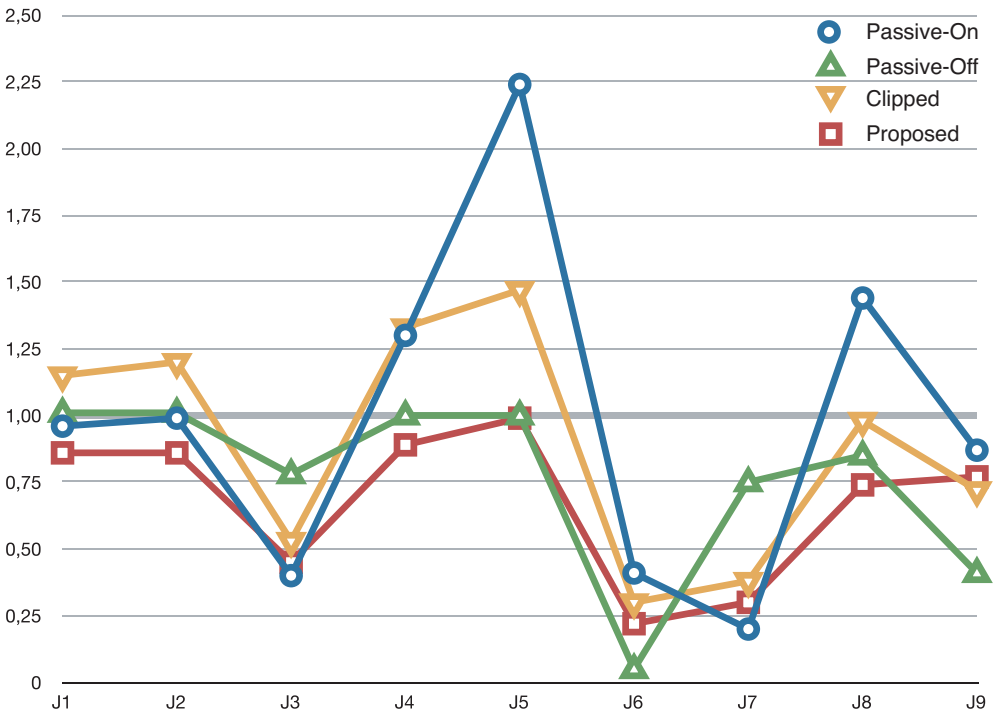

Figure 5.14: Comparison of performance indices for various control systems (*passive on*, *passive off*, clipped-optimal and the proposed one) under Kobe excitation (FP-y and FN-x).

5.4 Conclusion

The numerical results from simulation of a 3D benchmark base-isolation building with hierarchical semi-active controller presented. Resulted performance indices demonstrate that the proposal semi-active method can effectively suppress structural vibration caused by earthquake loading.

Chapter 6

Conclusions and future works

6.1 Conclusions

In Chapter 2 a new Bouc-Wen based normalized model for MR dampers has been developed to study the behavior of a wider range of MR dampers, specially the devices which can be more effective in the vibration control of real civil engineering structures (large-scale MR dampers). Based on this new model, an extension of a parameter identification method for MR dampers, has been proposed. This extension allows to identify a larger class of MR dampers more accurately. The validation of the parameter identification method has been carried out using a black-box model of an MR damper that is a part of a smart base-isolated benchmark building mode available in the community of researchers in structural control. The versatility of the parameter identification method has been tested using the MR damper as a semi-active device under time-varying voltage and earthquake excitation.

Chapter 3 has proposed a new inverse model for MR dampers. This model has been obtained based on two simplifications. First the piecewise nonlinear voltage dependent function κ_w is

replaced by a piecewise linear representation, and then the internal dynamic variable $w(t)$, which was a Bouc-Wen hysteretic variable, has been replaced by a Coulomb friction term. If two additional practical physical constraints are satisfied, then the voltage of the MR dampers can be manipulated by the inverse model.

Chapter 4 has presented a hierarchical semi-active control strategy for the control of the vibration response of isolated buildings equipped with a set of parallel MR dampers. The inverse model of an MR damper, proposed in Chapter 3, has also been implemented to overcome the difficulty of commanding the MR damper to follow the desired control force. The management of the set of MR dampers is based on a hierarchical strategy. This strategy consists of four steps applied in real time at each control instant:

1. Compute the overall desired control force to be applied at the base of the structure.

2. Determine the total force applied at the current control instant by the set of MR dampers. If this force is smaller than the desired force and they have the same sign, this means that the MR dampers need to apply more damping force and go to step 3. Otherwise the voltage of the MR dampers is set to 0.

3. Determine the number of dampers that are applying force in the same direction as the desired control force.

4. Compute the corresponding command voltage for each MR damper using the inverse model.

Chapter 5 has focused on the application of the proposed strategy. The whole method is simulated by considering the three-dimensional smart base-isolated benchmark building which is also used by the structural control community as a state-of-the-art model for numerical experiments of seismic control attenuation. The resulted performance indices demonstrate that the

proposed semi-active method can effectively improve the performance of the building under earthquake loading.

6.2 Future works

Possible future works involve:

- ▷ Experimental tests with a large-scale MR damper and application of the parameter identification methodology to find the system parameters and evaluation of the inverse model.
- ▷ Application of the hierarchical semi-active control strategy on other types of isolation systems (LRB, friction type or mixture of them).
- ▷ Add a sensor to measure the ground acceleration during earthquake excitation. This would allow to improve the calculation of the desired control force depending on the current ground excitation, which could lead to obtain more smooth variation of the command voltage.
- ▷ Numerical study on the influence of the number of the parallel MR dampers, their nominal damping force and distribution pattern. In other words try to answer to these questions:
  1. Which combination could be more effective, "less MR dampers with large damping capacity" or "more dampers with smaller nominal damping force"?
  2. What is the effect of their location in the resulted performance indices? Specially in the building with lateral-torsional effect.

Appendix A

Normalized Bouc-Wen identification method

The parameter identification in [93] departs from the next shear-mode model:

$$F_{\mathrm{n}}(x)(t) = \kappa_x(v)\dot{x}(t) + \kappa_w(v)w(t) \tag{A.1}$$

$$\dot{w}(t) = \rho(\dot{x}(t) - \sigma|\dot{x}(t)||w(t)|^{n-1}w(t) + (\sigma-1)\dot{x}(t)|w(t)|^n) \tag{A.2}$$

where $\kappa_x > 0$, $\kappa_w > 0$, $\rho > 0$, $\sigma > 1/2$, and $n \geq 1$. All of these parameters can be voltage or current dependent (here the case of voltage dependency are under consideration, as emphasized this dependency for $\kappa_{\dot{x}}$ and κ_w). It has shown [48] that this model is meaningful in the sense that the limit cycle depends directly on the parameters that appear in the normalized form, and thus depends only indirectly on the parameters of the standard form as

$$\begin{array}{ll} \rho = \frac{A}{Dz_0} > 0, & \sigma = \frac{\beta}{\beta+\gamma} \geq 0, \\ \kappa_x = \alpha k > 0, & \kappa_w = (1-\alpha)Dkz_0 > 0 \end{array} \tag{A.3}$$

where A, D, α, β, γ and k comes from the standard Bouc-Wen model

$$F_{\mathrm{BW}}(x)(t) = \alpha k x(t) + (1-\alpha) D k z(t) \tag{A.4}$$

$$\dot{z} = D^{-1}(A\dot{x} - \beta|\dot{x}|z|z|^{n-1} - \gamma\dot{x}|z|^{n}) \tag{A.5}$$

For parameter identification, a T-periodic input $x(t)$ (see Figure A.1) is applied to the Bouc-Wen system under constant voltage v/current i. Also, it has been proved [48] that the output force of the Bouc-Wen model goes asymptotically to a periodic steady-state status, so that a limit cycle is obtained. The identification method assumes the knowledge of the relation of the $\bar{w}(x)$ that describes this cycle as illustrated in Figure A.2. The whole identification process can be summarized as follows.

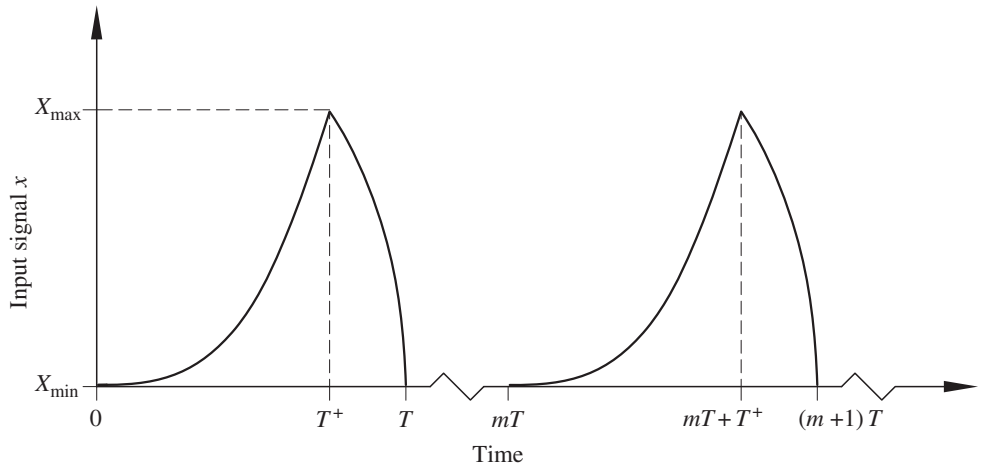

Figure A.1: A sample T-wave periodic signal.

The parameter κ_x is first determined using the plastic region ($\bar{w} \approx 1$) of the hysteresis loop by a linear regression for each constant voltage:

$$\bar{F}(\tau) = \kappa_x(v)\dot{x}(\tau) + \kappa_w(v).$$

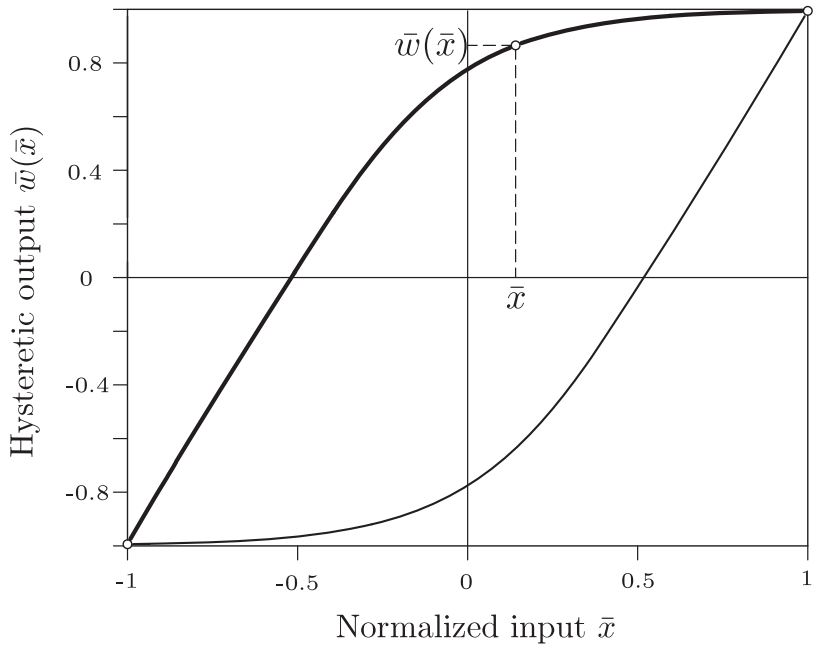

Figure A.2: Symmetry property of the hysteresis loop of the normalized Bouc–Wen model.

To continue with parametric estimation, a function θ is computed as:

$$\theta(x(\tau)) = \bar{F}(x(\tau)) - \kappa_{\dot{x}} \frac{dx(\tau)}{d\tau}, \quad \tau \in [0, T^+], \tag{A.6}$$

which has a unique zero, i.e, there exists a time instant $\tau_* \in [0, T^+]$, and a corresponding value $x_* = x(\tau_*) \in [X_{\min}, X_{\max}]$, such that the function θ is zero. Because θ is known, then x_* is also known. Define the quantity

$$a = \left(\frac{d\theta(x)}{dx} \right)_{x=x_*}. \tag{A.7}$$

Then, the parameter n is determined as:

$$n = \frac{\log\left[\frac{\left(\frac{d\theta(x)}{dx}\right)_{x=x_{*2}} - a}{\left(\frac{d\theta(x)}{dx}\right)_{x=x_{*1}} - a}\right]}{\log\left(\frac{\theta_{x=x_{*2}}}{\theta_{x=x_{*1}}}\right)} \tag{A.8}$$

where $x_{*2} > x_{*1} > x_*$ are design parameters. Define

$$b = \frac{a - \left(\frac{d\theta(x)}{dx}\right)_{x=x_{*2}}}{\theta(x_{*2})^n}. \tag{A.9}$$

Then, the parameters κ_w and ρ are computed as follows:

$$\kappa_w = \sqrt[n]{\frac{a}{b}}, \tag{A.10}$$

$$\rho = \frac{a}{\kappa_w}. \tag{A.11}$$

The function $\bar{w}(x)$ can be computed as:

$$\bar{w}(x) = \frac{\theta(x)}{\kappa_w}. \tag{A.12}$$

Finally, the remaining parameter σ is determined as:

$$\sigma = \frac{1}{2}\left(\frac{\frac{\left(\frac{d\bar{w}(x)}{dx}\right)_{x=x_{*3}}}{\rho} - 1}{(-\bar{w}(x_{*3})^n)} + 1\right) \tag{A.13}$$

where x_{*3} is a design parameter such that $x_{*3} < x_*$.

Appendix B

Smart base-isolated benchmark building

Introduction

The smart base-isolated benchmark building [81] is employed as an interesting and realistic example to investigate the effectiveness of passive, active or semi-active control systems. This benchmark problem is recognized by the American Society of Civil Engineers (ASCE) Structural Control Committee as a state-of-the-art model developed to provide a computational platform for numerical experiments of seismic control attenuation [86, 102].

Structural model

The benchmark structure is a base-isolated eight-storey, steel-braced framed building, 82.4 m long and 54.3 m wide, similar to existing buildings in Los Angeles, California. The floor plan is L-shaped, as shown in Figure B.1. The superstructure bracing is located at the building perimeter. Metal decking and a rigid of steel beams support all concrete floor slabs. The steel superstructure is supported on a reinforced concrete base slab, which is integral with concrete beams below, and drop panels below each column location. The isolators are connected between these

drop panels and the footing below, as shown in Figure B.1. The superstructure is located as a three-dimensional linear elastic system. The superstructure members, such as beam, column, bracing, and floor slab are modeled in detail. Floor slabs and the base are assumed to be rigid in plane.

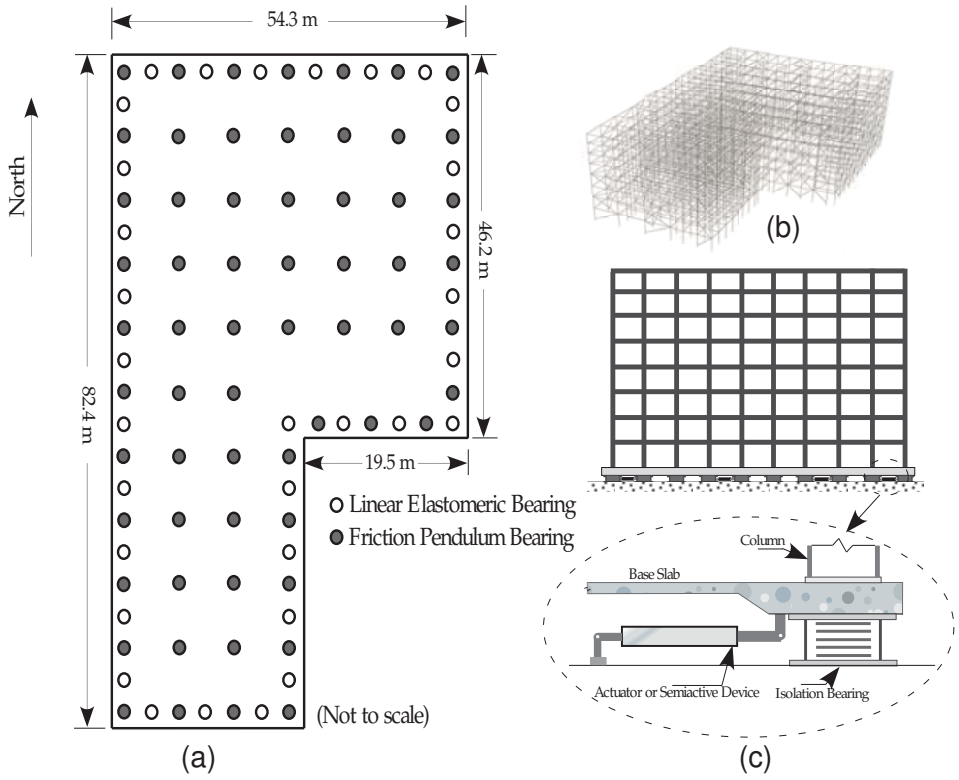

Figure B.1: (a) Isolation plan; (b) FEM model of superstructure, and (c) Elevation view with devices [81].

The superstructure and the base are modeled using three master degrees of freedom (DOF) per floor at the center of mass. The combined model of the superstructure (24 DOF) and isolation system (3 DOF) consists of 27 degrees of freedom. All

twenty four modes in the fixed-base case are used in modeling the superstructure. The superstructure damping ratio is assumed to be 5% in all fixed-base modes. See Figure 5.1 for a representative figure of the benchmark structure.

The computed natural periods for all 24 fixed-base modes are shown in Table B.1. The nominal isolation system consists of 61 friction pendulum bearings and 31 linear elastomeric bearings, as shown in Figure B.1. The nominal isolation system can also be regarded as a linear isolation system consisting of 92 linear elastomeric bearing and 61 passive friction dampers; since the friction pendulum bearings consist of an linear elastic part due to the curvature of the sliding surface and friction. While the nominal model consists sliding and linear elastomeric bearings, participants may replace them with other types of bearings. The total weight of the structure is 202 000 kN.

Isolation model

Several isolation elements are included so that any combination of these can be used to model the isolation system completely. The isolation elements are elastic, viscous, hysteretic elements for bilinear elastomeric bearings and hysteretic elements for sliding bearings. The force-displacement characteristics for friction pendulum, lead rubber bearing and linear isolation bearing are shown in Figure B.2. The hysteretic elements can be uniaxial or biaxial. The linear elastic and viscous elements are for modeling linear elastomeric bearings and fluid dampers. They can also be used for modeling bilinear elastomeric isolation systems with corresponding equivalent linear properties, obtained using appropriate linearization techniques.

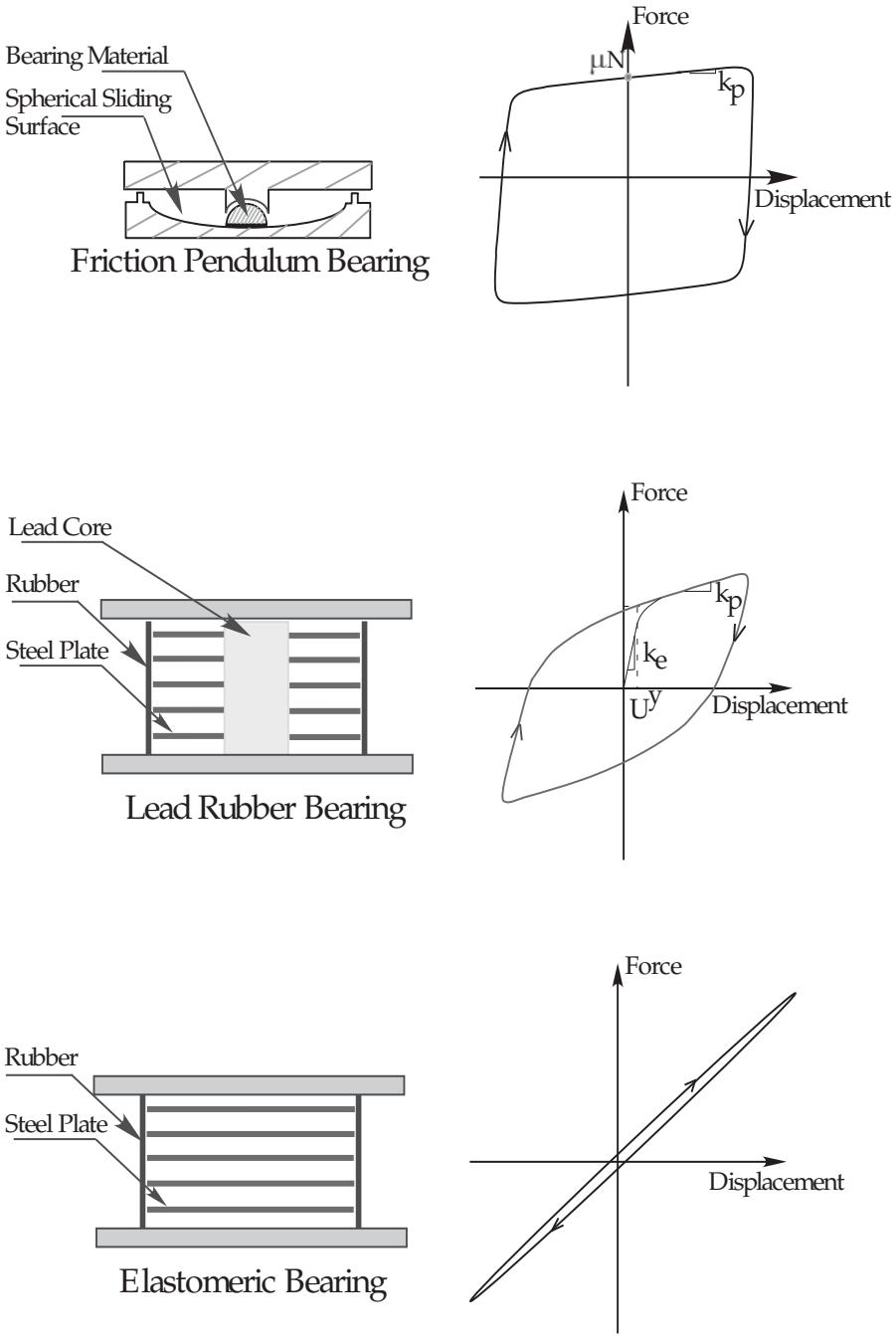

Figure B.2: Force-displacement characteristics of bearings [81].

Evaluation criteria

The following nine evaluation criteria are defined for the benchmark problem based on both maximum and RMS responses of the building. For each control design, these criteria must be evaluated for all seven earthquakes, in two orthogonal directions. In the following discussion, the term *uncontrolled* refers to the isolation system containing linear and nonlinear bearing, but with no supplemental passive dampers or control devices.

1. Peak base shear (isolation level) in the controlled structure normalized by the corresponding shear in the uncontrolled structure
$$J_1(q) = \frac{\max_t ||V_0(t,q)||}{\max_t ||\hat{V}_0(t,q)||}$$

2. Peak structural shear (at first storey level) in the controlled structure normalized by the corresponding shear in the uncontrolled structure
$$J_2(q) = \frac{\max_t ||V_1(t,q)||}{\max_t ||\hat{V}_1(t,q)||}$$

Table B.1: Periods of the superstructure [81]

	North-South	East-West	Torsion
1	0.78	0.89	0.66
2	0.27	0.28	0.21
3	0.15	0.15	0.12
4	0.11	0.11	0.08
5	0.08	0.08	0.07
6	0.07	0.07	0.06
7	0.06	0.06	0.06
8	0.05	0.06	0.05

3. Peak base displacement or isolator deformation in the controlled structure normalized by the corresponding displacement in the uncontrolled structure

$$J_3(q) = \frac{\max_{t,i}||d_i(t,q)||}{\max_{t,i}||\hat{d}_i(t,q)||}$$

4. Peak inter-storey drift in the controlled structure normalized by the corresponding inter-storey drift in the uncontrolled structure

$$J_4(q) = \frac{\max_{t,f}||d_f(t,q)||}{\max_{t,f}||\hat{d}_f(t,q)||}$$

5. Peak absolute floor acceleration in the controlled structure normalized by the corresponding acceleration in the uncontrolled structure

$$J_5(q) = \frac{\max_{t,f}||a_f(t,q)||}{\max_{t,f}||\hat{a}_f(t,q)||}$$

6. Peak force generated by all control devices normalized by the peak base shear in the controlled structure

$$J_6(q) = \frac{\max_t||\sum_k F_k(t,q)||}{\max_t||V_0(t,q)||}$$

7. RMS base displacement in the controlled structure normalized by the corresponding RMS base displacement in the uncontrolled structure

$$J_7(q) = \frac{\max_i||\sigma_d(t,q)||}{\max_i||\sigma_{\hat{d}}(t,q)||}$$

8. RMS absolute floor acceleration in the controlled structure normalized by the corresponding RMS acceleration in the

uncontrolled structure

$$J_8(q) = \frac{\max_f ||\sigma_a(t,q)||}{\max_f ||\sigma_{\hat{a}}(t,q)||}$$

9. Totall energy absorbed by all control devices normalized by energy input into the controlled structure

$$J_9(q) = \frac{\sum_k \left[\int_0^{T_q} F_k(t,q) v_k(t,q) dt\right]}{\int_0^{T_q} \langle V_0(t,q) \dot{U}_g(t,q)\rangle dt}$$

where, i = isolator number, $1, \ldots, N_i (N_i = 8)$; k = device number, $1, \ldots, N_d$; f = floor number, $1, \ldots, N_f$; q = earthquake number, $1, \ldots, 7$; t = time, $0 \leq t \leq T_q$; $\langle \cdot \rangle$ =inner product; $|| \cdot ||$ = vector magnitude incorporating NS and EW components.

Bibliography

[1] A.A. Adewuya, *New method in genetic search with real-valued chromosomes*, Master's thesis, Massachusetts Institute of Technology, Cambridge (1996).

[2] M. Ahmadian, *Design and development of magneto-rheological dampers for bicycle suspensions*, ASME Dynamical Systems & Control Division **DSC-67** (1999), 737–741.

[3] M. Ahmadian, J.C. Poynor, and J.M. Gooch, *Application of magneto-rheological dampers for controlling shock loading*, ASME Dynamical Systems & Control Division **DSC-67** (1999), 731–735.

[4] T.T. Baber and M.N. Noori, *Random vibration of pinching hysteretic systems*, J. Eng. Mech **110** (1984), 1036–1049.

[5] T.T. Baber and Y.N. Noori, *Random vibration of degrading pinching system*, Journal of Engineering Mechanics **111** (1985), 1010–1026.

[6] T.T. Baber and Y.K. Wen, *Random vibration hysteretic, degrading systems*, Journal of Engineering Mechanics, ASCE **124** (1981), 319–327.

[7] K. Bani-Hani and J. Ghaboussi, *Nonlinear structural control using neural networks*, Journal of Engineering Mechanics, ASCE **124** (1998), 1069–1087.

[8] D.M. Bates and D.G. Watts, *Nonlinear regression analysis and its applications*, Wiley: New York, 1998.

[9] Z. Bazant, *Endochronic inelasticity and incremental plasticity*, Int. J. Solids Struct. **14** (1978), 691–714.

[10] G. Bossis, P. Khuzir, S. Lacis, and O. Volkova, *Yield behavior of magnetorheological suspensions*, Journal of Magnetism and Magnetic Materials **258-259** (2003), 456–458.

[11] R. Bouc, *Forced vibration of mechanical system with hysteresis (abstract)*, Proc., 4th Conf. on Nonlinear Oscillation, Prague, Czechoslovakia (1967).

[12] ———, *Modèle mathèmatique d'hystérésis (a mathematica model for hysteresis)*, Acustica **21** (1971), 16–25.

[13] T. Butz and O. von Stryk, *Modelling and simulation of electro- and magnetorheological fluid dampers*, ZAMM. Z. Angew. Math. Mech. **82** (2002), 3–20.

[14] F. Casciati, *Nonlinear stochastic dynamics of large structural systems by equivalent linearization*, Proc., 5th Int. Conf. on Application of Statistics and Probability in Soil and Structural Engineering,ICASP5, Vancouver, B.C., Canada (1987).

[15] C.C. Chang and P.N. Roschke, *Neural network modeling of a magnetorheological damper*, Journal of Intelligent Material Systems and Structures **9** (1998), 775–764.

[16] C.C. Chang and T. Tse, *Commanding mr dampers through a bouc-wen based inverse dynamic model*, Proc. Third World Conference on Structural Control, Como, april 7-11, Italy (2002), 787.

[17] C.C. Chang and L. Zhou, *Neural network emulation of inverse dynamics for a magnetorheological damper*, Journal of Structural Engineering, ASCE **128** (2002), 231–239.

[18] A.G. Chassiakos, S.F. Masri, A.W. Smyth, and T.K. Caughy, *On-line identification of hysteretic systems*, Journal of Applied Mecanics **65** (1998), 194–203.

[19] H.M. Chen, K.H. Tsai, G.Z. Qi, and J.C.S. Yang nad F. Amini, *Neural network for structure control*, J. Computing in Civ. Engrg. ASCE **9** (1995), 168–176.

[20] K.M. Choi, H.J. Lee, S. W. Cho, and I.W. Lee, *Modified energy dissipation algorithm for seismic structures using magnetorheological dampers*, KSCE Journal of Civil Engineering **11** (2007), 121–126.

[21] W.W. Chooi and S.O. Oyadiji, *Design, modeling and testing of magnetorheological dampers using analytical flow solution*, Computers and Structures **86** (2008), 473–482.

[22] D.G. Reigles DG and M.D. Symans, *Supervisory fuzzy control of a base-isolated benchmark building utilizing a neuro-fuzzy model of controllable fluid viscous dampers*, Structural Control and Health Monitoring **13** (2006), 724–747.

[23] A. Dominguez, R. Sadaghati, and I. Stiharu, *Modelling the hysteresis phenomenon of magnetorheological dampers*, Smart Mater. Struc. **13** (2004), 1351–1361.

[24] ———, *A new dynamic hysteresis model for magnetorheological dampers*, Smart Mater. Struc. **15** (2006), 1179–1189.

[25] H. Du and N. Zhang, *Evolutionary takagi-sugeno fuzzy modelling for mr damper*, Proceeding of the Sixth International Conference on Hybrid Intelligent Systems (HIS'06), December 13-15, Auckland, New Zealand (2006).

[26] S.J. Dyke and B.F. Spencer Jr., *Seismic response control using multiple mr dampers*, Proceedings of the 2nd International Workshop on Structural Control, Hong Kong (1996), 163–173.

[27] S.J. Dyke, B.F. Spencer Jr., M.K. Sain, and J.D. Carlson, *Modeling and control of magnetorheological dampers for seismic response reduction*, Smart Material and Structures **5** (1996a), 565–575.

[28] _____, *Seismic response reduction using magnetorheological dampers*, Proceedings of the IFAC world congress, June 30-July 5, San Francisco, CA. (1996b).

[29] _____, *An experimental study of mr dampers for seismic protection*, Smart Materials and Structures: Special Issue on Smart Materials and Structures Technology: Application to Large Civil Infrastructures **7** (1998), 693–703.

[30] R.C. Ehrgott and S.F. Masri, *Modelling the oscillatory dynamic behaviour of electrorheologicall materials in shear*, Smart Material and Structures **1** (1992), 275–285.

[31] _____, *Structural control applications of an electrorheological device*, Proceedings of the International Workshop on Structural Control, USC Publication, Number CE-9311 (1994), 115–129.

[32] G.C. Foliente, M.P. Singh, and M.N. Noori, *Equivalent linearization of generally pinching hysteretic, degrading systems*, Earthquake Eng. Struct. Dyn. **25** (1996), 611–629.

[33] D.R. Gamota and F.E. Filisko, *Dynamic mechanical studies of electrorheological materials: moderate frequencies*, J Rheol **35** (1991), 339–425.

[34] J. Gang, M.K. Sain, K.D. Pham, B.F. Spencer Jr., and J.C. Romallo, *Modeling mr-dampers: A nonlinear blackbox approach*, Proc. American Control Conference (2001), 429–434.

[35] H. Gavin and U. Aldemir, *Optimal control of earthquake responce using semiactive isolation*, Journal of Eng. Mech., ASCE **131** (2005), 769–776.

[36] J. Ghaboussi and A. Joghataie, *Active control of structures using neural networks*, J. Engrg. Mech., ASCE **121** (1995), 555–567.

[37] Z.Q. Gu and S.O. Oyadiji, *Application of mr damper in structural control using anfis method*, Computer and Structures **86** (2008), 427–436.

[38] T.P. Gunstona, J. Rebelleb, and M.J. Griffina, *A comparison of two method of simulating seat suspension dynamic performance*, Journal of Sound and Vibration **278** (2004), 117–134.

[39] J. Ha, Y. Kung, R. Fungc, and S. Hsien, *A comparison of fitness functions for the identification of a piezoelectric hysteretic actuator based on the real-coded genetic algorithm*, Sensors and Actuators **132** (2006), 643–650.

[40] Q.P. Ha, N.M. Kwok, M.T. Nguyen, B. Samali, and J. Li, *Mitigation of seismic responses on building structures using mr dampers with lyapunov-based control*, Struc. Control Health Monit. **15** (2008), 604–621.

[41] R.L. Haupt and S.E. Haupt, *Practical genetic algorithms*, Wiley Interscience Publication, 1998.

[42] Lord Corporation homepage, *http://www.lord.com/home/magnetorheologicalmrfluid/mrfluidtechnology/whatismr-/tabid/3772/default.aspx*.

[43] ———, *http://www.lord.com/home/magnetorheologicalmrfluid/products/magnetorheologicalmrfluids/tabid/3360-/default.aspx*.

[44] J. Huang, J.Q. Zhang, Y. Yang, and Y.Q. Wei, *Analysis and design of a cylindrical magneto-rheological fluid brake*, Journal of Materials Processing Technology **129** (2002), 559–562.

[45] F. Ikhouane and O. Gomis-Bellmunt, *A limit cycle approach for the parametric identification of hysteresis system*, System & Control Letters **57** (2008), 663–669.

[46] F. Ikhouane, J.E. Hurtado, and J. Rodellar, *Variation of the hysteresis loop with the bouc-wen model parameters*, Nonlinear Dynamics **48** (2007), 361–380.

[47] F. Ikhouane and J. Rodellar, *On the hysteretic bouc-wen model part i: Forced limit cycle characterization*, Nonlinear Dynamics **42** (2005), 63–78.

[48] ———, *Systems with hysteresis: Analysis, identification and control using the bouc-wen model*, John Wiley & Sons, Inc, 2007.

[49] J. Inaudi, F. López-Almansa, J.M. Kelly, and J. Rodellar, *Predictive control of base-isolated structures*, Earthquake Engineering & Structural Dynamics **21** (1992), 471–482.

[50] L.M. Jansen and S.J. Dyke, *Semi-active control strategies for mr dampers: A comparative study*, ASCE Journal of Engineering Mechanics **126** (2000), 795–803.

[51] E.A. Johnson, J.C. Ramallo, B.F. Spencer, and M.K. Sain, *Intelligent base isolation systems*, Proceedings of the Second World Conference on Structural Control, Kyoto, Japan, June, 1 (1998), 367–376.

[52] M.R. Jolly, J.W. Bender, and J.D. Carlson, *Properties and applications of commercial magnetorheological fluids*, Journal of Intelligent Material Systems and Structures **10** (1999), 5–13.

[53] H.J. Jung, K.M. Choi, B.F. Spencer Jr., and I.W. Lee, *Application of some semi-active control algorithms to a smart base-isolated building employing mr dampers*, Structural Control and Health Monitoring **13** (2006), 693–704.

[54] H.J. Jung, B.F. Spencer Jr., Y.Q. Ni, and I.W. Lee, *State-of-the-art of semiactive control systems using mr fluid dampers in civil engineering applications*, Structural Engineering and Mechanics **17** (2004), 493–526.

[55] H.R. Karimi, M. Zapateiro, and N. Luo, *Wavelet-based parameter identification of a nonlinear magnetorheological damper*, International Journal of Wavelets, Multiresolution and Information Processing **7** (2009), no. 2, 183–198.

[56] M. Kciuk and R. Turczyn, *Properties and application of magnetorheological fluids*, Journal of Achievement in Material and Manufacturing Engineering **18** (2006), no. 1-2, 127–130.

[57] J.M. Kelly, *The role of damping in seismic isolation*, Earthquake Engineering & Structural Dynamics **28** (1999), no. 1, 3–20.

[58] W. Klein, A. Mezyk, and M. Otorowski, *The application overhaul of magnetorheological fluids in mechanical engineering*, XIII International Scientific Conference TEMAG, Gliwice-Ustro (2005), 95–105.

[59] J.H. Koo, *Using magneto-rheological dampers in semiactive tuned vibration absorbers to control structural vibrations*, Dissertation submitted to the faculty of the Virginia Polytechnic Institute and State University.

[60] N.M. Kwok, Q.P. Ha, M.T. Nguyen, J. Li, and B. Samali, *Bouc-wen model parameter identification for a mr fluid damper using computationally efficient ga*, ISA Transactions, doi: 10.1016/j.isatra.2002.08.005 **46** (2007), 167–179.

[61] A. Kyprianou, K. Worden, and M. Panet, *Identification of hysteresis system using the differential evolution algorithm*, Journal of Sound and Vibration **2** (2001), no. 248, 289–314.

[62] H.J. Lee, H. J. Jung, W.H. Yun, and I.W. Lee, *Semi-active neuro-control using mr damper for base-isolated benchmark problem*, The Eighteenth KKCNN Symposium on Civil Engineering, December 18-20, Taiwan (2005).

[63] S. J. Li, H. Yu, and Y. Suzuki, *Identification of non-linear hysteretic system with slip*, Computers and Structures **82** (2004), 157–165.

[64] S.J. Li, Y. Suzuki, and M. Noori, *Identification of hysteretic system with slip using bootstrap filter*, Mechanical System and Signal Processing **18** (2004), 781–795.

[65] W.H. Li, G.Z. Yao, S.H. Yeo, and F.F. Yap, *Testing and steady state modeling of a linear mr damper under sinusoidal loading*, Smart Mater. Struct. (2009), 95–102.

[66] Z. Li and C.C. Chang, *Adaptive fuzzy control for a structure-mr damper system*, SPIE procceding series, Smart systems for bridges, structures, and highways, Newport Beach, CA, 6-7 March (2000), 105–115.

[67] J. Lin, *Extraction of dynamic soil properties using extended kalman filter*, Journal of Geotechnical Engineering **120** (1994), no. 12, 2100–2117.

[68] J. lin and R. Betti, *On-line identification and damage detection in non-linear structural system using a variable forgetting factor approach*, Earthquake Engineering and Structural Dynamics **33** (2004), 419–444.

[69] J. Lin, R. Betti, A.W. Smyth, and R.W. Longman, *On-line identification of non-linear hysteretic structural systems using a variable trace approach*, Eartquake Engineerinf and Structural Dynamics (2001), 1279–1303.

[70] J.S. Lin and Y. Zhang, *Nonlinear structural identification using extended*, Computers and Structures **52** (1994), no. 4, 757–764.

[71] H.R. Lo, J.K. Hammond, and M.G. Sainsbury, *Non-linear system identification and modelling with application to an isolator with hystereis*, Processing of the 6th International Modal Analysis Conference, FL, **22** (1993), 129–150.

[72] C. Loh, L.Y. Wu, and P.Y. Lin, *Displacement control of isolated structures with semi-active control device*, Journal of Structural Control **10** (2003), 77–100.

[73] C.H. Loh and S.T. Chung, *A three-stage identification approach for hysteretic systems*, Earthquake Engineering and Structural Dynamics **II** (1998), 1453–1459.

[74] K.C. Lu, C.H. Loh, J.N. Yang, and P.Y. Lin, *Decentralized sliding mode control of a building using mr dampers*, Smart Mater. Struct. **17** (2008), 225–240.

[75] N. Luo, J. Rodellar, J. Vehí, and M. De la Sen, *Composite semiactive control of a class of seismically excited structures*, Journal of the Franklin Institute **338** (2001), 225–240.

[76] F. Ma, C.H. Ng, and N. Ajavakom, *On system identification and response prediction of degrading structures*, Structural Control and Health Monitoring **13** (2006), 347–364.

[77] O. Maruyama, C.B. Yun, M. Hoshiya, and M. Shinozuka, *Program exka12 for identification of structural dynamic system*, Technical report, NCEER-89-0014, National Center for Earthquake Engineering Research: Buffalo, NY (1989).

[78] S.F. Masri, J.P. Caffrey, T.K. Caughey, A.W. Smyth, and A.G. Chassiakos, *Identification of the state equation in complex non-linear system*, International Journal of Non-Linear Mechanics **39** (2004), 1111–1127.

[79] F. Naeim and J.M. Kelly, *Design of seismic isolated structures: From theory to practice*, Wiley, Chichester, England, 1999.

[80] S. Narasimhan, and S. Nagarajaiah,*Smart base-isolated benchmark building part II: Phase I sample controllers for linear isolation systems*, Journal Structural Control and Health Monitoring **13** (2006), 589–604.

[81] S. Narasimhan, S. Nagarajaiah, E. A. Johnson, and H.P. Gavin, *Smart base-isolated benchmark building. part I: Problem definition*, Journal Structural Control and Health Monitoring **13** (2006), 573–588.

[82] S. Narasimhan, S. Nagarajaiah, and E.A. Johnson, *Smart base-isolated benchmark building. part iv: phase ii sample controller for nonlinear isolation systems*, Journal Structural Control and Health Monitoring **15** (2008), 657–672.

[83] M.T. Nguyen, N.M. Kwok, Q.P. Ha, J. Li, and B. Samali, *Semi-active direct control of civil structure seismic responses using magneto-rheological dampers*, 24th International Symposioum on Automation and Robotics in Construction, ISARC (2007).

[84] Y.Q. Ni, J.M. Ko, and C.W. Wong, *Identification of nonlinear hysteretic isolators from periodic vibration tests*, Journal of Sound and Vibration **4** (1998), 737–756.

[85] M.N. Noori, J. Choi, and H. Davoodi, *Zero and nonzero mean random vibration analysis of a new general hysteresis model*, Probab. Eng. Mech. **1** (1986), 192–201.

[86] Y. Ohtori, R.E. Christenson, B.F. Spencer, and S.J. Dyke, *Benchmark problems in seismically excited nonlinear buildings*, Journal of Engineering Mechanics, ASCE **130** (2004), 366–385.

[87] Y.J. Park, Y.K. Wen, and A.H.S. Ang, *Random vibration of hysteretic systems under bi-directional ground motion*, Earthquake Eng. Struct. Dyn. **14** (1986), 543–547.

[88] J. Poynor, *Innovative designs for magneto-rheological dampers*, MS thesis, Virginia Polytechnic Institute and State University, Blacksburg, VA; 2001.

[89] F. Pozo, L. Acho, A. Rodríguez, and G. Pujol, *Nonlinear modeling of hysteretic systems with double hysteretic loops using position and acceleration information*, Nonlinear Dynamics.

[90] F. Pozo, P.M. Montserrat, J. Rodellar, and L. Acho, *Robust active control of hysteretic base-isolated structures: Application to the benchmark smart base-isolated building*, Structural Control and Health Monitoring **15** (2008), 720–736.

[91] J.C. Ramallo, E.A. Johnson, and B.F. Spencer Jr., *"smart" base isolation systems*, Journal of Engineering Mechanics **128** (2002), 1088–1099.

[92] J.C. Ramallo, H. Yoshioka, and B.F. Spencer, *A two-step identification technique for semiactive control system*, Structural Control and Health Monitoring **11** (2004), 273–289.

[93] A. Rodríguez, F. Ikhouane, J. Rodellar, and N. Luo, *Modeling and identification of a small-scale magnetorheological damper*, Journal of Intelligent Materials, Systems and Structures (2009).

[94] A. Rodríguez, N. Iwata, F. Ikhouane, and J. Rodellar, *Model identification of a large-scale magnetorheological fluid damper*, Smart Materials and Structures **18** (2009).

[95] S.M. Savaresi, S. Bittanti, and M. Montiglio, *Identification of semi-physical and block-box nonlinear models: The case of mr dampers for vehicles control*, Automatica **41** (2005), 113–127.

[96] K.C. Schurter and P.N. Roschke, *Neuro-fuzzy control of structures using magnetorheological dampers*, Proceeding

of the American Control Conference, Artington, VA June 25-27 (2001).

[97] L.F. Shampine, *Numerical solution for ordinary differential equations*, Chapman & Hall: London, 1994.

[98] R.I. Skinner, W.H. Robinson, and G.H. McVerry, *An introduction to base isolation*, John Wiley & Sons, Inc, 1992.

[99] J. Song and A.D. Kiureghian, *Generalized bouc-wen model for highly asymmetric hysteresis*, Journal of Engineering Mechanics-ASCE **132** (2006), 610–618.

[100] T.T. Soong and M.C. Constantinou, *Passive and active structural vibration control in civil engineering*, Springer-Verlag, 1994.

[101] B.F. Spencer, S.J. Dyke, M.K. Sain, and J.D. Carlson, *Phenomenological model of a magnetorheological damper*, J. Engrg. Mech., ASCE **123** (1997a), 230–238.

[102] B.F. Spencer and S. Nagarajaiah, *State of the art of structural control*, Journal of Structural Engineering **129** (2003), 845–856.

[103] A.G. Sreenatha and M. Pradham, *Fuzzy logic controller for position control of flexible structures*, Acta Astrunautica **50** (2002), 665–671.

[104] R. Stanway, J.L. Sprosten, and N.G. Stevens, *Non-linear identification of an electrorheological vibration damper*, IFAC Identification and System Parameter Estimation (1985), 195–200.

[105] ———, *Non-linear modeling of an electrorheological vibration damper*, J. Electrostatics **20** (1987), 167–184.

[106] W. Sun, H. HU, and J. Weng, *Design, testing and modelling of magnetorheological damper with stepped restoring torque*, Journal of Intelligent Material Systems and Structures **17** (2006), 335–340.

[107] R.S. Thyagarajan and W.D. Iwan, *Performance characteristics of a widely used hysteretic model in structural dynamics*, Proc., 4th U.S. National Conf. Earthquake Engineering, Palm Springs, Calif.

[108] H.H. Tsang, R.K.L. Su, and A.M. Chandler, *Simplified inverse dynamics models for mr fluid dampers*, Engineering Structures **28** (2006), 327–341.

[109] D.H. Wang and W.H. Liao, *Modeling and control of magnetorheological fluid damper using neutral networks*, Smart Materials and Structures **14** (2005), 111–126.

[110] D.H. Wang and Y.K. Wen, *Reliability and redundancy of pre-northridge low-rise steel building under seismic excitation*, Rep. No. UILU-ENG-99-2002, Univ. Illinois at Urbana-Champaign, Champaign, Ill (1998).

[111] Y.K. Wen, *Method of random vibration of hysteretic systems*, ASCE Journal Eng. Mechanics **102** (1976), 249–263.

[112] ———, *Equivalent linearization for hysteretic systems under random excitation*, Trans. ASME **47** (1980), 150–154.

[113] Y. Woosoon, S.N. Singh, and M.A. Minnicino, *Semi-active control of magnetorheological damper system: A lyapunov design*, APIE proceeding series, Modeling, signal processing, and control conference, San Diego CA **5383** (2004), 289–297.

[114] P. Q. Xia, *An inverse model of mr damper using optimal neural network and system identification*, Journal of Sound and Vibration **266** (2005), 1009–1023.

[115] Y.L. Xu, W.L. Qu, and J.M. Ko, *Seismic response control of frame structures using magnetorheological/electorheological dampers*, Earthquake Engineering and Structural Dynamics **29** (2000), 557–575.

[116] Z. Xu, A.K. Agrawal, and J.N. Yang, *Semi-active and passive control of the phase i linear base-isolated benchmark building model*, Structural Control and Health Monitoring **13** (2006), 626–648.

[117] Z. Xu and Q. Guob, *Fuzzy control method for earthquake mitigation with magnetorheological dampers*, Journal of Intelligent Material Systems and Structures **17** (2006), 871–881.

[118] G. Yang, *Large-scale magnetorheological fluid damper for vibration mitigation: Modeling, testing and control*, Ph.D dissertation,University of Notre Dame (2001).

[119] M. Yar and J.K. Hammond, *Parameter estimation for hysteretic system*, Journal of Sound and Vibration **117** (1987), 161–172.

[120] F. Yi, S. J. Dyke, J. M. Caicedo, and J. D. Carlson, *Experimental verification of multi-input seismic control strategies for smart dampers*, ASCE Journal of Engineering Mechanics **127** (2001), no. 11, 1152–1164.

[121] F. Yi, S.J. Dyke, J.M. Caicedo, and J. D. Carlson, *Seismic response control using smart dampers*, Proceedings of the 1999 American Control Conference, San Diego, California, June 23-25 (1999a), 1022–26.

[122] F. Yi, S.J. Dyke, J.M. Caicedo, and J.D. Carlson, *Experimental verification of multi-input seismic control strategies for smart dampers*, Journal of Engineering Mechanics **127** (2001), 1152–1164.

[123] O. Yoshida and S. J. Dyke, *Seismic control of a nonlinear benchmark building using smart dampers*, Journal of Engineering Mechanics **130** (2004), 386–392.

[124] H. Yoshioka, J.C. Ramallo, and B.F. Spencer, *"smart" base isolation strategies employing magnetorhelogical*

dampers, Journal of Engineering Mechanics, ASCE **128** (2002), 540–551.

[125] M. Zapateiro, and N. Luo, *Neural network modeling of magnetorhelogical dampers*, Artificial Intelligence Research and Development **163** (2007), 351–358.

[126] M. Zapateiro, R. Villamizar, and N. Luo, *Semiactive seismic vibration control of structures equipped with magnetorheological dampers*, International Journal of Factory Automation, Robotics and Soft Computing, no.1 (2008), 77–84.

[127] M. Zapateiro, H.R. Karimi, N. Luo, and B.F. Spencer, Jr., *Real-time hybrid testing of semiactive control strategies for vibration reduction in a structure with MR damper*, Structural Control and Health Monitoring, doi:10.1002/stc.321 (2008).

[128] H. Zhang, G.C. Foliente, Y. Yang, and F. Ma, *Parameter identification of inelastic structures under dynamic loads*, Earthquake Engineering and Structural Dynamics **31** (2002), 1113–1130.

[129] J. Zhang, T. Sato, and S. Lai, *Non-linear system identification of the versatile-type structures by a novel signal processing technique*, Earthquake Engineering & Structural Dynamics **36** (2007), 909–925.